

THE UNIVERSITY *of* EDINBURGH
School of Engineering

Engineering Design of Actuated Sensor Alignment Systems for Subsea Applications

Alistair I. **Murison**

(Supervisor: Dr Brian G. Sellar)

The University of Edinburgh
9 April 2026

Personal Statement

This project was undertaken in response to a design brief set by my supervisor, Dr Brian Sellar, to design an actuator housing for integration into an existing subsea gravity mooring, allowing measuring equipment to be positioned while resisting tidal forces. The flow modelling sections were my expansion of the scope following discussion with Dr Sellar.

Before this project, I had no exposure to marine projects. As part of weekly meetings with Dr Sellar and independent research, I developed the knowledge required to produce the presented design. My initial plan was to complete the design work by the end of semester 1 and progress to manufacture and testing in semester 2. This proved unrealistic due to the complexity of the design state and my wider academic workload and commitments, so the project scope was revised early on.

The project was linked to the MEng project conducted by Michael Wilson. During the early stages, we collaborated to conduct an interview with Dr Sellar to determine the operational requirements of our respective projects. This includes producing all of the documentation surrounding GDPR.

I completed the theoretical design using STAR-CCM+ for flow modelling and SOLIDWORKS for CAD and structural analysis. I would have preferred to use ABAQUS for structural analysis, but after the flow modelling section took longer than anticipated, there was insufficient time to learn the software, which would have added further value to my results.

Although I was provided with CAD files of the existing gravity mooring for Computational Fluid Dynamics (CFD) simulations, the derivation of the flow equations, CFD simulations themselves, and analysis of the results were my own. Dr Sellar also shared a previous housing mock-up based on standard purchased components, but the design presented here was developed independently to meet the project objectives.

AI tools such as Grammarly Pro and ELM were utilised to assist with suggestions for editing, condensing, and presenting my work. They were not used to generate any original content, including the underlying engineering analysis, CFD results, design work, or discussion and conclusions. All submitted content was reviewed and edited by me.

I declare that this thesis is my original work except where stated.



Alistair I. **Murison**, 9 April 2026
[Word count: 9972]

Summary

Project Title: Engineering Design of Actuated Sensor Alignment Systems for Subsea Applications
Author: Alistair I. **Murison**
Date: 9 April 2026

In the effort to improve renewable energy capabilities, obtaining accurate tidal flow data is critical for assessing locations for tidal turbine deployment in tidal channels, such as the Fall of Warness in Orkney. To position velocity-measuring equipment against tidal forces, Acoustic Doppler Current Profilers (ADCP), the aim of this project was to quantify the tidal forces acting on the equipment, and to select an appropriate actuator and design a housing that is low-cost, high-performance, and manufacturable. It is to fit into an existing passively aligning two-axis gimbal set.

The work consisted of research, analytical modelling, computational fluid dynamics (CFD) simulations of the flow, and component design. A simplified analytical flow model was developed for the Fall of Warness, combining depth-dependent current velocity, Stokes second-order wave motion and turbulent intensity. This model provided inlet conditions for transient STAR-CCM+ simulations of flow around the existing gravity mooring frame, gimbal system and ADCP.

CFD studies reproduced the expected bluff-body flow features around the frame, including stagnation, separation, wake formation and internal recirculation. A key result was that the highest loads on the system occurred under long-term mean flow rather than extreme conditions, indicating that internal mixing and vortex interaction were more important than current velocity alone. The CFD model predicted a maximum moment of 1.185 Nm about the outer gimbal axis, which was taken as the actuator design load. The result was mesh independent. Commercial actuators were then reviewed against holding torque, size and cost. The selected actuator was the MyActuator RH-17, whose brake provides an effective holding torque of 50 Nm at the output shaft, corresponding to a safety factor of approximately 42.

A detailed air-filled housing concept was developed for a 100 m depth rating. Stainless steel 316 was selected for an output shaft and end-cap covering, and POM-C acetal for a rear housing element. Components were designed to a safety factor of 2, verified by finite element analysis (FEA), with acceptable deflections in all cases. The estimated cost for a pair of actuator assemblies for a two-axis gimbal was £3,341.74, with the actuators accounting for 70% of the total.

The project met its primary objectives by defining operational requirements, characterising the site flow, selecting a suitable actuator, and developing a structurally justified housing design supported by CFD and FEA. The main limitations were the simplified flow model, the absence of direct validation data, and the unresolved reverse-flow CFD case. Nevertheless, the work provides a credible basis for prototype manufacture, further analysis and future subsea testing.

Acknowledgements

I would like to thank my project supervisor, Dr Brian Sellar, whose guidance and enthusiasm throughout the report have been invaluable. In particular, his assistance in improving my understanding of the marine environment and sector enabled me to make informed decisions throughout this report.

I would also like to thank Michael Wilson for his collaboration in the early stages of the report, when we initially began defining the operational requirements of our interlinked MEng projects.

Furthermore, I would like to thank a number of academics whose teaching resources have been highly beneficial to the content and writing up of this project. In particular, Professor David Ingram for organising the Computational Fluid Dynamics 5 course, which was essential and highly valuable in enabling me to complete the modelling in this report. Also, to Dr Felipe Teixera-Dias for his Overleaf LaTeX workshops, which helped improve my skill set using Overleaf.

Finally, I would like to thank those who have had a positive overall impact on my university experience. Those would include, but are not limited to, my friends in the Edinburgh University Motorsport Club and Edinburgh University Hillwalking Club, the former of which I've had the great privilege of serving as President, for all the achievements and experiences shared. To those I worked with on the Dynamics subteam at HYPED, and to Anna-Katerina Chabidis, my Student Advisor, for her support throughout my degree.



Alistair I. **Murison**, 9 April 2026

Notation

Variables and symbols

c	–	Surface wave speed
C_D	–	Drag coefficient
g	–	Acceleration due to gravity
h	–	Depth below mean sea level
$H,\ H_s$	–	Significant wave height
k	–	Wave number (spatial frequency)
κ	–	von Kármán constant
λ	–	Wavelength
λ_0	–	Initial wavelength
$\mathcal{N}$	–	Gaussian random process
N	–	Number of prism layers
p	–	Order of convergence
P_{100m}	–	Pressure at a depth of 100 metres
P_{6000m}	–	Pressure at a depth of 6000 metres
P_{atm}	–	Atmospheric pressure
P_{fluid}	–	Fluid pressure
Ra	–	Roughness Average
t	–	time
$T,\ \tau$	–	Spectral wave period
$\mathbf{u}$	–	Flow velocity
$\mathbf{u}'$	–	Turbulent flow velocity variation
u^*	–	Shear velocity
$\mathbf{U}_{\mathrm{c}}$	–	Current flow velocity
$\mathbf{U}_{\mathrm{r\ max}}$	–	Maximum current on a mean day
$\mathbf{U}_{\mathrm{r\ rms}}$	–	Long term mean current

$\mathbf{U}_{r-1}$	–	Regular current with a recurrence period of 1 year
$\mathbf{U}_{r-50}$	–	Regular current with a recurrence period of 50 years
$\mathbf{u}_w, \mathbf{w}_w$	–	Wave particle velocity horizontal and vertical components
x	–	Horizontal coordinate of the wave
y	–	Cross-flow coordinate
y^+	–	Wall distance
z	–	Height above seabed
z_0	–	Roughness length
z_1	–	Reference height above seabed
ρ	–	Density of sea water
σ	–	Standard deviation
ω	–	Wave angular frequency
Δx	–	Average mesh cell spacing

Acronyms and abbreviations

ADCP	–	Acoustic Doppler Current Profiler
CAD	–	Computer Aided Design
CFD	–	Computational Fluid Dynamics
EMEC	–	European Marine Energy Centre
EPDM	–	Ethylene Propylene Rubber
FEA	–	Finite Element Analysis
FoW	–	Fall of Warness
GCI	–	Grid Convergence Index
GDPR	–	General Data Protection Regulation
PEEK	–	Polyether ether ketone
POM-C	–	Polyoxymethylene Copolymer (Acetal C)
SST	–	Shear Stress Transport
TI	–	Turbulence Intensity

Summary of Resources

The majority of work conducted in this project involved computational work. A student licence for STAR-CCM+ was made available through the Computational Fluid Dynamics 5 course at the beginning of this project, and the Student Edition of SOLIDWORKS 2024 was obtained through membership of Edinburgh University Formula Student.

The £250 MEng project budget supplied by the School of Engineering was not used. No technician time was required.

Contents

Personal Statement i

Summary ii

Acknowledgements iii

Notation iv

Summary of Resources vi

List of Figures x

List of Tables xii

1 Introduction 1

1.1 Context and Motivation . . . 1
1.2 Aims and Objectives . . . 1
1.3 Project Constraints . . . 2
1.3.1 Budgetary Constraints . . . 2
1.3.2 Time Constraints . . . 2

2 Literature Review 4

2.1 Passively Aligning Gimbal Solution . . . 4
2.2 Operational Requirements . . . 4
2.3 Payloads . . . 5
2.4 Environmental Location . . . 5
2.5 Environmental Characteristics . . . 6
2.6 Review of Commercial Subsea Actuators . . . 8
2.7 Biofouling . . . 9
2.8 Corrosion and Subsea Materials . . . 10
2.9 Sealing Techniques . . . 11

3 Site Flow Model **12**
3.1 Characterising the flow . . . 12
3.1.1 Current Velocity . . . 13
3.1.2 Waves . . . 14
3.1.3 Turbulence . . . 15

4 Computational Fluid Dynamics Modelling **17**
4.1 Workflow Strategy . . . 17
4.2 Geometry and Domain . . . 18
4.3 Boundary Conditions and Solvers . . . 19
4.4 Meshing strategy . . . 19
4.5 Results Monitoring . . . 21
4.6 Grid Convergence Study . . . 24
4.7 Sensitivity Study . . . 25
4.8 Results . . . 25

5 Housing Design **31**
5.1 Actuator Selection . . . 31
5.2 Actuator Operation and Housing Design Considerations . . . 32
5.2.1 Actuator Description . . . 32
5.2.2 Design Strategy . . . 33
5.3 Housing Design . . . 33
5.3.1 Output Shaft . . . 33
5.3.2 End-cap . . . 37
5.3.3 Rear Housing . . . 39
5.3.4 Assembly . . . 43
5.3.5 Connection to Frame and Gimbal Rings . . . 44
5.4 Actuator Assembly . . . 46
5.4.1 Fasteners . . . 46
5.5 Tolerances . . . 46
5.5.1 Output Shaft . . . 46
5.5.2 End-cap . . . 47
5.5.3 Rear Housing and connector plates . . . 48
5.6 Costs . . . 48
5.6.1 Bill of Materials . . . 48
5.6.2 Labour Costs . . . 49

6 Discussion **50**
6.1 Site Flow Model . . . 50
6.2 CFD Modelling . . . 50
6.3 Housing Design Process . . . 51

7 Conclusion and Further Work **52**
7.1 Conclusion . . . 52
7.2 Next Steps . . . 53

Bibliography **54**

A Interview GDPR Documentation **60**

B CFD Simulation Files **72**
B.1 STAR-CCM+ Simulation Files . . . 72
B.2 Additional CFD Plots . . . 73

C GCI Python Scripts **75**
C.1 grid_refinement.py . . . 75
C.2 GCI.py . . . 82

D Component Technical Drawings **83**

E Manufacture and Testing Objectives **89**

Chapter Word Counts

Chapter	Word Count
Introduction	458
Literature Review	1620
Site Flow Model	1159
Computational Fluid Dynamics Modelling	1871
Housing Design	3517
Discussion	714
Conclusion and Further Work	633
Total	9972

List of Figures

1.1 Project Gantt chart . . . 3

2.1 Previous sensor frame designs . . . 4
2.2 Location of the Orkney Islands and the Fall of Warness . . . 6
2.3 EMEC tidal test locations . . . 6
2.4 Orkney Islands and FoW bathymetry . . . 7
2.5 The unsteady characteristics of turbulent flow . . . 8
2.6 Commercial subsea actuators by Sidus Solutions . . . 9
2.7 Biofouling . . . 10

3.1 Flow over a cavity . . . 12
3.2 Validity of theories for periodic water waves . . . 14

4.1 CFD workflow . . . 17
4.2 Seabed Frame Assembly CAD File in SOLIDWORKS 2024 . . . 18
4.3 Mesh along centreline, base size 0.5 m . . . 20
4.4 Mesh on surfaces, base size 0.5 m . . . 20
4.5 y^+ values along seabed . . . 21
4.6 Horizontal velocity plots at $z = 0.1$ m . . . 22
4.7 Horizontal velocity plots at $z = 0.75$ m . . . 23
4.8 Drag coefficient grid convergence . . . 24
4.9 Moment produced on gimbals and payload - axis of outer gimbal ring . . . 26
4.10 Moment produced on gimbals and payload - axis of inner gimbal ring . . . 26
4.11 Horizontal scalar velocity plots on final simulation . . . 27
4.12 Horizontal vector velocity plot of frame on final simulation, $z = 0.75$ m . . . 28
4.13 Vertical cross-section velocity plots on final simulation . . . 28
4.14 Vertical cross-section velocity plots on final simulation - offset 0.28 metres . . . 29
4.15 Streamlines scalar scene in final simulation . . . 30

5.1 RH-17 actuator . . . 32
5.2 Installation drawing of RH-17 actuator . . . 32
5.3 MacArtney 6-pin SubConn bulkhead connector . . . 33
5.4 Output shaft . . . 35

5.5 Output shaft FEA: Von Mises stresses . . . 36
5.6 Output shaft FEA: displacement . . . 36
5.7 End-cap model in CAD . . . 37
5.8 End-cap FEA: Von Mises stresses . . . 38
5.9 End-cap FEA: Displacement . . . 39
5.10 Rear housing design options . . . 40
5.11 Rear housing FEA: Von Mises stresses . . . 41
5.12 Rear housing FEA: localised stresses at the bulkhead connection . . . 42
5.13 Rear housing FEA: displacement . . . 42
5.14 Actuator components assembled . . . 43
5.15 Exploded view of actuator assembly . . . 43
5.16 Actuator assembly with back plate and threaded rods to pass through frame . . . 44
5.17 Rear connecting plate . . . 44
5.18 Actuator assembly with middle plates for attachment to outer gimbal ring . . . 45
5.19 Middle connecting plate - inner gimbal . . . 45
5.20 Output shaft manufacturing drawing . . . 47

B.1 Azimuth moment about gimbal vertical axis . . . 73
B.2 Horizontal force on payload . . . 74
B.3 Vertical force on payload . . . 74

D.1 Output shaft technical drawing . . . 84
D.2 End-cap technical drawing . . . 85
D.3 Rear housing technical drawing . . . 86
D.4 Rear connection plate technical drawing . . . 87
D.5 Middle connection plate technical drawing . . . 88

List of Tables

2.1 Summary of operational requirements 5
2.2 Payload data 5
2.3 Long-term and extreme flow conditions 7
2.4 Candidate materials for subsea application 10
2.5 Seal options for rotating subsea shafts 11

3.1 Flow conditions values at FoW 13

4.1 Boundary conditions and solvers 19
4.2 Mesh setup 19
4.3 Grid convergence results 24
4.4 Grid Convergence Index (GCI) results 24
4.5 Key results for key flow conditions 25

5.1 MyActuator RH Series performance values 31
5.2 Fasteners required for full assembly - minimum lengths 46
5.3 Bill of Materials 48
5.4 Manufacturing details 49

B.1 List of .sim files used in CFD simulations 72

Chapter 1

Introduction

1.1 Context and Motivation

An important challenge of renewable energy is the reliability of supply associated with wind and solar, and the subsequent issues of energy storage and grid stability [1]. Tidal energy utilises the predictable, constant flow of coastal tidal waters produced by the interaction of the Earth and the Moon's gravitational fields. The Orkney Islands' exposed position off the North coast of Scotland results in great tidal energy potential [2].

Tidal energy development is highly site-specific because performance depends on local bathymetry, topography, and complex current behaviour. These flows are difficult to model accurately, so field measurements remain essential. Acoustic Doppler Current Profiler (ADCP) sensors are used for this purpose [3]. The ability to rotate an ADCP would increase survey flexibility and reduce the number of instruments required.

1.2 Aims and Objectives

This project aimed to design a low-cost, high-performance actuator and housing assembly for subsea ADCP alignment. The system is intended to improve data quality and reliability by calibrating pitch and roll, correcting and holding sensor orientation, and allowing controlled repositioning. The alignment system could also be used to orient multiple sensors for triangulation, increasing the effective survey area.

The project was undertaken alongside Michael Wilson's MEng project on azimuth rotation within the same two-axis gimbal system [4]. Existing commercial subsea actuators are generally designed for either deep-sea oil and gas applications or lower-energy environments and are therefore poorly suited to highly energetic coastal waters up to 100 m in depth. The primary objective was therefore to develop a custom housing that balanced strength, manufacturability, cost, and long-term subsea reliability.

The following objectives were set for this project:

- Develop an engineering design specification for the operating requirements for a subsea actuator and housing suitable for high-energy coastal waters.
- Advance one selected concept to detailed design, including detailed material selection, geometry, sealing techniques, and tolerances.
- Analyse commercial actuators to determine the best balance of cost and torque output.
- Conduct material and structural analysis using software tools such as finite element analysis (FEA) and computational fluid dynamics (CFD) to inform material and geometry choices.

Further objectives regarding manufacturing and testing were proposed (Appendix E), subject to financial and time constraints, but it was decided early in the project to focus on the theoretical design.

1.3 Project Constraints

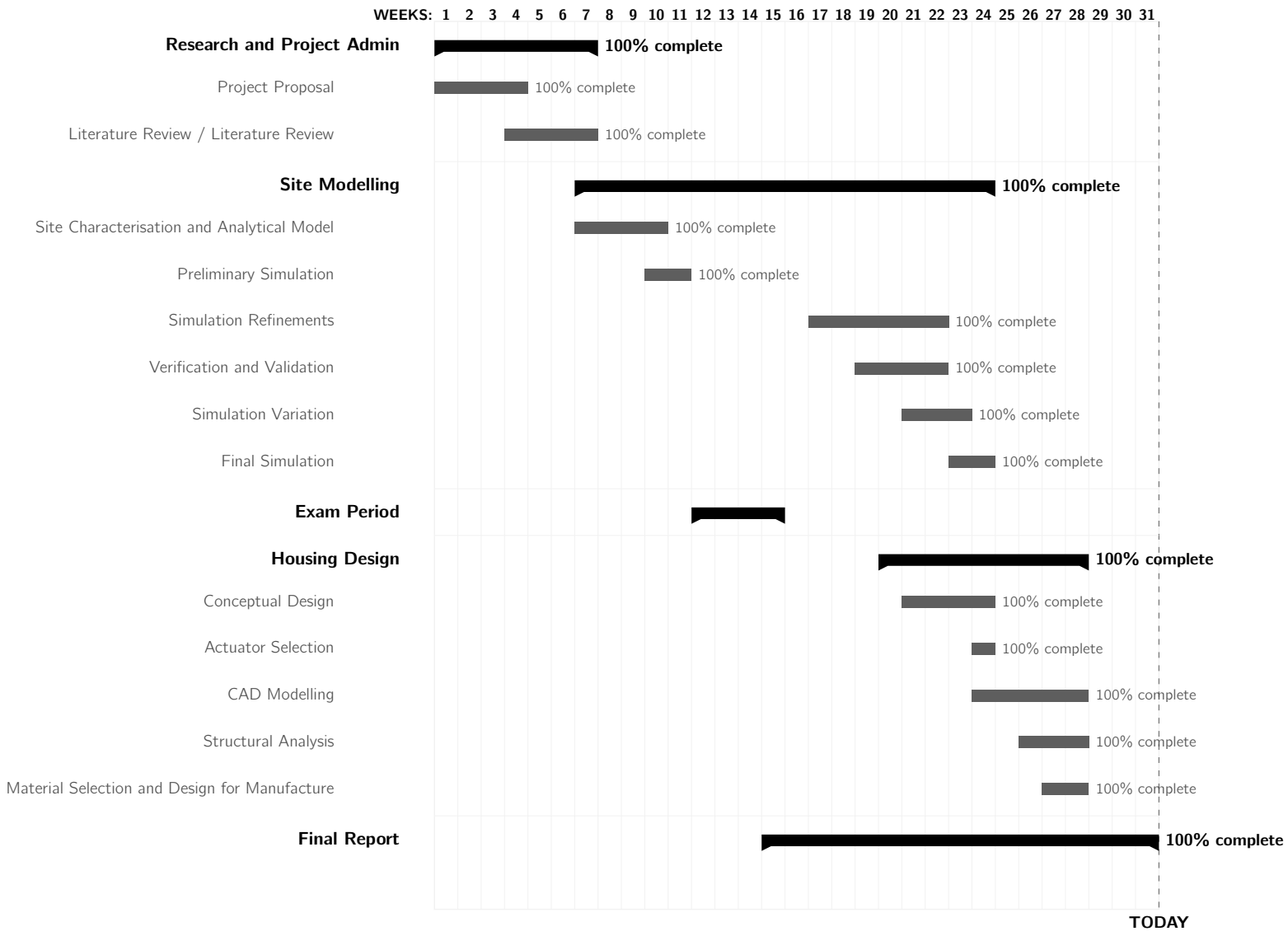
1.3.1 Budgetary Constraints

Funding of £250 was allocated by the School of Engineering, but was not used.

1.3.2 Time Constraints

The project Gantt chart, shown in Figure 1.1, outlines the project's workflow across the academic year. The analytical model and CFD simulations were planned to be completed during the first semester, with the actuator housing design completed in semester 2. As the project progressed, more emphasis was placed on the CFD design.

Figure 1.1: Project Gantt chart



Chapter 2

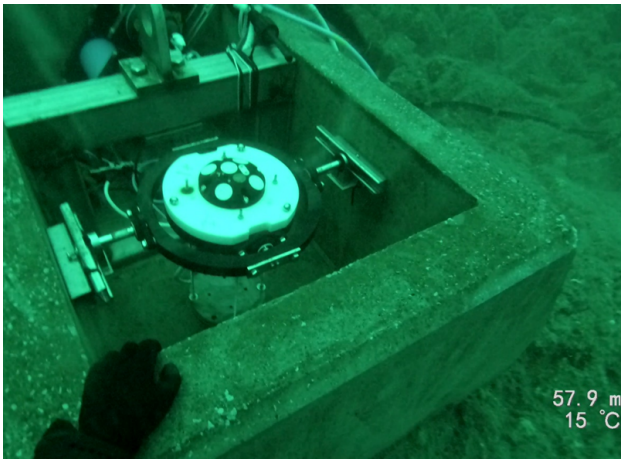
Literature Review

2.1 Passively Aligning Gimbal Solution

Dr Brian Sellar's team has previously trialled multiple sensor-carrying frames. Figure 2.1a shows a sensor held fixed in a steel frame [5]. Figure 2.1b shows the most recent design, with a weighted gimbal set. This makes it a passively damped pendulum system. By fitting an actuator to each gimbal axis, it may be used for sensor alignment and movement.



(a) ADCP sensor fixed in a steel frame



(b) ADCP sensor in a passively aligning gimbal set

Figure 2.1: Previous sensor frame designs

2.2 Operational Requirements

Operational requirements were extracted from an interview with Dr Brian Sellar, conducted in accordance with the University of Edinburgh's GDPR procedures (see Appendix A) and transcribed for use in the project [5] [6]. The main requirements and characteristics of operation are summarised in Table 2.1.

Table 2.1: Summary of operational requirements

Characteristic	Value / description
Calibration motion	90° from vertical in pan and tilt
Calibration frequency	Once per day
Calibration condition	Sensor not recording and not held at extreme conditions
Main operating range	20° from vertical
Measurement duration	24 hours for a minimum of 32 consecutive days
Control cycle	5 minute stationary, reposition typically a few degrees, another 5 minutes stationary
Total adjustments over 32 days	9,216
Holding requirement	No power required to hold against tidal loading
Max design depth	100 m

The aspiration is to leave the system in place for 1 year continuously to reduce the costs of hiring equipment to deploy and retrieve the system. Therefore, power shouldn't be needed to hold the sensor in position against the tidal forces. An actuator with a brake should therefore be used.

2.3 Payloads

The payloads are ADCP sensors: the Sonardyne Origin 600, Nortek Signature 500, and Teledyne Workhorse II [7] [8] [9]. Their key characteristics are outlined in Table 2.2. Sonardyne's Origin 600 is the largest and heaviest is used as the design basis.

Table 2.2: Payload data

Manufacturer	**Sonardyne**	**Nortek**	**Teledyne Marine**
Product	Origin 600 Dual Battery	Signature 500	Workhorse II
Height [mm]	388	274	216
Diameter [mm]	244	228	228
Mass in water [kg]	7.9	1.45	3.5
Beam Angle [°]	25	25	20
Pan and Tilt Accuracy [°]	±1	±2	±0.3

2.4 Environmental Location

The deployment location is the Fall of Warness (FoW) in Orkney, shown in Figure 2.2. FoW is an open-sea tidal testing site operated by the European Marine Energy Centre (EMEC), chosen for its high velocity currents, which can reach 4 m/s during spring tides [10]. The Orkney region has high wave energy potential, with similar sites at Billa Croo, Scarpa Flow and Shapinsay Sound, shown in Figure 2.3 [11].

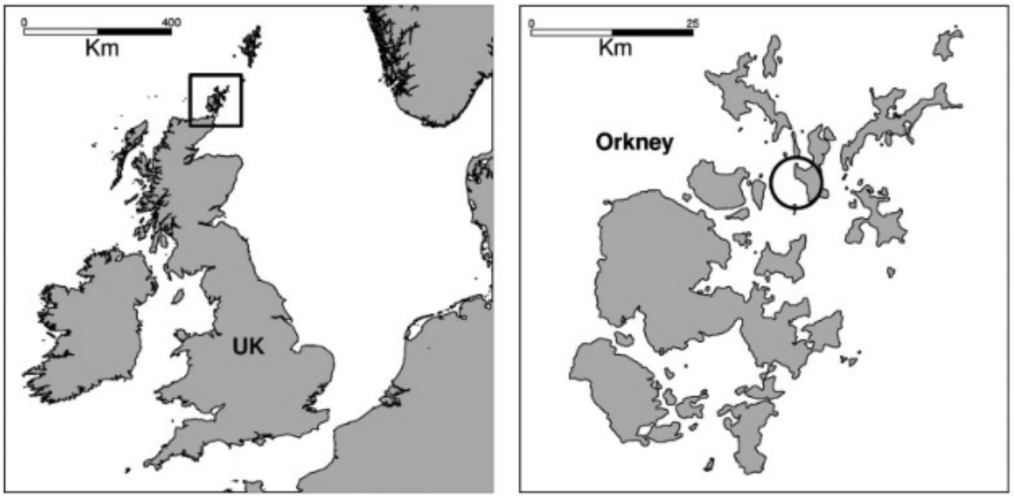


Figure 2.2: Location of the Orkney Islands (left) and the Fall of Warness (right)



Figure 2.3: EMEC tidal test locations

2.5 Environmental Characteristics

Depths at FoW range from 12 m to 54 m, shown in Figure 2.4 [12]. A depth of 50 metres is used for flow calculations. The sub-littoral environment north and east of the deep basin contains thick deposits of boulders, gravel, and interstitial shelly sand according to surveys [13]. These materials are reported to be well covered with flora and fauna, indicating stability and minimal transport of sand or gravel during water movement.

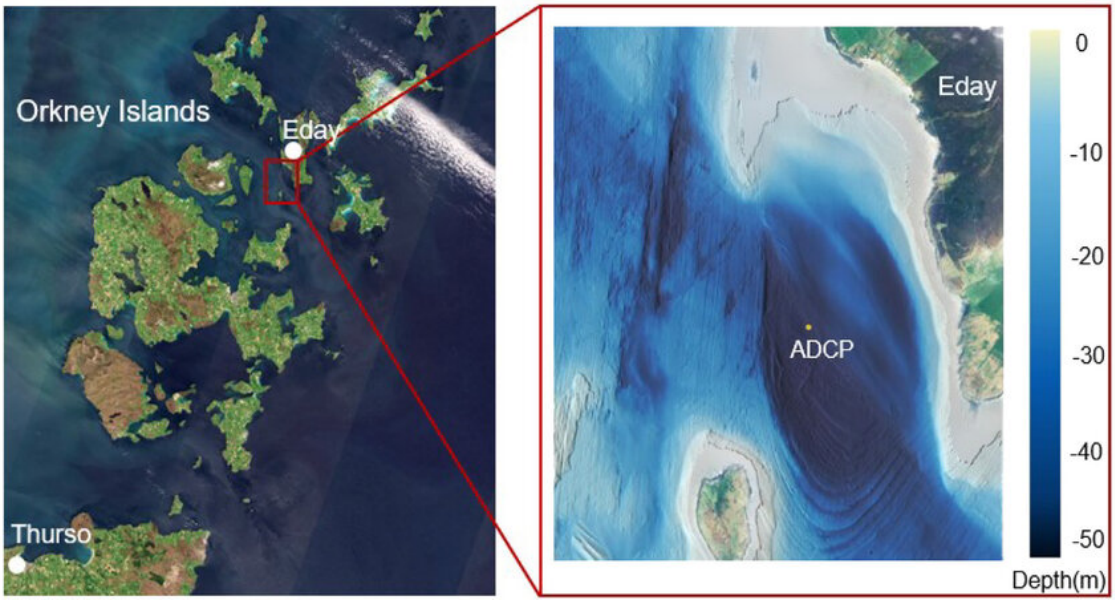


Figure 2.4: Orkney Islands (left) with FoW bathymetry (right), the yellow dot marks the location of an ADCP in the source publication

The University of Edinburgh's Open Data for Tidal Energy service provides papers and data relating to FoW, including from the Realtide and ReDapt projects [14]. This includes data on long-term and extreme tidal flow conditions, summarised in Table 2.3.

Table 2.3: Long-term and extreme flow conditions

Long term tidal flow conditions		
$U_{r\ rms}$	Long term mean current	1.804 m/s
$U_{r\ max}$	Maximum current on a mean day	2.42 m/s
ρ_{water}	Sea water density	1027 kg/m^3
Extreme tidal flow conditions		
U_{r-1}	Regular current with a recurrence period of 1 year	3.911 m/s
U_{r-50}	Regular current with a recurrence period of 50 years	4.212 m/s

Flow speeds can be used to model the flow's interaction with the ADCP system by scaling on the velocity profile. The flow speed is the sum of the current flow as a function of depth, wave orbital velocities, and turbulent eddies, shown in Figure 2.5 [15]. It is not within the scope of this project to devise a fully accurate model of turbulence at FoW.

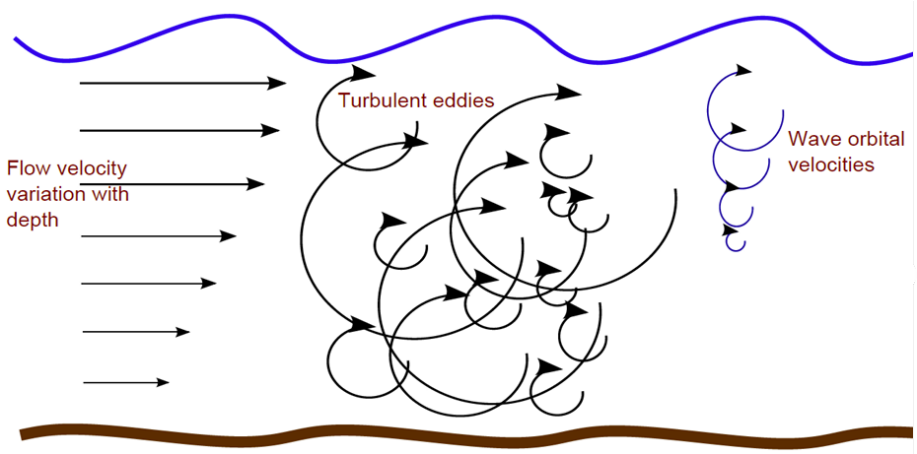


Figure 2.5: The unsteady characteristics of turbulent flow

2.6 Review of Commercial Subsea Actuators

Several pan and tilt subsea actuators have been tested but deemed unsuitable for use in high-energy coastal environments for two reasons. These were products from Sidus Solutions and Arctic Rays, the latter of which is no longer produced [16].

First, the actuators were back-drivable and did not fix in position when unpowered. Requiring continuous power to resist tidal loading is undesirable for a system intended for long subsea deployment with limited onboard power.

Secondly, the available products were primarily designed for deep-sea oil and gas applications. They are rated for much deeper depths and higher pressures, meaning they are over-engineered and thus more expensive than necessary. For example, the Sidus SS109HT Pan & Tilt (Figure 2.6a) is rated to 6000 metres [17]. Equations 2.1 and 2.2 quantify the differences in pressure resistance required [18]. The density of seawater is 1025 kg/m^3 [19].

$$P_{100\text{m}} = P_{\text{atm}} + P_{\text{fluid}} = P_{\text{atm}} + \rho_{\text{sea water}}\, g\, h = 101,325 + 1025 \times 9.81 \times 100 = 1.107 \text{ MPa} \quad (2.1)$$

$$P_{6000\text{m}} = 101,325 + 1025 \times 9.81 \times 6000 = 60.432 \text{ MPa} \quad (2.2)$$

The Sidus SS109HT is a combined pan and tilt actuator. The integration of actuators into the existing passive gimbal design would require individual actuators for the pan and tilt axes, such as the Sidus SS350 Heavy Duty Subsea Rotator (Figure 2.6b).



(a) Sidus SS109HT Pan & Tilt **(b)** Sidus SS350 Heavy Duty Subsea Rotator

Figure 2.6: Commercial subsea actuators by Sidus Solutions

The housing material of the Sidus SS109HT and SS350 are anodised 6061-T6 aluminium with 316 stainless steel fasteners. Depth ratings are 30 m air-filled, 3000 m oil-filled with internal pressure compensation, and 6000 m with external compensation [20]. It is an aspiration that the designed actuator be air-filled to reduce cost and depth rated to 100 m [5]. SS109HT has a maximum output torque of 19 Nm per axis, while SS350 has a maximum of 88 Nm. The Sidus SS109HT costs $10,000 (£7,600) while a similar product from Arctic Rays costs $6,000 (£4,560).

2.7 Biofouling

Biofouling is the build-up of microorganisms, algae, plants, or small animals on wetted surfaces, and can reduce mechanical performance. It develops in two stages: Microfouling is when a biofilm forms on the material surface, while macrofouling is the attachment of organisms such as seaweed, coral and barnacles [21].

The severity depends on temperature, geographical location, solar radiation, and the local flow field. Water velocity and recirculation around the ADCP frame are therefore expected to influence the areas most susceptible to fouling.

Reports from FoW suggest that fouling may not be severe. The ReDAPT report noted only superficial algal growth and crustaceans on the DEEP-Gen IV turbine (2.7a) after 6 months, which were easily removed by pressure washing [22]. Biofouling can occur on the transducers of ADCPs (Figure 2.7b). Oceanographers often use a mix of Vaseline and chilli powder, which is effective [5]. Many paints can be used for biofouling prevention, but few have the physical, chemical, and toxicological properties required for effective antifouling [23].



(a) Biofouling on the University of Edinburgh's thruster mounted instrumentation rack



(b) Biofouling on a recovered ADCP

Figure 2.7: Biofouling

2.8 Corrosion and Subsea Materials

Subsea devices are subjected to harsh, corrosive seawater environments with high salinity, temperature changes, biological activity, and physical factors such as rapid fluid flow and sand impact, leading to erosion-corrosion. Advantages and limitations of common marine materials are outlined in Table 2.4.

Table 2.4: Candidate materials for subsea application

Material	Advantages	Limitations
Titanium	Excellent corrosion resistance through a stable oxide film; good stress-corrosion cracking resistance; strong mechanical properties [24].	High material cost; difficult and expensive to machine [25].
Stainless steel 316	Baseline marine stainless steel; better corrosion resistance than 304 because of molybdenum addition [26].	Still susceptible to pitting and crevice corrosion in chloride environments; good protection requires a fine surface finish [27].
PEEK	Excellent chemical resistance and mechanical properties; used in extreme oil-and-gas environments [28] [29].	High cost.
Acetal (POM-C)	Good machinability, low moisture absorption, good dimensional stability; copolymer has better hydrolysis resistance than homopolymer grades [30].	Creep under sustained load (can be combined with other materials [31]).

For stainless steel, surface finishes no coarser than Ra 0.5 µm are recommended to restrict corrosion. For polymer components, the main issues are water uptake, property retention, creep, and chemical stability.

2.9 Sealing Techniques

Rotary seals will be required between the actuator housing and the actuator shaft. Important considerations are the pressure differential, lubrication, effectiveness at preventing leakage and contamination ingress. The primary options for sealing are:

Table 2.5: Seal options for rotating subsea shafts

Seal type	Main advantages	Main limitations
Radial lip seal	Compact, low cost, widely used for rotary shafts [32] [33].	Contact seal; generates friction and wear; performance depends on lubrication and surface finish.
Mechanical face seal	Highest-integrity option for harsh environments.	Large, expensive, and dependent on a lubricating film; debris at the seal face can reduce performance [34].
Bearing isolator seal	Non-contact, low drag, good for retaining lubricant and excluding ingress [34].	Cannot seal large pressure differentials on its own.
Dynamic O-ring	Compact, low cost, suitable for low-speed or intermittent duty.	Not suitable for continuous rotation; sensitive to poor shaft finish and runout [33] [34].

O-rings and lip seals are both well-suited for a low-cost subsea housing, given the very low duty cycles. Mechanical face seals are preferred where the former are inadequate. Multi-barrier arrangements are common for harsh marine environments. The primary suppliers are Trelleborg, SKF, and Parker.

Chapter 3

Site Flow Model

3.1 Characterising the flow

The actuator must hold the payload against the tidal loading at FoW. To estimate the torque requirement, the flow around the payload, gimbal rings, and the frame must first be described analytically before being modelled. It is hypothesised that incoming horizontal flow would be pushed up at an angle by the flow striking the flat front of the frame, with recirculation generated within it, as in classical cavity flow (Figure 3.1) [35]. This was consistent with deployment observations that the payload was disturbed despite sitting below the top of the frame.

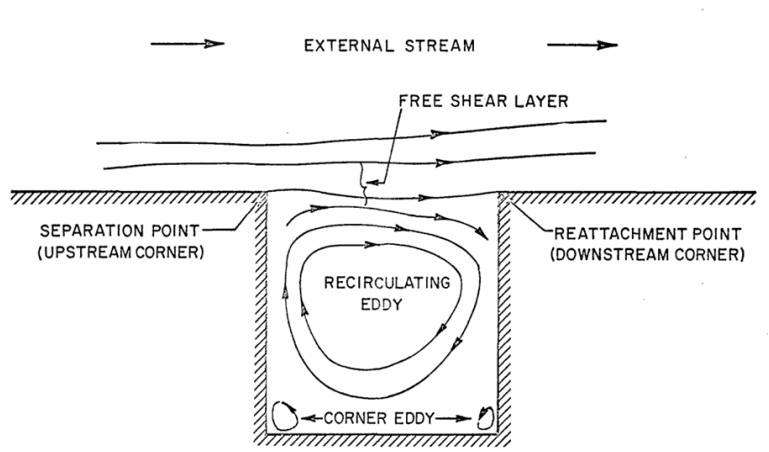


Figure 3.1: Flow over a cavity

The flow is turbulent. As per Figure 2.5, the three primary contributors to turbulent flow are: the current driven by the strong ebb and flow tides, and wave orbital velocities, which both vary with depth, and turbulent eddies, which vary in both depth and time. The water velocity is the sum of these three, shown in Equation 3.1. z is the height above the seabed, and t is time. A full turbulence model for FoW was beyond scope, so a simplified analytical model was developed instead.

$$\mathbf{u}(z,t) = \underbrace{\mathbf{U}_c(z)}_{\text{current flow}} + \underbrace{\mathbf{u}_w(z)}_{\text{waves}} + \underbrace{\mathbf{u}'(z,t)}_{\text{turbulence}} \tag{3.1}$$

FoW site studies show that flow profiles for flood tides follow a logarithmic profile, while ebb tides follow a parabolic flow profile [36].

Long-term mean flow condition values, most likely to be experienced by the actuator, as well as the 1-year and 50-year recurrence values, the extreme values expected once in those time frames, are available through the 2011 ReDAPT report [22]. Current velocity $\mathbf{U}_c$, significant wave height H_s, and spectral period T (or τ) are given and shown in Table 3.1 [22]. The long term mean current velocity is given as the maximum current on a mean day.

Table 3.1: Flow conditions values at FoW

	Long term mean	**1-year recurrence**	**50-year recurrence**
Current velocity [m/s]	2.420	3.911	4.212
Significant wave height [m]	1.11	3.9	5.2
Spectral Period [s]	4.2	9.1	10.4

For design, the 1-year recurrence values are used as a conservative case, as 50-year recurrence values would likely lead to over-engineering and unnecessary cost. Significant wave height is the average of the highest one-third of waves, representing the typical wave conditions. Spectral period represents the dominant energy-carrying waves.

3.1.1 Current Velocity

The 1/7th power law provides an approximate relationship between current velocity and depth, but it is purely empirical and not derived from physics. It performs poorly in the boundary layer region and near the seabed, where the payload is located.

The von Kármán-Prandtl (log-law) profile shown in Equation 3.2 is more accurate in this region, derived from the Reynolds-averaged momentum equation, and accounts for seabed roughness and shear stresses in this region. u^* is the shear velocity, κ is the von Kármán constant ($\kappa \approx 0.41$), and z_0 is the roughness length, approximately 0.01 m for rough bedrock seabeds like FoW [37] [38] [39]. z is positive upwards from the seabed. This relationship, like the power law, assumes a smooth velocity profile.

$$\mathbf{U}_c(z) = \frac{u^*}{\kappa} \ln\left(\frac{z}{z_0}\right) \tag{3.2}$$

As a reference, based on current profile data from Red Wharf Bay, a sandy bay in Anglesey, $u^* = 2.2$ cm/s [39]. The value for FoW is expected to be much higher due to the maximum regular current of 3.9 m/s and water depths up to 50 m. Setting $z = 50$ m and $\mathbf{U}_c(z) = 3.911$ m/s in Equation 3.2 as per Table 3.1, the shear velocity is found to be 18.8 cm/s, as shown in Equation 3.3.

$$u^* = \frac{\mathbf{U}_c(z)\,\kappa}{\ln(z/z_0)} = \frac{3.911 \times 0.41}{\ln(50/0.01)} = 0.188 \text{ m/s} \tag{3.3}$$

$$\Rightarrow \quad \mathbf{U}_c(z) = 0.459 \ \ln\left(\frac{z}{0.01}\right) \tag{3.4}$$

Alternatively, a method without the shear velocity u^* and von Karman's constant κ can be derived as follows, where one current velocity $\mathbf{U}_c(z_1)$ is already known:

$$\frac{\mathbf{U}_c(z)}{\mathbf{U}_c(z_1)} = \frac{(u^*/\kappa)\ \ln(z/z_0)}{(u^*/\kappa)\ \ln(z_1/z_0)} = \frac{\ln(z/z_0)}{\ln(z_1/z_0)} \quad \Rightarrow \quad \mathbf{U}_c(z) = \frac{\mathbf{U}_c(z_1)}{\ln(z_1/z_0)} \ \ln\left(\frac{z}{z_0}\right) \tag{3.5}$$

Using Equation 3.5, the same result as derived in Equation 3.4 is found.

3.1.2 Waves

Multiple theories exist for different depth, wave height and period combinations as shown in Figure 3.2. For the three flow conditions given in Table 3.1, Stokes 2nd order wave theory is the appropriate theory to use [40].

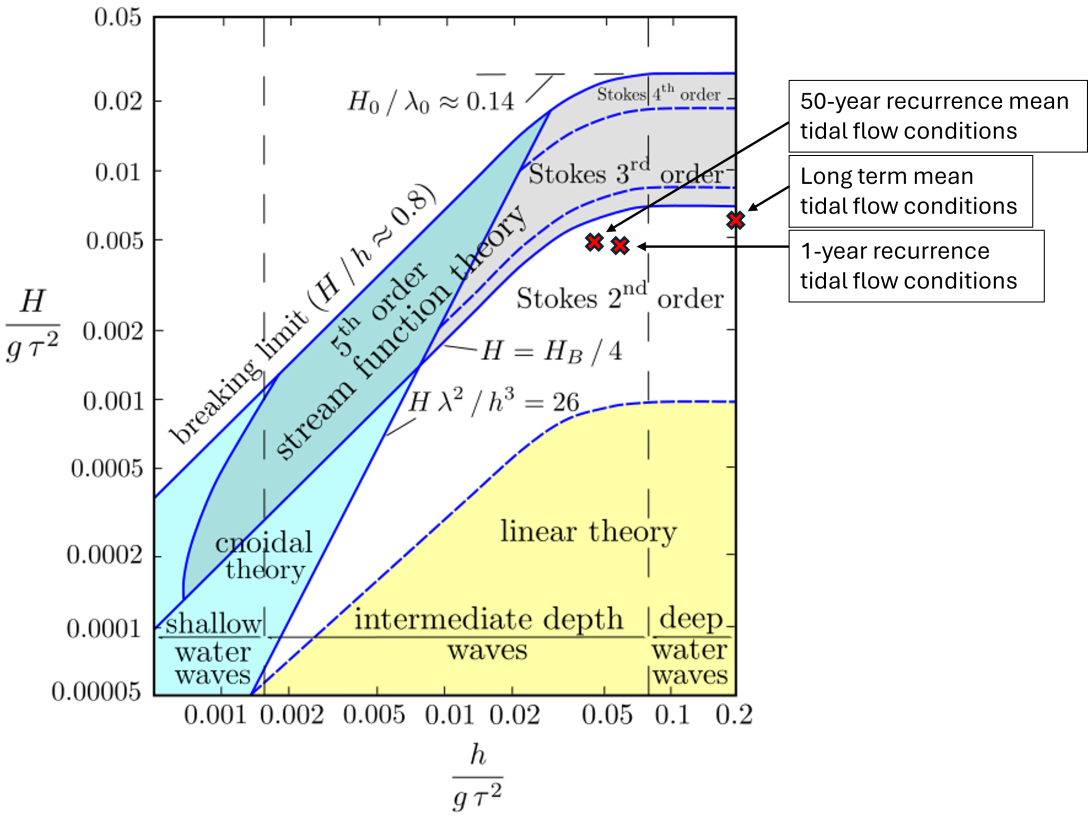


Figure 3.2: Validity of theories for periodic water waves

Equations for the horizontal and vertical particle velocities, $\mathbf{u}_w$ and $\mathbf{w}_w$ are shown by Equation 3.6 and 3.7 [41]. H is the significant wave height, ω is the wave angular frequency (rad s^{-1}), k is the wave number (or spatial frequency), and x is the horizontal coordinate of the wave. λ is the wavelength, c the surface wave speed, and h is water depth. The 1-year recurrence values (Table 3.1) are used.

$$\mathbf{u}_w(z) = \frac{gH}{2c}\frac{\cosh(kz)}{\cosh(kh)}\cos(kx-\omega t) + \frac{3}{16}ck^2H^2\frac{\cosh(2kz)}{\sinh^4(kd)}\cos[2(kx-\omega t)] \tag{3.6}$$

$$\mathbf{w}_w(z) = \frac{gH}{2c}\frac{\sinh(kz)}{\cosh(kh)}\sin(kx-\omega t) + \frac{3}{16}ck^2H^2\frac{\sinh(2kz)}{\sinh^4(kd)}\sin[2(kx-\omega t)] \tag{3.7}$$

$$k = 2\pi/\lambda \tag{3.8}$$ $$\omega = 2\pi/T \tag{3.9}$$ $$c = \omega/k \tag{3.10}$$

Wavelength λ is found iteratively using Equation 3.11, with an initial wavelength guess of $\lambda_0 = 100$ m. After five iterations, the difference between iterations is less than 0.01 m, $\lambda = 127.44$ m.

$$\lambda = \frac{gT^2}{2\pi}\tanh\left(\frac{2\pi h}{\lambda}\right) \tag{3.11}$$

The wave angular frequency is calculated using Equation 3.9. This gives $\omega = 0.690$ rad s^{-1}. Using Equation 3.8 and 3.10, the wave number is $k = 0.0493$ m^{-1}, and wave speed 13.996 ms^{-1}. As $kh = 2.465$, or $\mathcal{O}(1)$, the depth is considered intermediate [42]. For the long term mean values, it is considered deep water.

Equations 3.6 and 3.7 describe the horizontal and vertical wave particle velocities. The kx term is dropped, as only the velocity as a function of depth at a fixed point in the horizontal direction is of interest. The vertical particle velocity is later used in the CFD inlet condition.

$$\mathbf{u}_w(z) = 1.367\frac{\cosh(0.0496z)}{\cosh(2.465)}\cos(0.690t) - 0.0981\frac{\cosh(0.0986z)}{\sinh^4(2.465)}\cos(1.380t) \tag{3.12}$$

$$\mathbf{w}_w(z) = -1.367\frac{\sinh(0.0496z)}{\cosh(2.465)}\sin(0.690t) - 0.0981\frac{\sinh(0.0986z)}{\sinh^4(2.465)}\sin(1.380t) \tag{3.13}$$

3.1.3 Turbulence

Turbulence intensity (TI) is a maximum of 9.1% ±1.9% at FoW, decreasing by 15-30% in magnitude by mid-depth across flood and ebb tides [36]. TI is therefore taken as 9%. TI is defined in Equation 3.14 where u' is the RMS turbulent velocity fluctuation, which can be assumed equal to the standard deviation σ.

$$\text{TI} = \frac{u'}{\mathbf{U}_c} = \frac{\sigma}{\mathbf{U}_c} \quad \Rightarrow \quad u' = \sigma = 0.09\,\mathbf{U}_c \tag{3.14}$$

The turbulent fluctuations can be modelled as a Gaussian random process with zero mean and a standard deviation equal to 9% of the mean current velocity, as shown in Equation 3.15.

$$\mathbf{u}'(z) \approx \mathcal{N}\big(0,\ (0.09\ \mathbf{U}_c)^2\big) \tag{3.15}$$

Equation 3.16 presents the full analytical equation describing the horizontal turbulent flow at FoW for a total depth of 50 m. Vertical flow is given by Equation 3.13, plus Equation 3.15. These provide a simplified, depth-dependent representation of the FoW flow suitable for CFD boundary conditions.

$$\begin{aligned}\mathbf{u}(z,t) = 0.459\ \ln\!\left(\frac{z}{0.01}\right) + 1.367\ \frac{\cosh\left(0.0496z\right)}{\cosh\left(2.465\right)}\cos\left(0.690t\right) \\ - 0.0981\ \frac{\cosh(0.0986z)}{\sinh^4\left(2.465\right)}\cos\left(1.380t\right) + \mathcal{N}\left(0,\ \left(0.0413\ \ln\!\left(\frac{z}{0.01}\right)\right)^2\right)\end{aligned} \tag{3.16}$$

Chapter 4

Computational Fluid Dynamics Modelling

Flow around the payload and frame was simulated using STAR-CCM+, a commercial CFD solver [43]. STAR-CCM+ was selected because it provides greater accuracy, mesh control, turbulence modelling, and boundary-layer resolution than CAD-integrated software, making it better suited to resolving flows around complex geometries.

4.1 Workflow Strategy

The CFD workflow was iterative as errors and new information were found. A linear simplification is shown in Figure 4.1. A preliminary model was created using an initial selection of physics models, mesh settings, and domain dimensions. Results were used to refine the setup parameters. Once a stable refined model had been obtained, a grid convergence study and a sensitivity study were performed for verification. The verification quantity used was the drag coefficient, chosen because it is a non-dimensional global quantity that combines pressure and viscous forces. As many simulation files were produced, the purposes of each are listed in Appendix B.

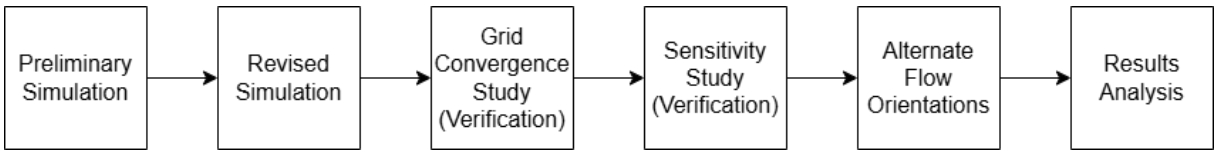


Figure 4.1: CFD workflow

4.2 Geometry and Domain

Dr Brian Sellar provided existing CAD models of the frame and the passively aligning gimbal system. The full assembly was simplified before simulation to reduce computational cost (Figure 4.2). Components that did not affect actuator loading were removed, and small geometric features such as minor holes were suppressed as the solver could only capture their effect with an extremely fine mesh.

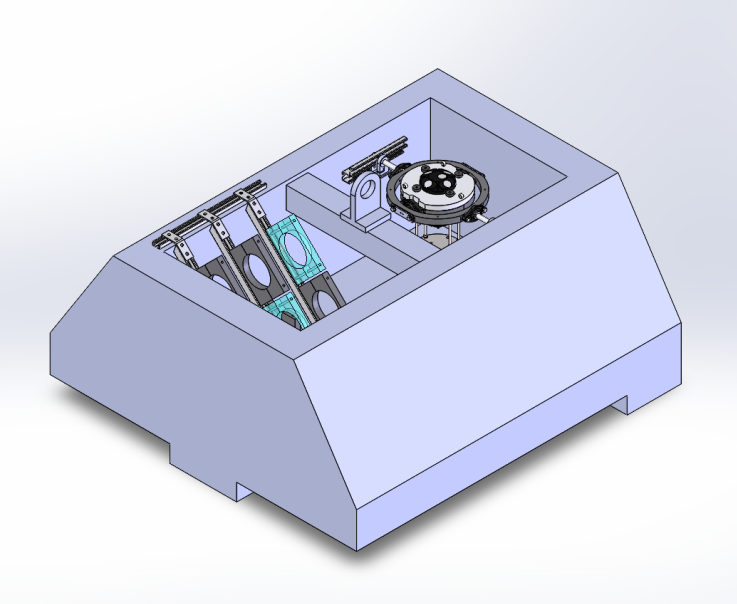


Figure 4.2: Seabed Frame Assembly CAD File in SOLIDWORKS 2024

The initial domain dimensions were based on multiples of the frame geometry:

- upstream length: 4 frame lengths
- downstream length: 12 frame lengths
- lateral clearance: 4 frame widths
- vertical clearance: 5 frame widths

The resulting blockage ratio was 2.93%, intended to minimise boundary effects while allowing wake and recirculation regions to fully develop. A half-model symmetry approach was trialled to halve computational cost, but preliminary runs produced unresolvable errors, so a full model was used. The results showed some asymmetric flow, so a full domain was appropriate.

4.3 Boundary Conditions and Solvers

Table 4.1: Boundary conditions and solvers

Boundary / Solver	Setup
Inlet	Velocity inlet, periodic horizontal and vertical components as defined in Equations 3.16 and 3.13
Outlet	Pressure outlet, to drive flow
Sides and top	Symmetry planes, to avoid lateral confinement
Floor	No-slip wall with roughness 0.01 m, to replicate the seabed
Solver	Segregated incompressible solver
Turbulence model	k-ω SST
Time	Implicit unsteady

Table 4.1 shows the boundary conditions and physics conditions used. The k-ω SST model handles separation, flow curvature and strong pressure gradients better than the k-ϵ model, which performs well for external flows and free streams. The SST (Shear Stress Transport) model combines both models, reducing their individual limitations. Inlet velocity and dynamic pressure were set using field functions.

4.4 Meshing strategy

Table 4.2: Mesh setup

Parameter	Value
Initial base size	0.5 m
Cell target size	20% of base
Cell minimum size	5% of base
Prism layers	Seabed only
Number of prism layers, N	25
Prism stretching	1.5
Prism total thickness	0.2 m
Frame surface target size	5% of base
Gimbal ring and payload target size	5% of base
Volumetric control around frame	5% of base
Inlet and outlet mesh	Coarsened to 100% of base

Table 4.2 shows the mesh parameters used. Surface and volumetric refinement are used to increase resolution and capture flow features around and inside the frame, as shown in Figures 4.3 and 4.4. Prism layers are not used around the frame because the flow was highly turbulent and included

motion normal to the wall. Prism layer settings were informed by wall distance y^+ plots (Figure 4.5) along the seabed and boundary layer visualisation. The number of prism layers is set to $N = 25$, the minimum recommended amount for $y^+ < 1$ resolution required by the k-ω SST model [44].

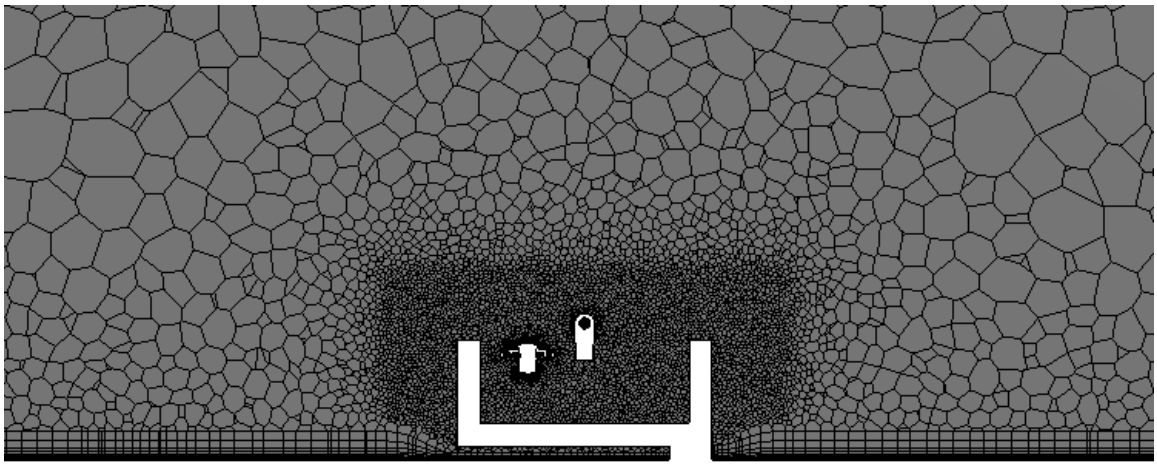


Figure 4.3: Mesh along centreline, base size 0.5 m. File: Full Model Simulation V2.2.sim

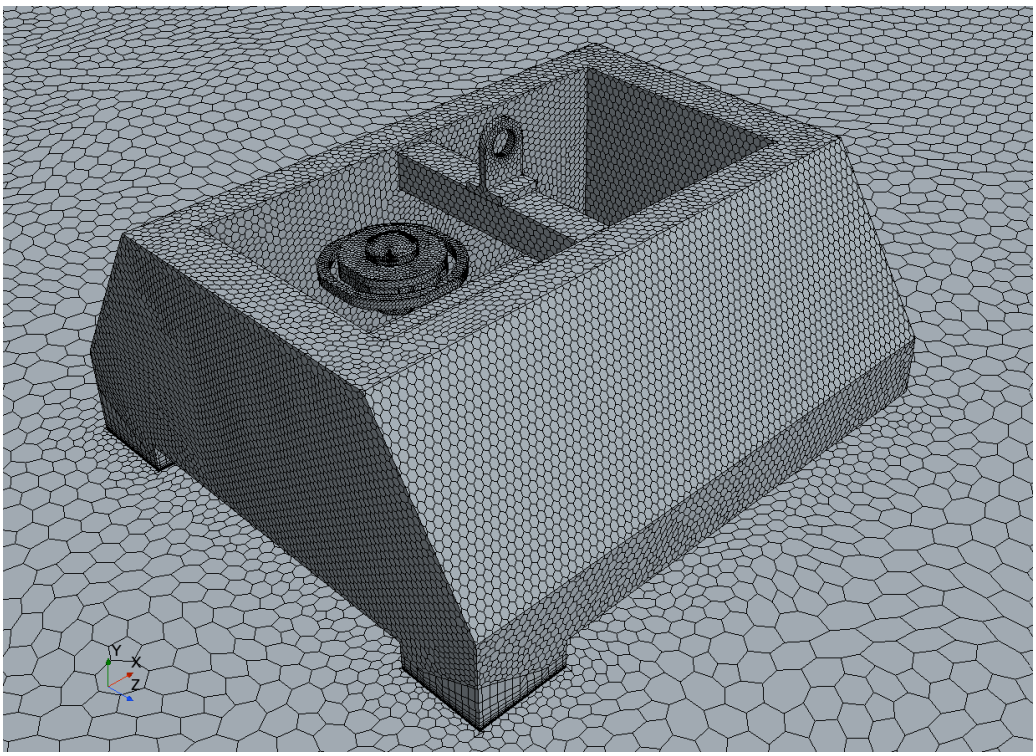


Figure 4.4: Mesh on surfaces, base size 0.5 m. File: Full Model Simulation V6 Long Term Mean.sim

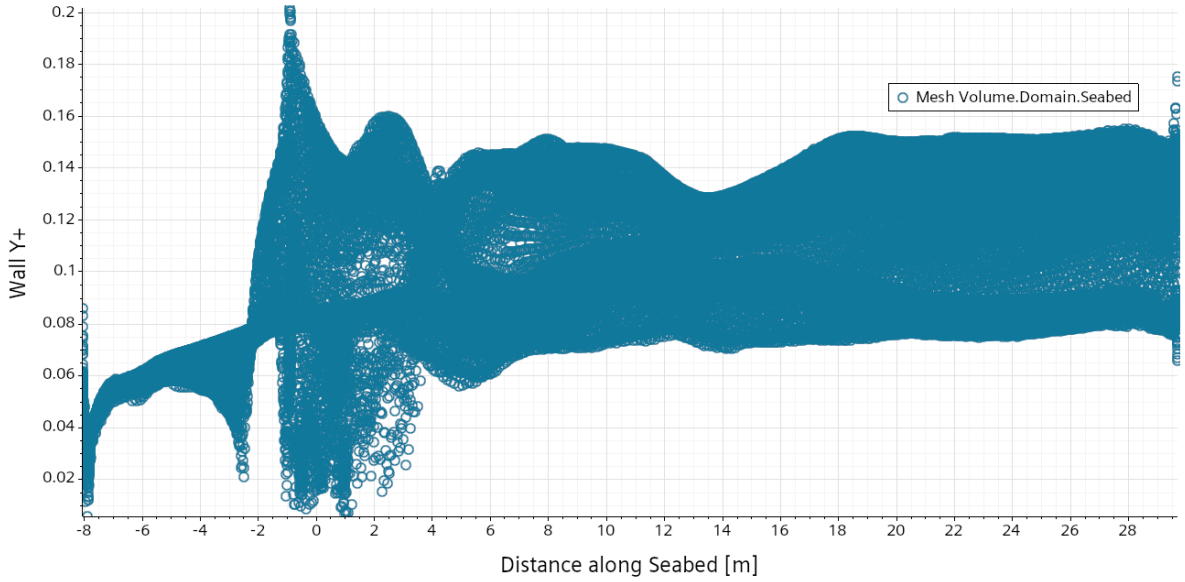


Figure 4.5: y^+ values along seabed. File: Full Model Simulation V2.2.sim

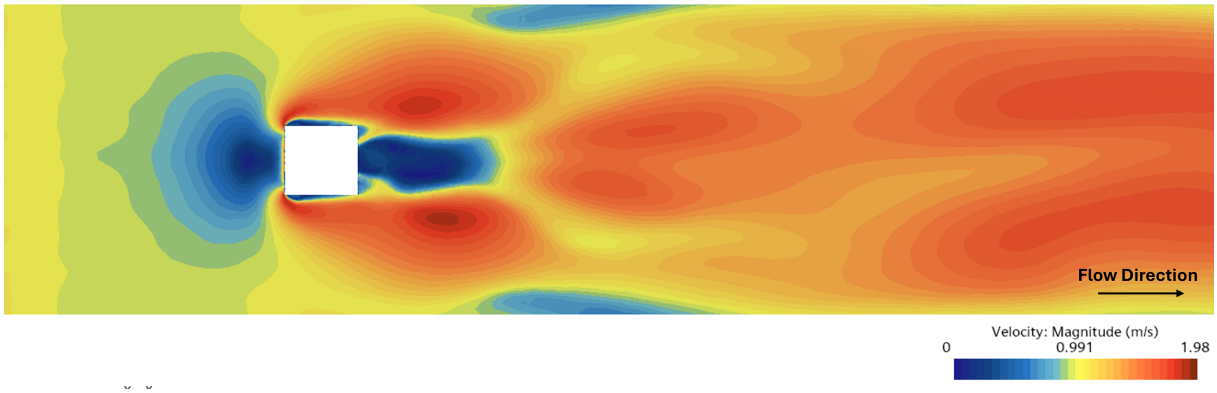
4.5 Results Monitoring and Preliminary Refinement

The following outputs were used throughout the simulation process:

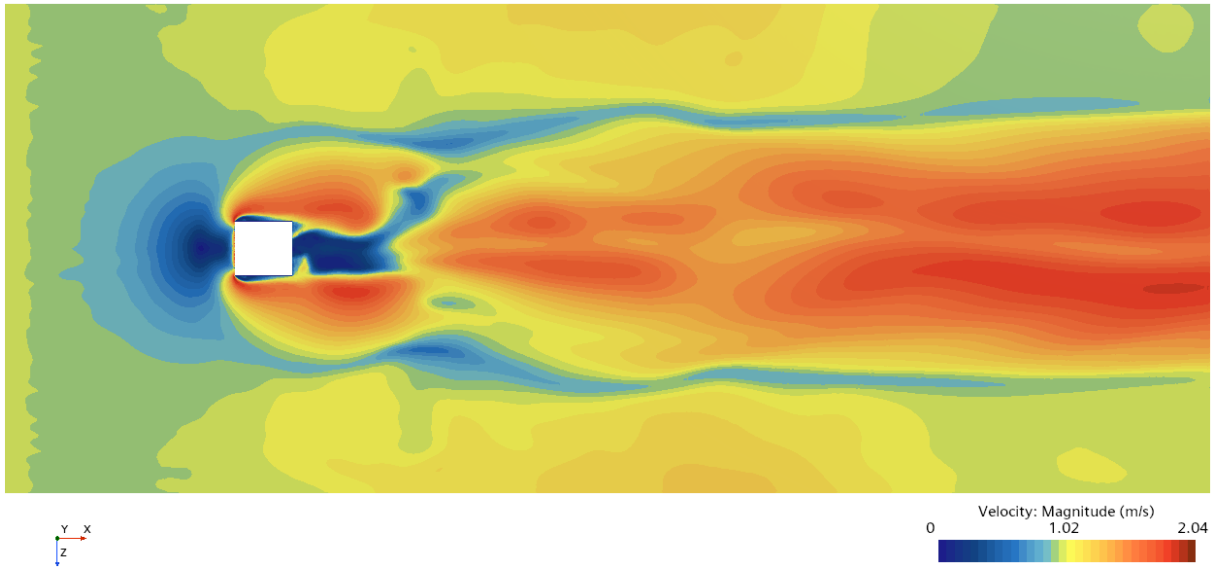
- Residual plots to assess convergence
- Scalar section planes to inspect velocity and pressure.
- Monitor plots for recording critical gimbal and payload moment forces, and drag coefficient for verification.
- Velocity vector section planes, and streamline scalar scene for flow visualisation.
- Seabed plots of y^+, pressure and skin friction for validation and refinement.
- Line probes to verify the inlet profile.

Additional force and moment monitors were produced to assist Michael Wilson's MEng project (Appendix B) [4].

Preliminary simulations showed notable velocity gradients at domain sides, including flow normal to them. This led to the enlargement of the domain. The difference in results can be seen between Figures 4.6 and 4.7. The domain width is doubled to 15.3 metres, length increased to 37.8 metres, and height maintained at 5.04 metres. Note as the simulations are transient, the velocity values in the different domains can not be compared. Flow direction is left to right in all velocity plots.

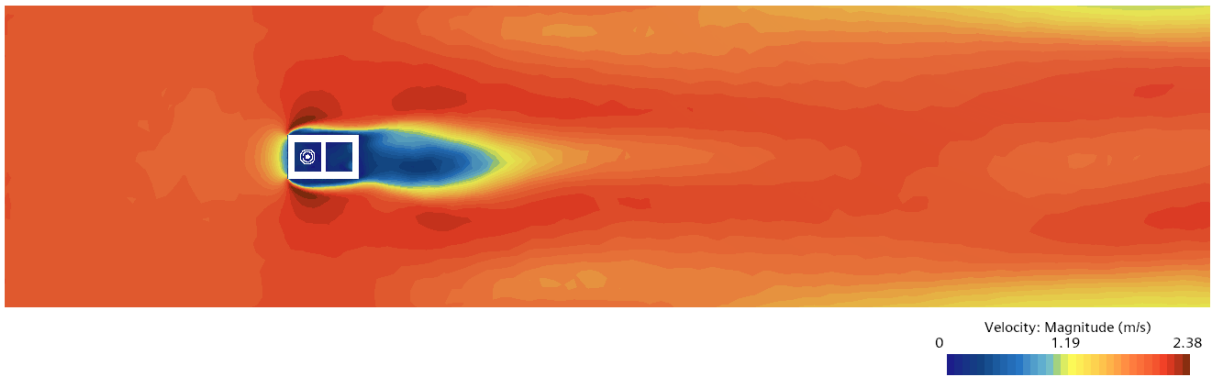


(a) Original domain size. File: Full Model Simulation V2.1_1m base.sim

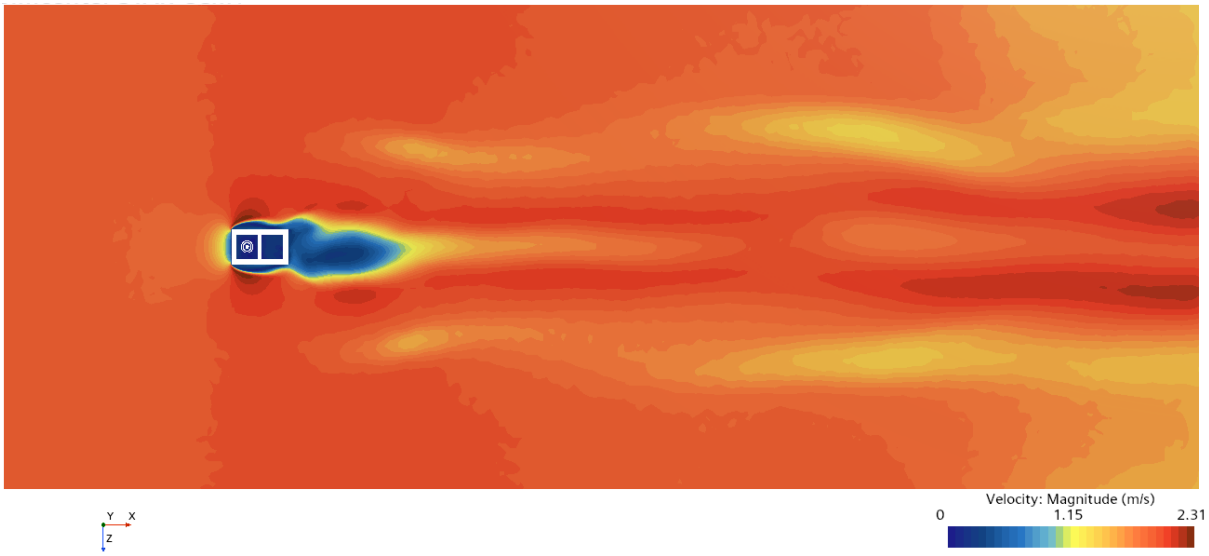


(b) Larger domain size. File: Full Model Simulation V2.2.sim

Figure 4.6: Horizontal velocity plots at $z = 0.1$ m



(a) Original domain size. File: Full Model Simulation V2.1_1m base.sim



(b) Larger domain size. File: Full Model Simulation V2.2.sim

Figure 4.7: Horizontal velocity plots with enlarged domain size

4.6 Grid Convergence Study

Mesh independence was verified by recording the drag coefficient C_D on three different mesh sizes. As the 0.5 m base size was more computationally expensive than expected, coarser grids were tested rather than refining further. The base size was doubled for each grid: 1 m and 2 m. Surface and volumetric refinements scaled with the base size, while prism layer values were kept absolute.

Since the simulation was periodic, the representative drag coefficient for each mesh was taken as the mean of the latest three peaks and troughs after convergence. Average cell spacing, Δx, was calculated from the cube root of mesh volume divided by the cell count. The convergence results are shown in Figure 4.8, and Tables 4.3 and 4.4, produced using a modified version Python script [45].

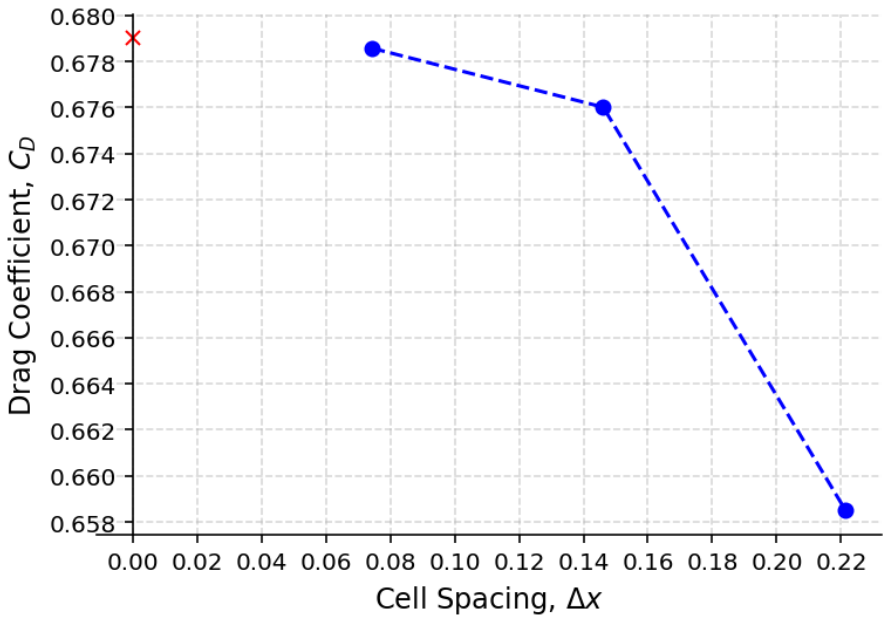


Figure 4.8: Drag coefficient grid convergence

Table 4.3: Grid convergence results

Grid	Δx ratio	Refinement ratio	C_D
1	0.0744	2.0	0.678577
2	0.1461	1.5	0.676016
3	0.2214	–	0.658488

Table 4.4: Grid Convergence Index (GCI) results

Grid Pair	GCI
1-2	0.0008073
2-3	0.005546

As the grid becomes further refined, the increase in drag coefficient becomes progressively smaller. The order of convergence was $p = 2.85$, consistent with second-order spatial accuracy, and the finest-grid GCI was 0.08% (Table 4.4), indicating grid convergence. However, as the gimbal rings and payload are small relative to the full domain, the local accuracy may not scale exactly with the global drag-based GCI.

4.7 Sensitivity Study

A sensitivity study for further verification was performed by repeating the simulations for the long-term mean and 50-year recurrence flow conditions in addition to the 1-year case 3.1. Testing a wide range of speeds would be too computationally intensive. These runs used the original domain and a 1 m base mesh to reduce computational cost. Peak moments about both gimbal axes and the mean drag coefficient recorded are shown in Table 4.5.

Table 4.5: Key results for key flow conditions

	Max moment on outer gimbal ring axis [Nm]	**Max moment on inner gimbal ring axis [Nm]**	**Mean drag coefficient**
Long-term mean	0.5266	0.2337	1.179
1-year recurrence	0.1618	0.2160	1.085
50-year recurrence	0.2631	0.2781	1.096

Contrary to initial expectations, the largest outer-axis moment occurred under the long-term mean flow, which was more than twice that of the more extreme cases. This is likely due to reduced turbulence intensity at higher flow speeds. Faster flow passed over the top of the frame and tended to drag fluid out of it, whereas slower flow allowed stronger mixing and more uneven vortex interaction with the underside of the gimbals.

The inner-axis moment varied by up to 22.3%, and the maximum difference in drag coefficient was 8%. The reference velocity at the frame mid-height was input manually from the log-law profile, so some uncertainty is associated with these comparisons.

4.8 Results

The refined model, using the enlarged domain and finest grid, gave a maximum moment of 1.1851 Nm on the outer gimbal axis under long-term mean conditions. This was more than double the 0.5266 Nm obtained earlier from the smaller-domain sensitivity study. The peak moment acted inwards towards the frame centre and is taken as the actuator design load. The values were taken over a span of 10 wave periods after convergence, as shown in Figures 4.9 and 4.10. It can be seen that, while the moments about the inner gimbal's axis are smaller and more random, they are weighted to one side, suggesting some asymmetrical flow.

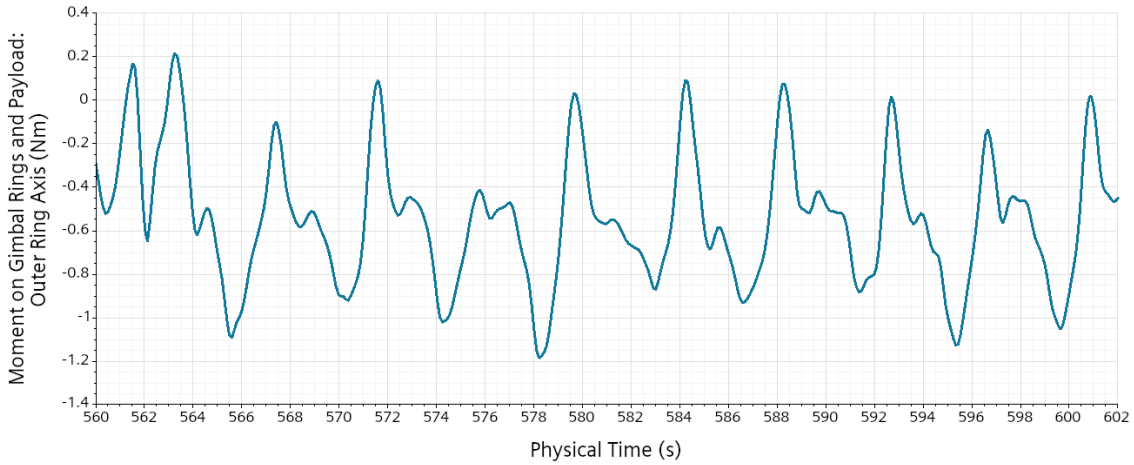


Figure 4.9: Moment produced on gimbals and payload - axis of outer gimbal ring

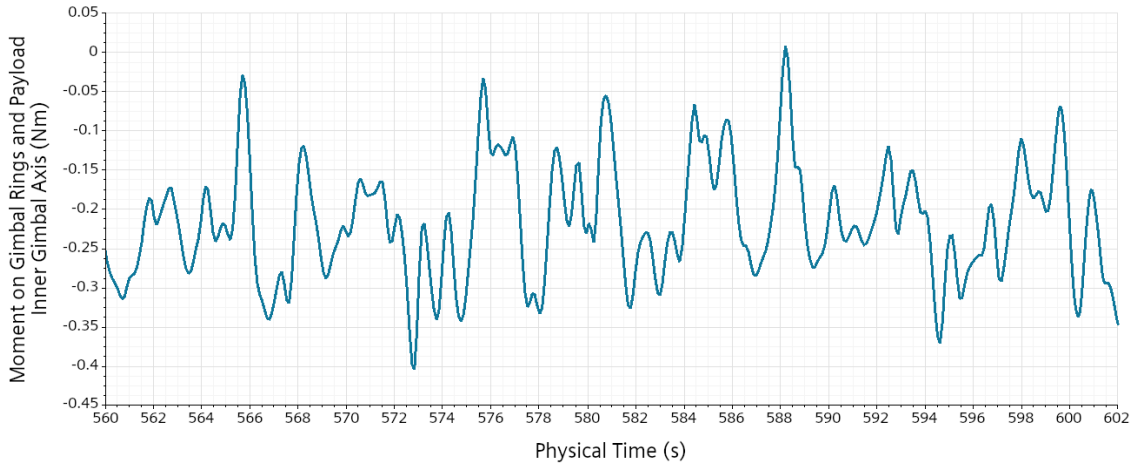
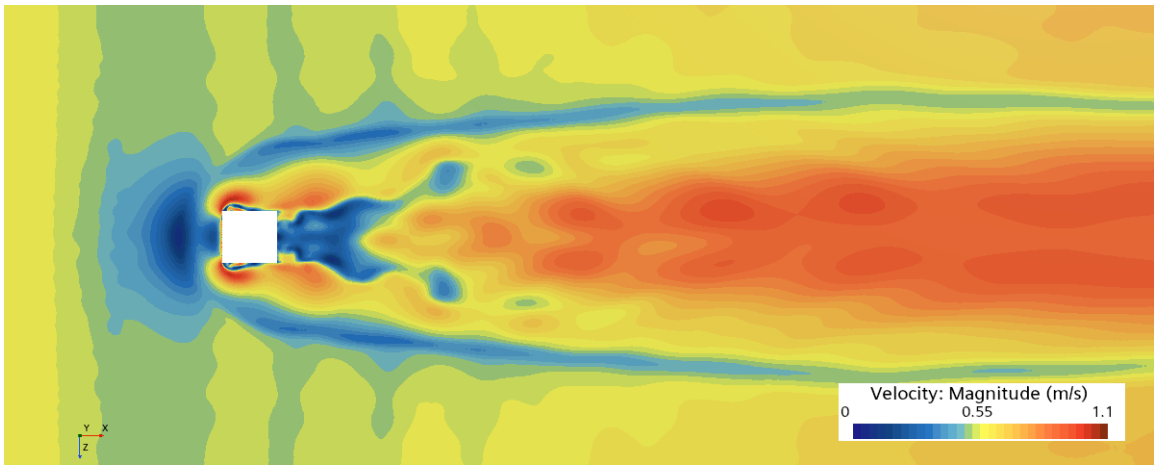


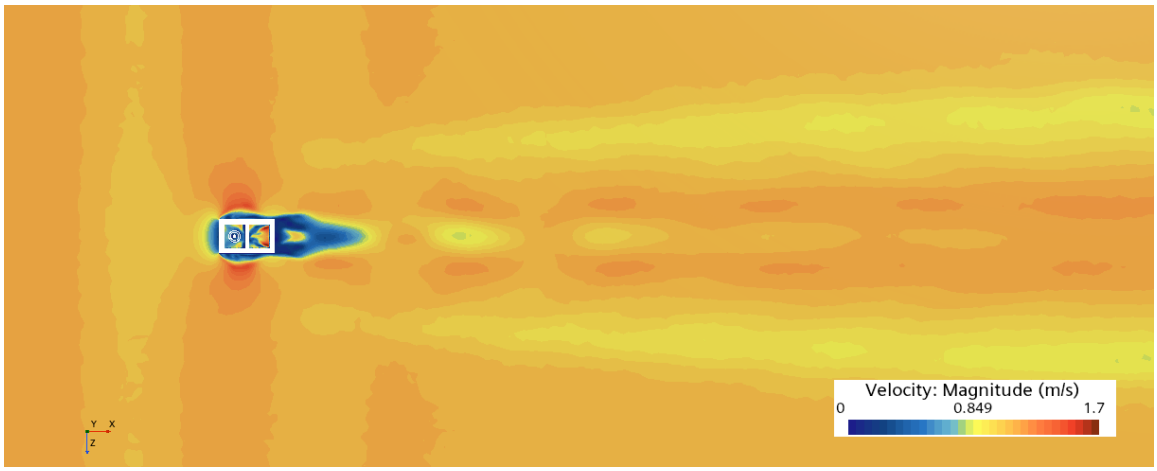
Figure 4.10: Moment produced on gimbals and payload - axis of inner gimbal ring

Figure 4.11 shows scalar velocity magnitude on two horizontal cross sections of the domain, the latter at the height of the gimbal rings. All plots in this section are from the same time step, and the colour bars are automatic. Flow visualisation showed that the external flow behaved like that around a bluff body [46], with:

- Stagnation ahead of the frame
- Acceleration around the front corners
- separation and vortex shedding
- A large wake downstream



(a) $z = 0.1$ m - velocity scalar



(b) $z = 0.75$ m - velocity scalar

Figure 4.11: Horizontal scalar velocity plots on final simulation. File: Full Model Simulation V6 Long Term Mean.sim

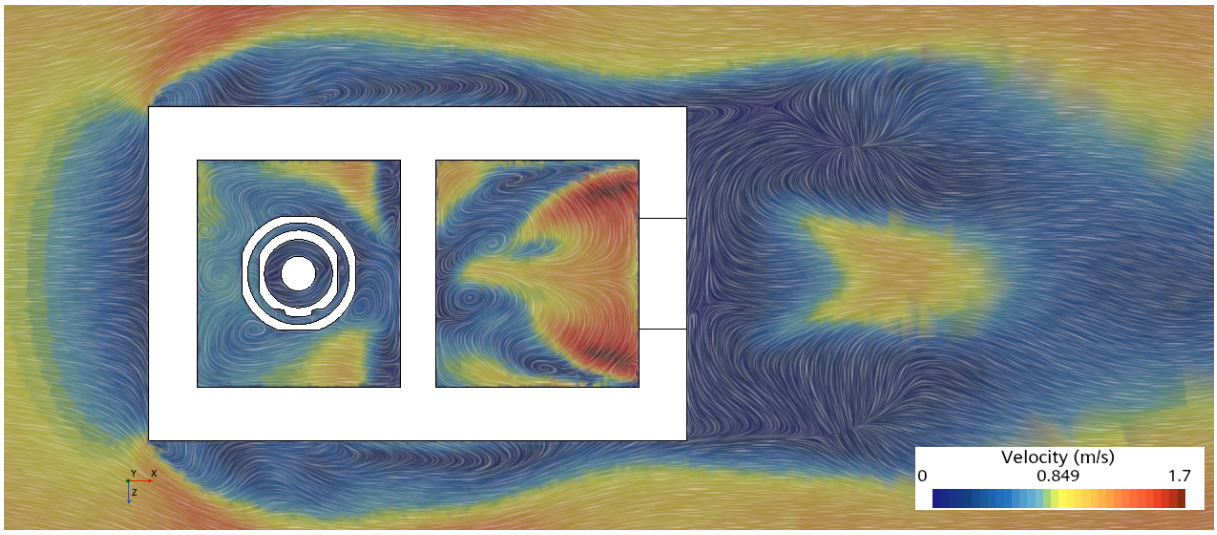
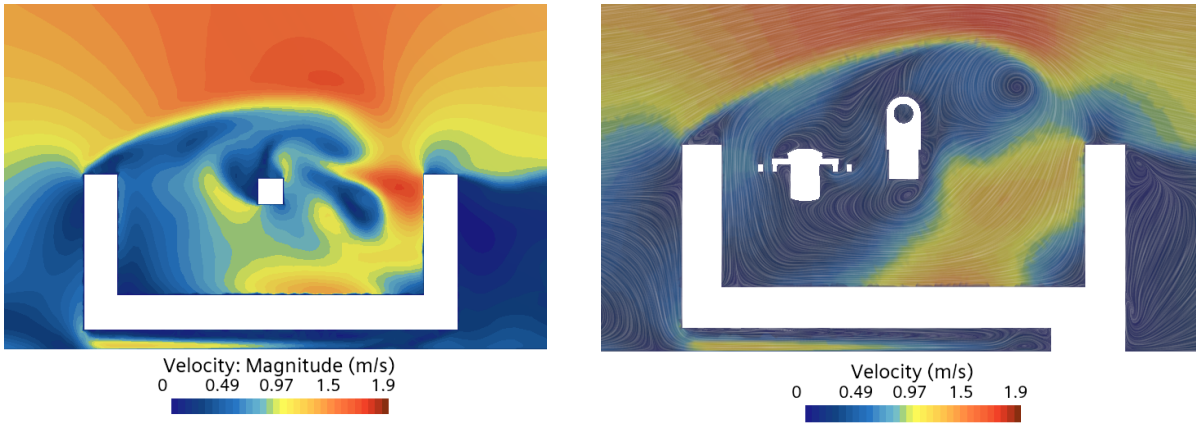


Figure 4.12: Horizontal vector velocity plot of frame on final simulation, $z = 0.75$ m. File: Full Model Simulation V6 Long Term Mean.sim

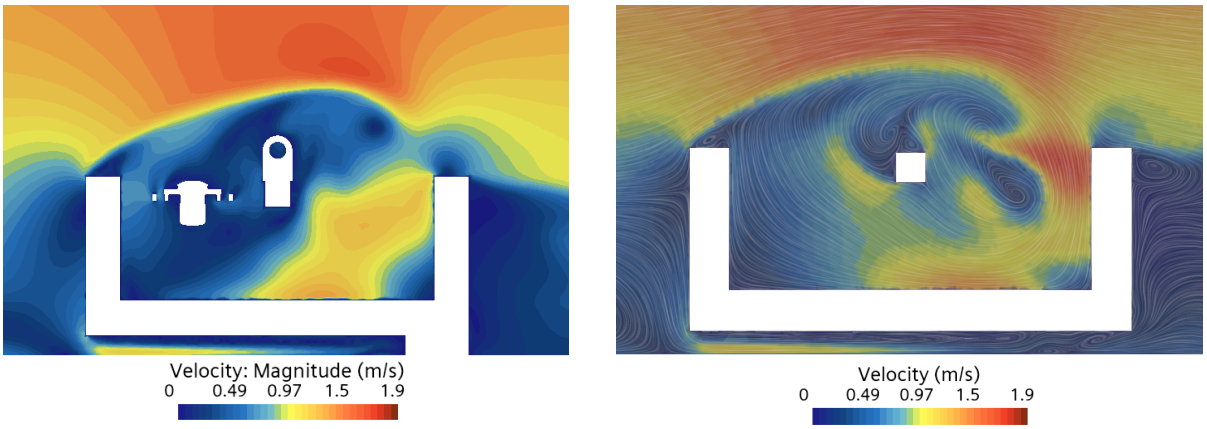
Within the frame, there were recirculating regions at the front and high-velocity zones near the rear corners (Figure 4.12). The critical flow inside the frame is best visualised with vertical cross-sections at the centreline (Figure 4.13) and offset by 0.28 metres (Figure 4.14) to capture the high velocity flow identified in Figure 4.12. The flow matches the hypothesis made in Section 3.1, and shows a maximum speed of approximately 1.7 m/s, compared with about 1 m/s at the gimbal rings. This indicated the need for a further simulation with the flow in the other direction.



(a) $y = 0.28$ m velocity scalar

(b) $y = 0$ m velocity vector

Figure 4.13: Vertical cross-section velocity plots on final simulation. File: Full Model Simulation V6 Long Term Mean.sim

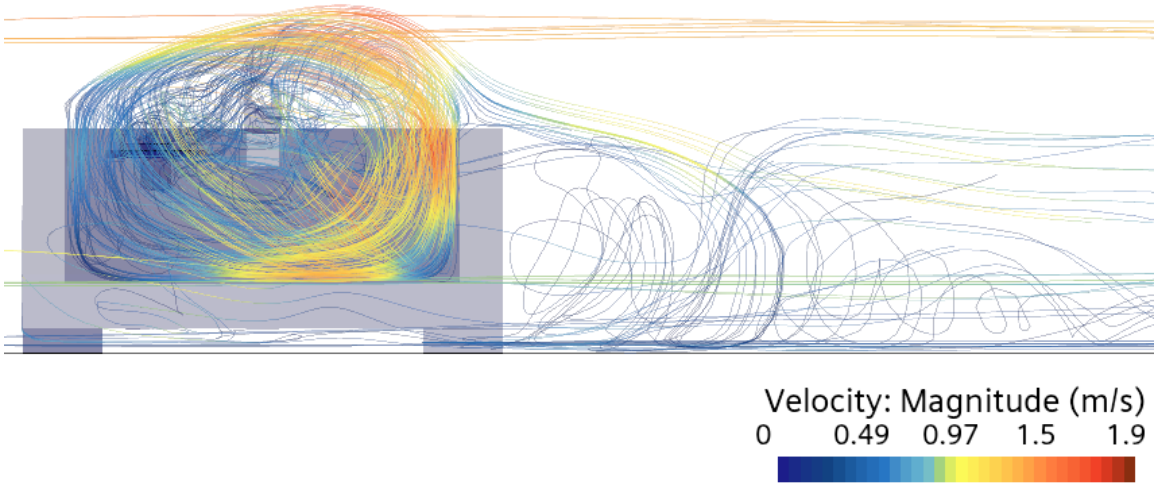


(a) $y = 0.28$ m velocity scalar

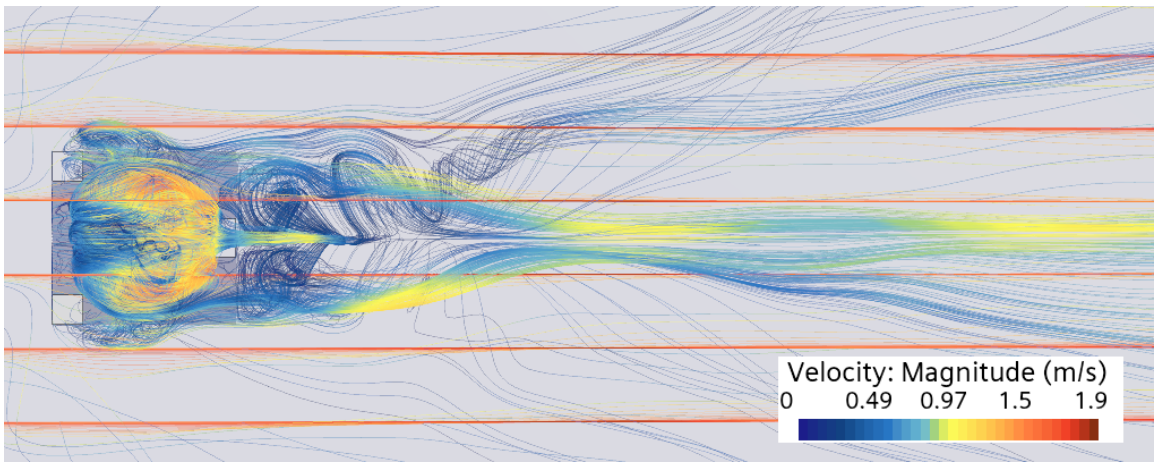
(b) $y = 0.28$ m velocity vector

Figure 4.14: Vertical cross-section velocity plots on final simulation - offset 0.28 metres. File: Full Model Simulation V6 Long Term Mean.sim

Figure 4.15 further illustrates the flow inside and around the frame using streamlines. The area of high velocity flow at the rear interior of the frame only occurs periodically for around 1 second at a time. A reverse-flow simulation, placing the payload and gimbal system effectively at the back of the frame, was attempted but had not been completed at the time of submission due to unresolved simulation instability.



(a) Cross-sectional view



(b) Top down view

Figure 4.15: Streamlines scalar scene in final simulation. File: Full Model Simulation V6 Long Term Mean.sim

Chapter 5

Housing Design

5.1 Actuator Selection

CFD results showed that the actuators must resist a peak torque of 1.185 Nm (Section 4.8), including a conservative safety factor to account for the model's limitations. Dr Sellar's team identified MyActuator products as being available at a reasonable cost [47]. The RH harmonic drive series was selected for further review because it includes a brake.

Brake holding torque is more important than rated or peak drive torque, as the actuator must hold position without movement. Key actuator data is summarised in Table 5.1 [47] [48] [49].

Table 5.1: MyActuator RH Series performance values

Actuator	RH-17	RH-20	RH-25	RH-32
Peak torque [Nm]	54	80	157	229
Rated torque [Nm]	35	50	108	150
Static torque of brake [Nm]	0.5	0.8	1.2	2
Actual static torque of brake [Nm]	50	80	120	200
Mass [kg]	1.28	1.75	2.74	4.74
Length [mm]	104	97.4	105.2	125.3
Max diameter [mm]	80	90	110	142
Min diameter [mm]	67	78	94.8	100
Price [£]	1,172.30	1,338.46	1,587.70	1,749.23

Although the user manual lists low brake torque values, the 100:1 reduction ratio means that the back-driving torque at the output shaft is reduced by a factor of 100 at the motor. The RH-17 brake value, therefore, corresponds to 50 Nm at the output shaft, giving an effective safety factor of 42, which is more than sufficient given the uncertainties in the CFD model and operating conditions. The RH-17 has the lowest mass, diameter (important for minimising material cost) and price. The output torque values are more than adequate for the movement required. Therefore, the selected actuator is the MyActuator RH-17, model EPS-RH-17-100-E-B-D.

5.2 Actuator Operation and Housing Design Considerations

5.2.1 Actuator Description

The RH-17 actuator and installation dimensions are shown in Figures 5.1 and 5.2 [50]. The front mounting plate is the rotating element and accepts an externally mounted output shaft, with eighteen M3 threaded holes for shaft attachment. The remainder of the actuator remains stationary relative to the housing and is mounted to it through 3.4 mm-diameter holes.



(a) Rear of actuator

(b) Front of actuator in CAD (downloaded from manufacturer's website)

Figure 5.1: RH-17 actuator

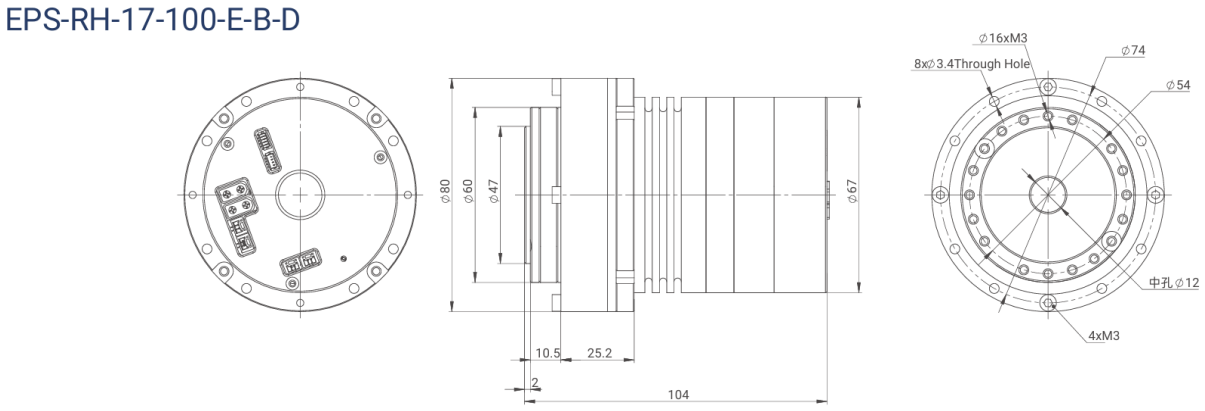


Figure 5.2: Installation drawing of RH-17 actuator

The actuator requires a sealed enclosure with two outputs:

- The output shaft to the gimbal rings.
- A rear electrical connection through a MacArtney 6-pin SubConn bulkhead connector (Figure 5.3). It has a 7/16" thread, and a 12.42 mm diameter O-ring that must be seated on a flat surface [51].



Figure 5.3: MacArtney 6-pin SubConn bulkhead connector

5.2.2 Design Strategy

The shaft is mounted first, followed by an end-cap over the front of the actuator. As the end-cap must connect rigidly to the actuator through the 3.4 mm holes and these holes must remain accessible for removal, the rear housing is designed as a separate part. The end-cap and rear housing are connected via flanges and at least one O-ring seal. The rear housing extends beyond the actuator to provide space for wiring and plug connections, and its rear face provides a flat mounting for the bulkhead connector.

5.3 Housing Design

The educational edition of SOLIDWORKS 2024 was used for CAD, which also has inbuilt finite element analysis capabilities for static structural analysis [52]. The software was selected for user familiarity, but alternatives such as Autodesk Fusion and SolidEdge offer the same functionality.

5.3.1 Output Shaft

The shaft comprises a circular base plate bolted to the actuator and a solid extruding shaft. Its critical requirement is concentricity with the actuator axis so that clearance to the end-cap bore remains constant during rotation.

The base plate outer diameter is 60 mm, matching the actuator's rotating face. A 2 mm raised section on the actuator, 47 mm in diameter, is avoided by a 48 mm diameter (Figure 5.1b), 2.5 mm deep recess on the rear of the shaft plate. Twenty 3.2 mm close-fit clearance through holes correspond to the effective twenty-hole pattern on the actuator face [53]. A central 12 mm flange shaft is retained for primary alignment with the actuator axis. The main shaft length is 53 mm after design iterations, and the original concept used an M10x1.5 threaded connection to the gimbal ring from a 20 mm-diameter shaft [54]. To assist the insertion of the threaded connection, a hexagon is cut into the shaft end, sizes for a 24 mm spanner.

As the part is axisymmetric, it is intended to be machined from solid metal by CNC turning, followed by milling of the rear recess and drilling of the bolt holes. External chamfers are included to deburr sharp edges.

Sealing

As discussed in Section 2.9, lip seals are the preferred option, followed by O-rings. The key requirements are seawater resistance and the ability to withstand 11.07 bar with a safety margin. No standard catalogue Trelleborg lip seal meets both: HP20 is the only pressure-capable seal family, but it is not listed as seawater compatible [55]. SKF also states that above 50 psi (3.4 bar), special-order PTFE seals are required instead of catalogue lip seals [56]. Trelleborg also specified that the mating surface roughness be no greater than Ra 0.5 µm and with no shaft misalignment greater than 0.1 mm.

Parker lists TDN3, NSC4, and NTC4 lip seals as suitable up to 13.7 bar, with FKM often used for high-temperature friction under pressure [57]. As with Trelleborg and SKF, a special order is required, even though the sizes range from 5 to 100 mm.

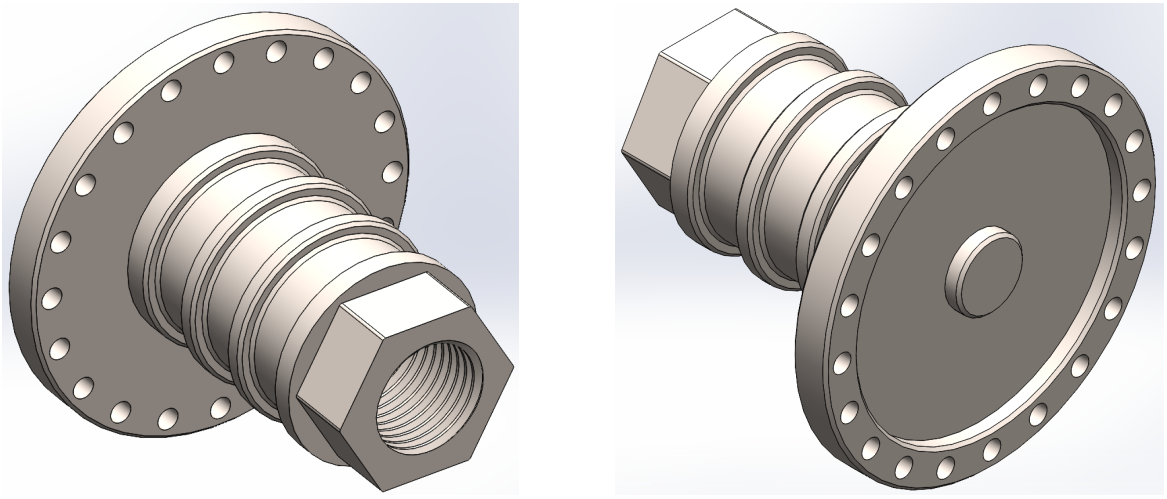
Standard O-rings are a suitable alternative because shaft motion is non-continuous and the duty cycle is low. The Parker O-ring handbook states that dynamic piston O-rings with 0.4 mm diametrical clearance can withstand 38 bar before failure, experienced at 368 metres depth, provided back-up rings are used [58]. Seal pressure-assisted by external seawater pressure.

A male groove on the shaft is used because it is simpler to machine than an internal undercut in the end-cap shaft bore. Based on Parker guidance and saltwater compatibility, compound E0540-80 EPDM (ethylene propylene rubber) was selected. Considering the 20 mm shaft, Parker seal 2-115 was selected, with a groove diameter of 17.64 mm and a mating diameter of 21.71 mm, giving 0.855 mm radial clearance to the bore.

The concept shaft includes three grooves to allow future testing of different O-ring and back-up ring arrangements. The corresponding Parker back-up ring is 8-215, N0300-90. Lubrication with Parker O-Lube would reduce friction and installation damage. Bearings were not included because the calculated shaft deflection was very small (Section 5.3.1) and remained within the O-ring compression range. The proposed shaft is shown in Figure 5.4. Chamfers are added to internal corners to reduce stress concentrations. For a specialist lip seal, these would be installed on the end-cap bore, against a plain shaft.

Material Selection

A metal shaft was required due to tight tolerances, strength requirements, lower thermal expansion, and better creep and fatigue performance compared to polymers.



(a) Front **(b)** Rear, showing cut-out

Figure 5.4: Output shaft

Copper beryllium has excellent anti-biofouling and mechanical properties, but it is carcinogenic, adding complexity and cost to manufacturing [59] [60]. It is also expensive, with a 1-foot (0.3048 m), 2 3/4" diameter (69.85 mm) bar costing £1,335 [61]. Comparatively, a half metre, 60 mm diameter bar of stainless steel grade 316 costs £145.97, and for the same quantity of titanium grade 5, £420.69 [62] [63]. As titanium is more expensive to buy and machine, stainless steel is preferred.

Finite Element Analysis

It is necessary to verify that the geometrical design and material choices are sufficiently robust. To ensure component resilience, a safety factor of 2 is targeted under maximum loads. The shaft was subjected to the peak actuator torque of 54 Nm, with the mounting face fixed. A remote mass representing half the combined payload and gimbal ring mass was also applied. Assuming a total in-water mass of 15.8 kg, twice the weight of the Origin 600, the load per shaft was 77.5 N acting 200 mm from the shaft end. Pressure of 11.07 bar is exerted.

Initial simulations gave a safety factor of 5.2 for titanium but only 1.2 for stainless steel 316. Increasing the shaft diameter to 30 mm with an M16 bolt hole improved the stainless steel safety factor to 2.72. After updating the seal to Parker 2-214 with back-up ring 8-214, the final safety factor was 2.63 (Figure 5.5) [58]. Maximum deflection was just 0.023 mm (Figure 5.6), and the highest stress occurred at the internal corner between the back O-ring groove and the chamfer. An M16 threaded connection was required for sufficient load distribution.

As the starting stock size would be similar for both materials, and stainless steel is non-magnetic, stainless steel 316 was selected for the final design.

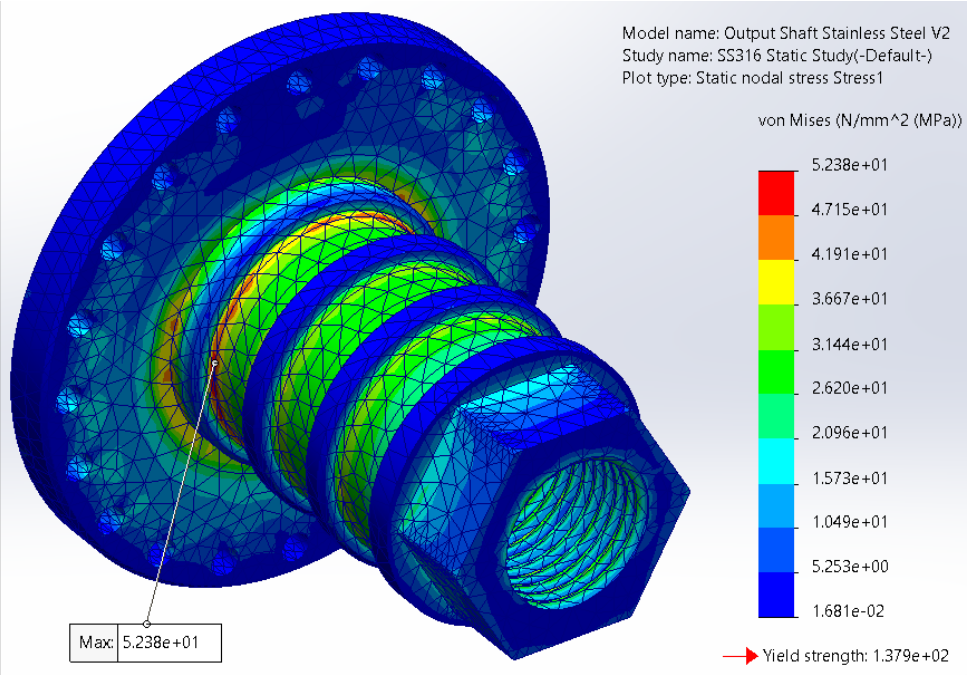


Figure 5.5: Output shaft FEA: Von Mises stresses

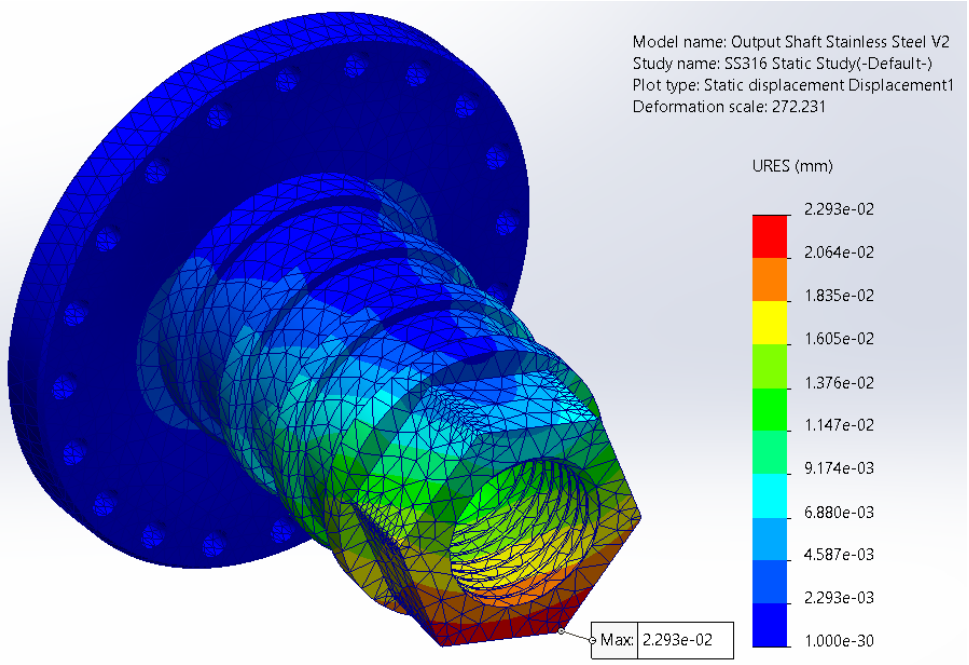


Figure 5.6: Output shaft FEA: displacement

5.3.2 End-cap

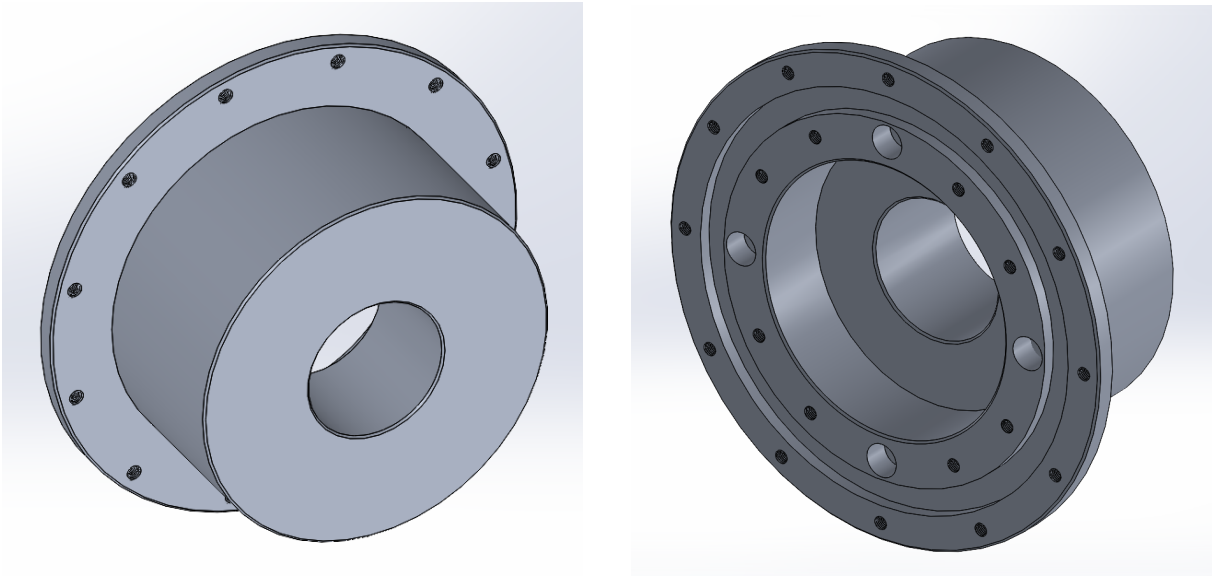
The end-cap interfaces with the actuator, the output shaft, and the rear housing. Its most critical function is maintaining a sealed, accurately aligned bore for the rotating shaft, requiring tight tolerances.

Internal clearances are designed to maintain a 1 mm spacing to rotating components, except at the shaft bore, where radial clearance is 0.82 mm to suit the O-ring seals. The actuator mounting holes are 3.4 mm clearance holes for M3 bolts. The corresponding holes on the end-cap are threaded, but are not through holes, so are contained within the housing.

The flange joining the end-cap to the rear housing is extended outwards rather than stepping over the actuator, so that the mounting face controlling the shaft bore can be machined accurately. Twelve threaded holes are used on the flange to provide uniform compression of the housing seal without requiring nuts.

Sealing

The joint between the end-cap and rear housing uses a static flange O-ring. For diameters above 80 mm, Parker recommends a 3.53 mm section with a groove depth of 2.90 mm. The groove is located on the end-cap, as the rear housing will be made of a material with poorer dimensional accuracy and stiffness (Section 5.3.3). The selected seal is Parker 2-236, in the same E0540-80 EPDM compound used for the shaft seals [58]. Figure 5.7 shows the designed end-cap.



(a) Front **(b)** Rear

Figure 5.7: End-cap model in CAD

Finite Element Analysis and Material Selection

The end-cap contains an air-filled cavity, so 11.07 bar external pressure was applied to all external faces, including the rear flange. The actuator mounting surface was fixed. No torque or downward force is exerted on this component.

Stainless steel 316 gave a safety factor of 5.9. The maximum stress occurred at the internal corner of the O-ring groove beside the M3 bolt-head clearance region (Figure 5.8), and the maximum displacement was 0.005 mm at the flange extremity (Figure 5.9). Note that deformation is exaggerated in all FEA figures.

POM-C acetal copolymer also appeared feasible, with a safety factor of 2.5 and maximum displacement of 0.36 mm, and no displacement at the bore. However, stainless steel was selected for its higher geometrical stability and lower surface roughness, which would reduce O-ring wear [64]. Acetal would be cheaper at £91.87 for a half metre of 110 mm diameter [30].

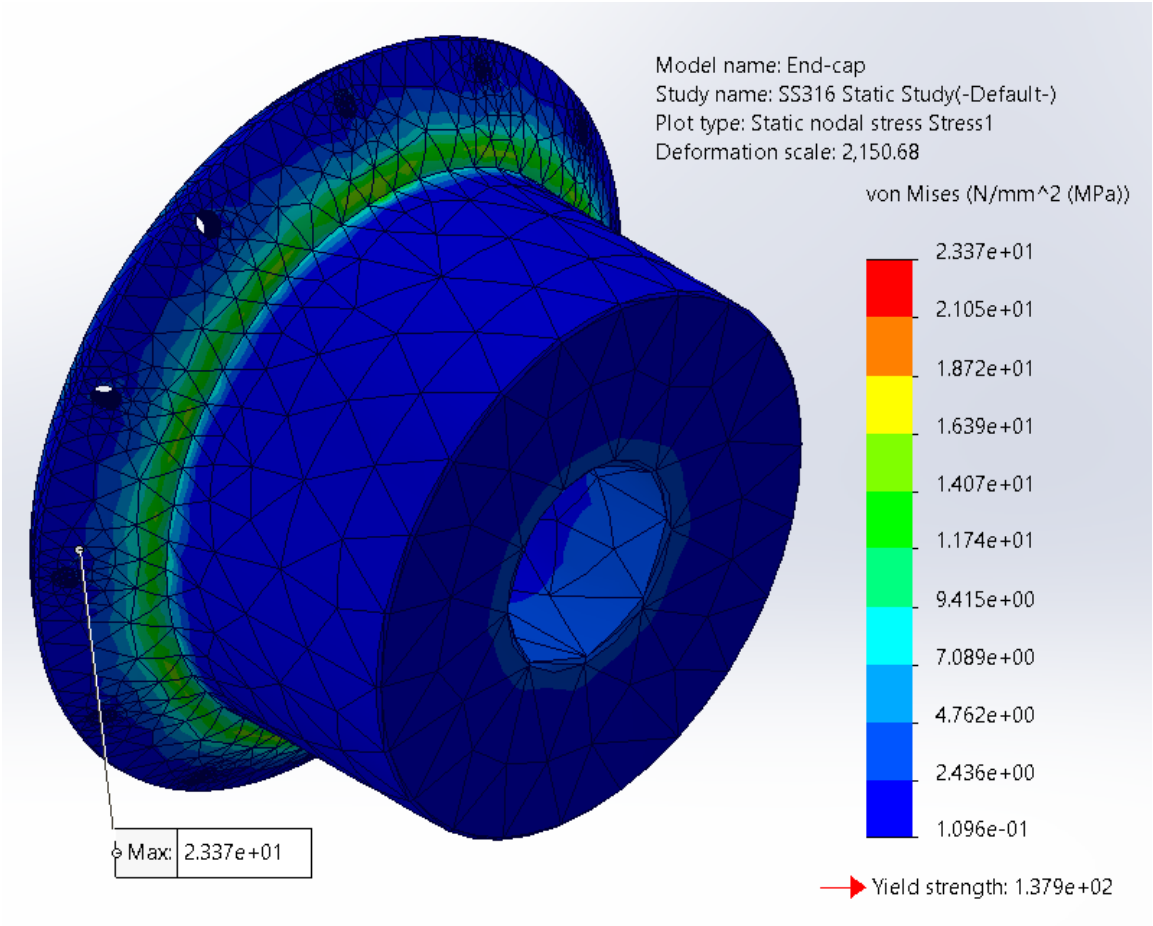


Figure 5.8: End-cap FEA: Von Mises stresses

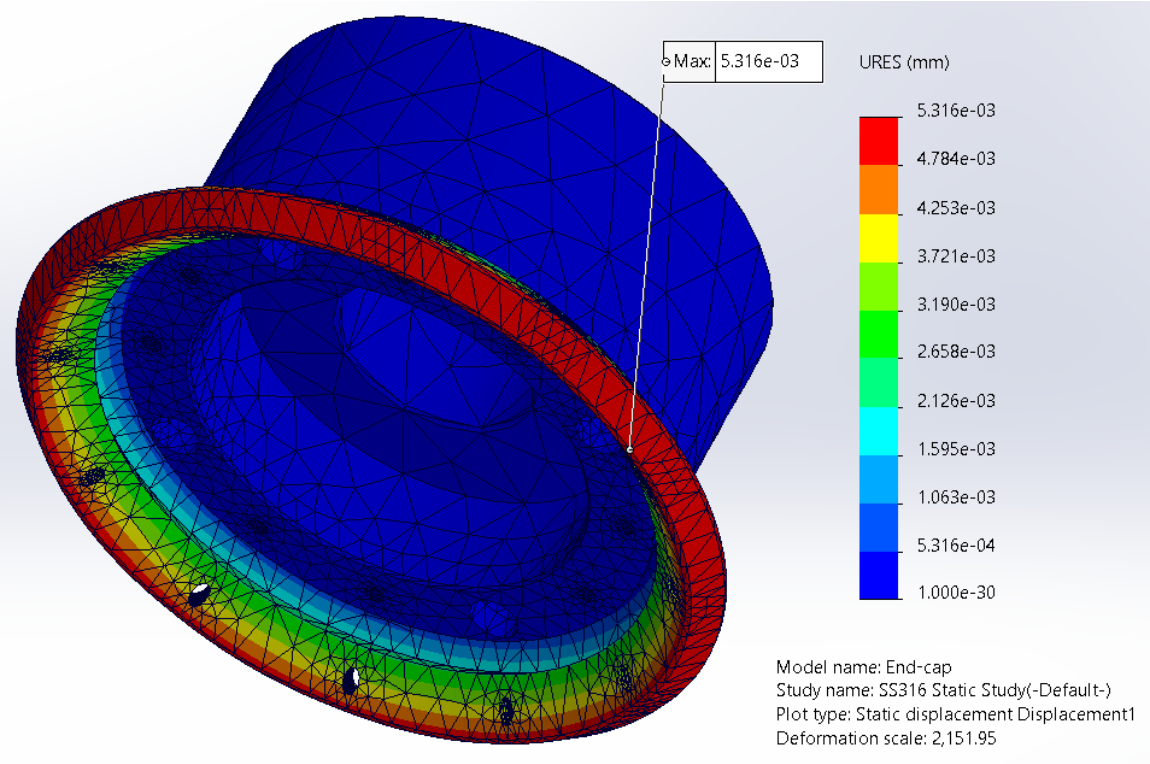


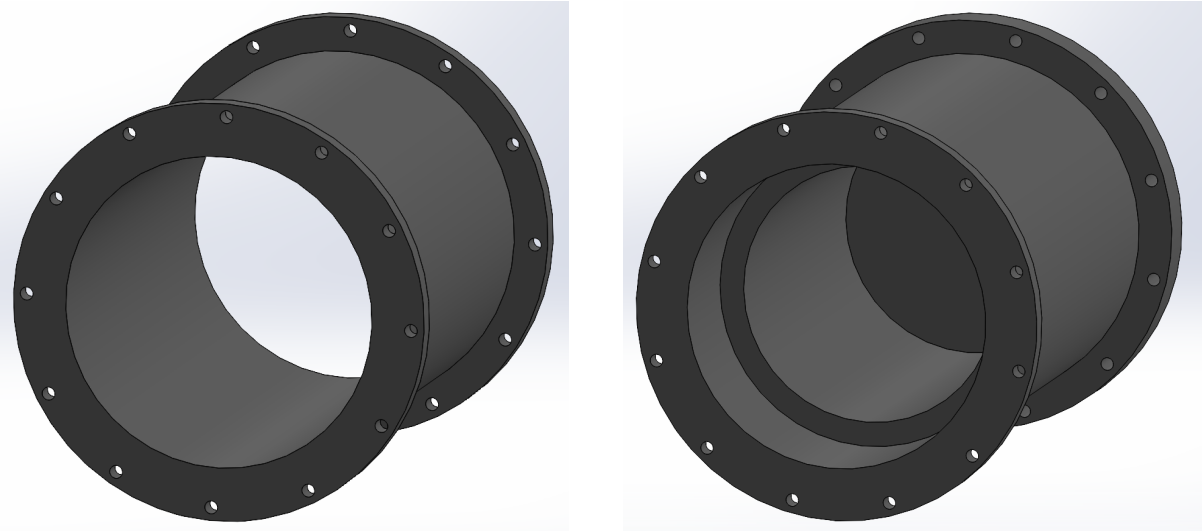
Figure 5.9: End-cap FEA: Displacement

5.3.3 Rear Housing

The rear housing encloses the actuator's rear and attaches to the rear face of the end-cap. Because no tight internal tolerances are required, polymer materials were considered acceptable.
Two design options were assessed:

- a constant-diameter tube with open ends and flanges, with a separate back plate (Figure 5.10a).
- a housing with a reduced internal diameter at the rear and a solid back face with a threaded hole for a connector (Figure 5.10b).

The first option has direct access to the actuator-to-end-cap bolts, allowing the end-cap and rear housing to be removed together, but it would require an additional seal and back plate. The second option avoids this extra seal and potential failure point and increases stiffness through a thicker rear section, so it was selected. A disadvantage is that a solid bar must be used for manufacturing instead of a cheaper pipe. Clearance behind the actuator for cabling is 15 mm.



(a) Design choice 1 - constant inner diameter **(b)** Design choice 2 - varied inner diameter with back

Figure 5.10: Rear housing design options

Finite Element Analysis and Material Selection

11.07 bar pressure was applied to the external surfaces, the front flange was fixed, and a 54 Nm torque was applied to the rear flange, as if all other components were perfectly rigid. POM-C acetal copolymer was used for the analysis.

Peak stress occurred at the junction between the bulkhead connector thread and the outer surface (Figures 5.11 and 5.12). The local safety factor there was 2.6, rising to 3.3 in the surrounding material. Maximum displacement was 0.28 mm at the same location (Figure 5.13). The stress concentration may be conservative because the rigid connector itself was not modelled, but the results were sufficient to justify the use of POM-C acetal.

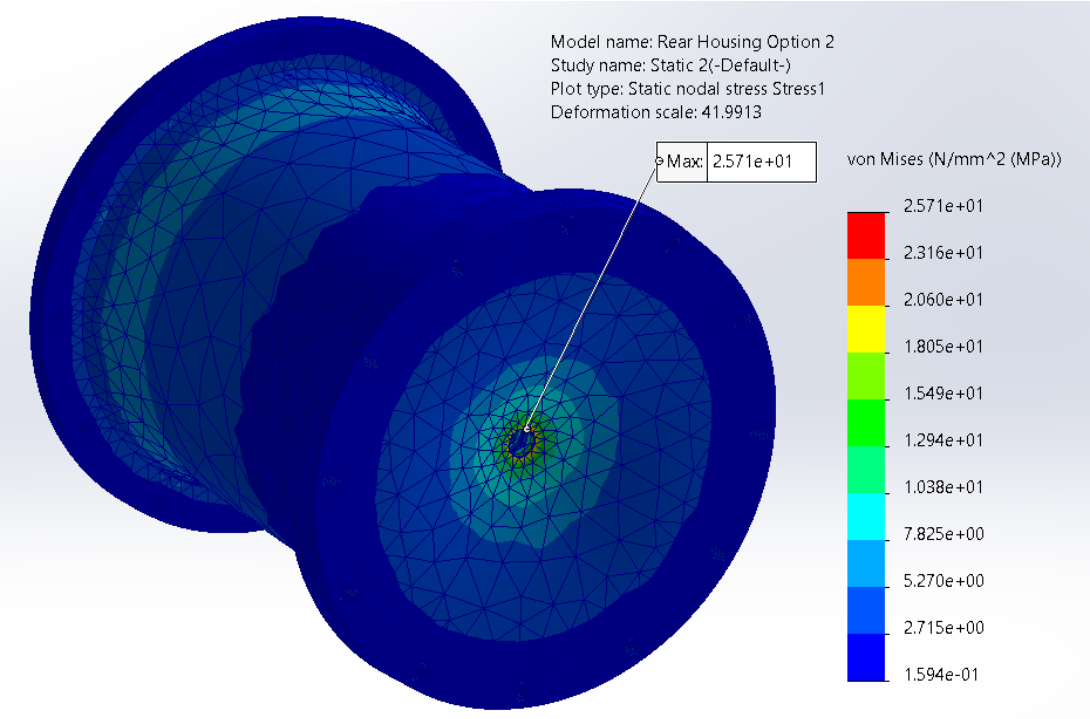


Figure 5.11: Rear housing FEA: Von Mises stresses

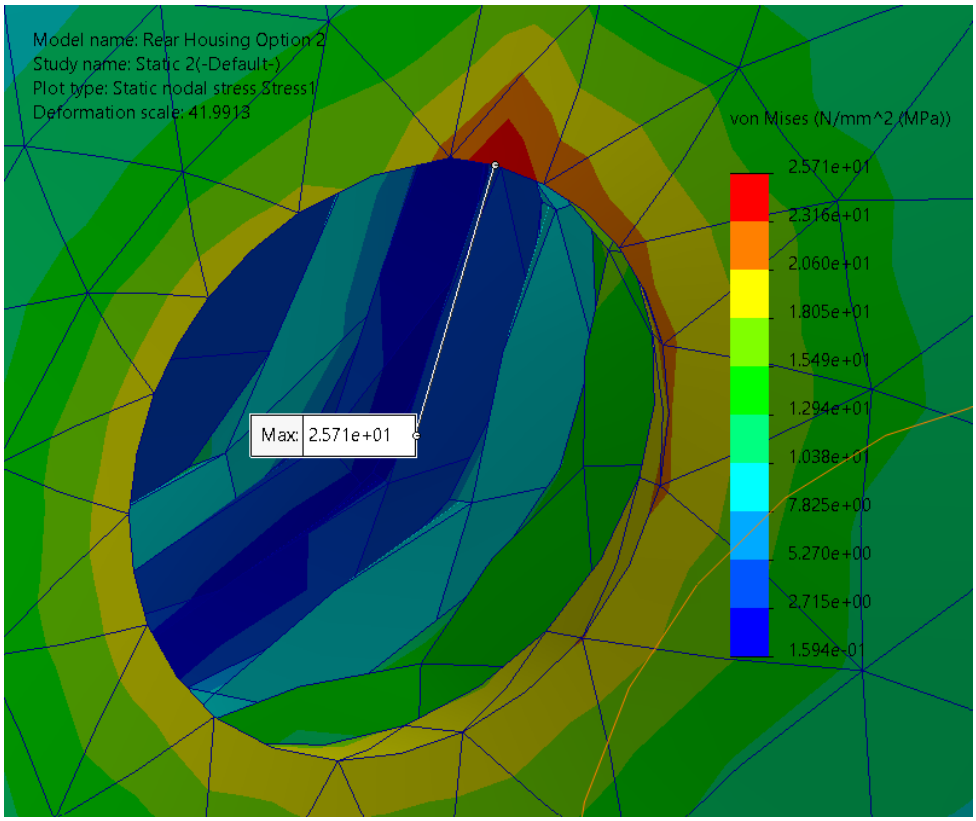


Figure 5.12: Rear housing FEA: localised stresses at the bulkhead connection

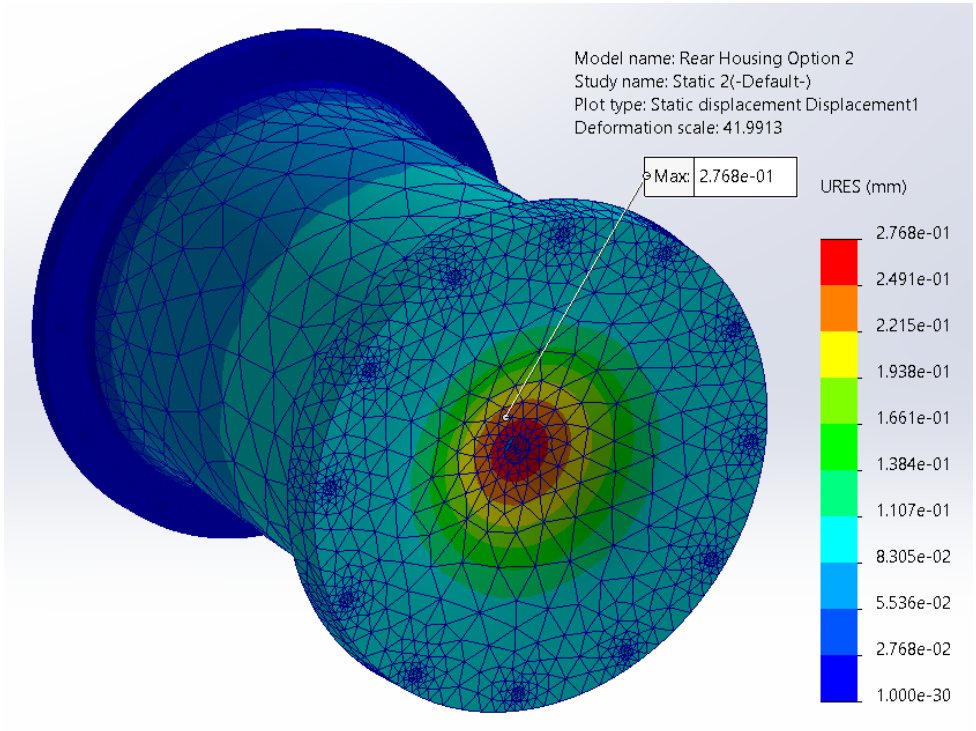
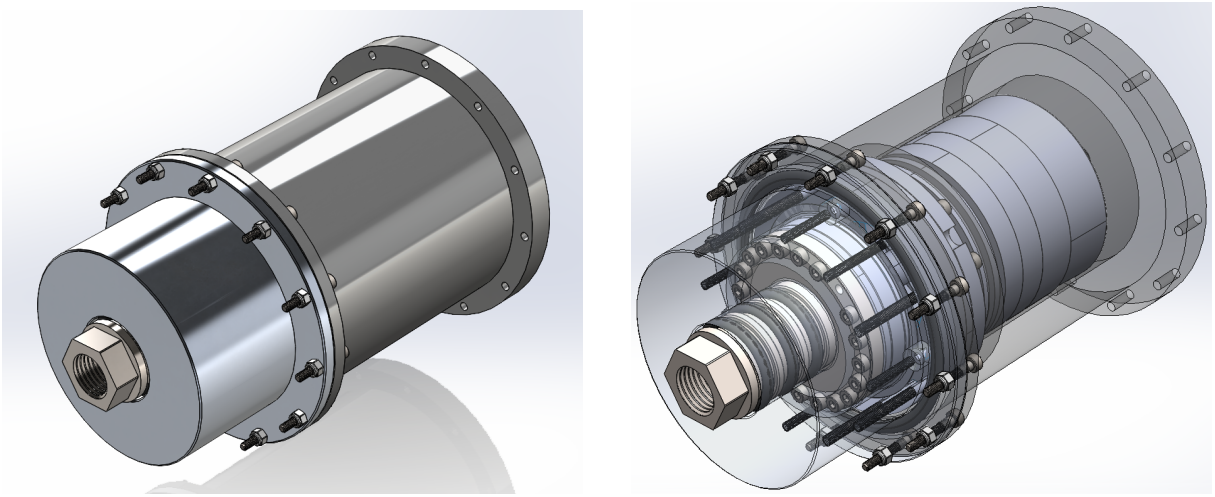


Figure 5.13: Rear housing FEA: displacement

5.3.4 Assembly

The assembly, and an exploded view including fasteners (Section 5.4.1) are shown by Figures 5.14 and 5.15. The total mass is 3.604 kg.



(a) Solid **(b)** Transparent end-cap and rear housing

Figure 5.14: Actuator components assembled

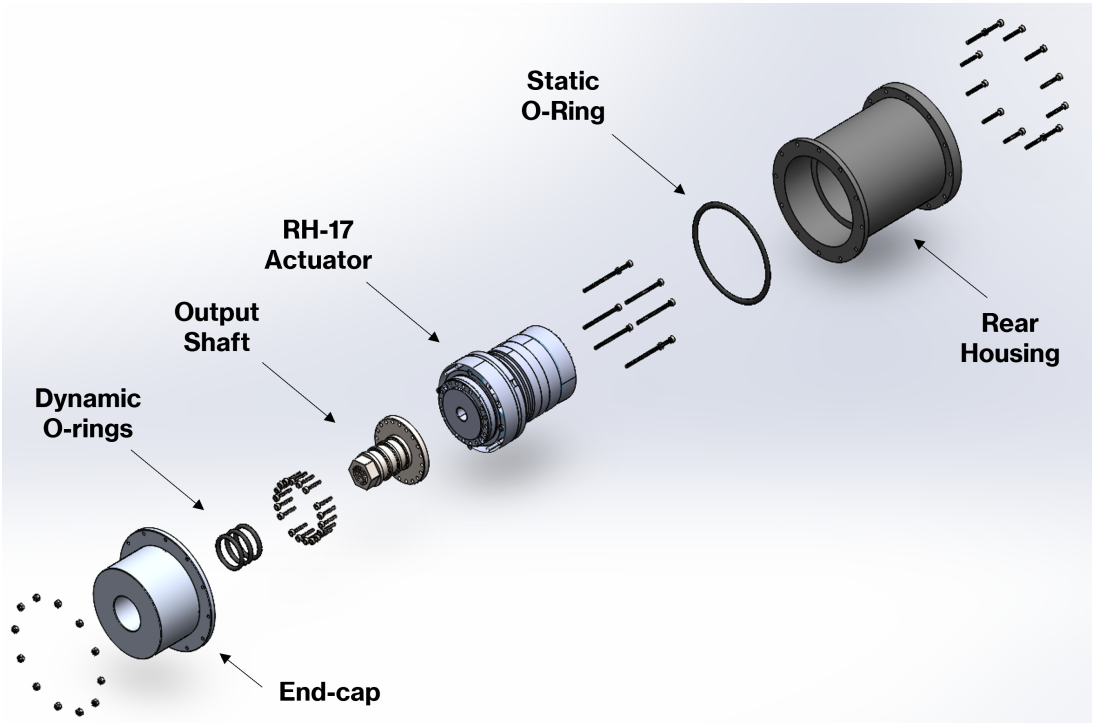


Figure 5.15: Exploded view of actuator assembly

5.3.5 Connection to Frame and Gimbal Rings

Connection to Frame

Only one actuator is required per gimbal ring, as the actuator torque and brake capacity greatly exceed the design requirement. The actuator driving the outer ring is mounted between the frame and the ring.

The frame connection will be via a stainless steel plate (Figure 5.17a) mounted to the rear housing flange (Figure 5.16). FEA indicated that an 8 mm-thick stainless steel plate provides a safety factor of 2, and this part is intended to be laser-cut (Figure 5.17b). Two M16 bolts either side of the bracket can join to the frame, length adjustable using Nyloc nuts, used throughout to reduce loosening under vibration and cyclic load.

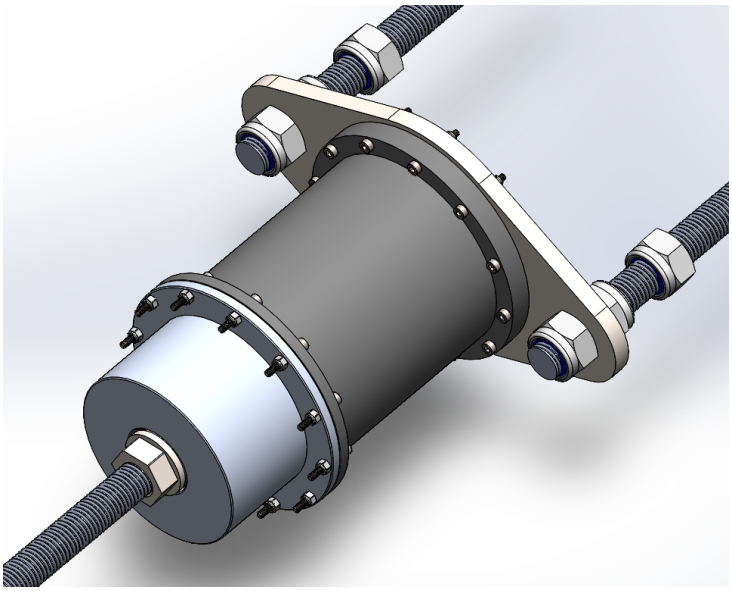
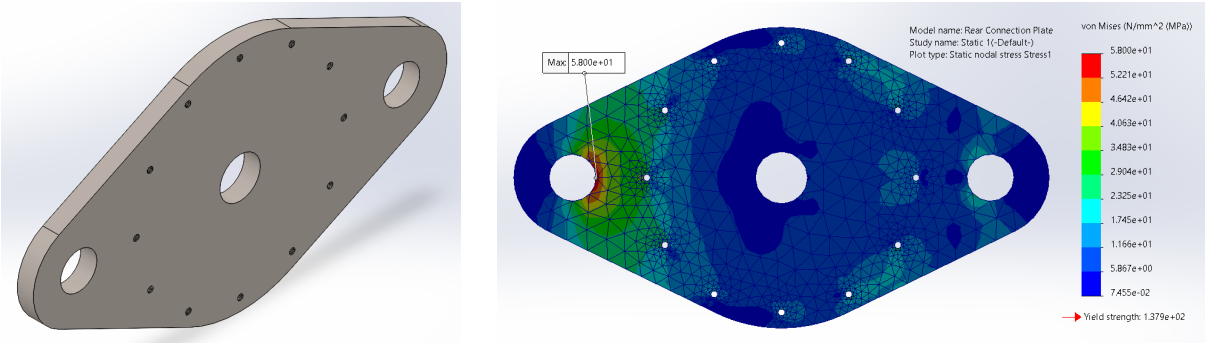


Figure 5.16: Actuator assembly with back plate and threaded rods to pass through frame



(a) 8 mm thick stainless steel 316 **(b)** FEA Von Mises stresses

Figure 5.17: Rear connecting plate

Connection to Outer Gimbal Ring

The actuator driving the inner gimbal ring is mounted to the outer ring through the housing flange rather than from within the inner ring, to keep the assembly compact. An unthreaded middle connecting plates (Figure 5.19a) is mounted to the flange (Figure 5.18). Redesign of the gimbal rings to suit this connection is outside the scope of this work.

An 8 mm thick stainless steel middle bracket achieves a safety factor of 2.4 (Figure 5.19b). The maximum stress occurs locally at a bolt hole, and the maximum deflection is 0.055 mm.

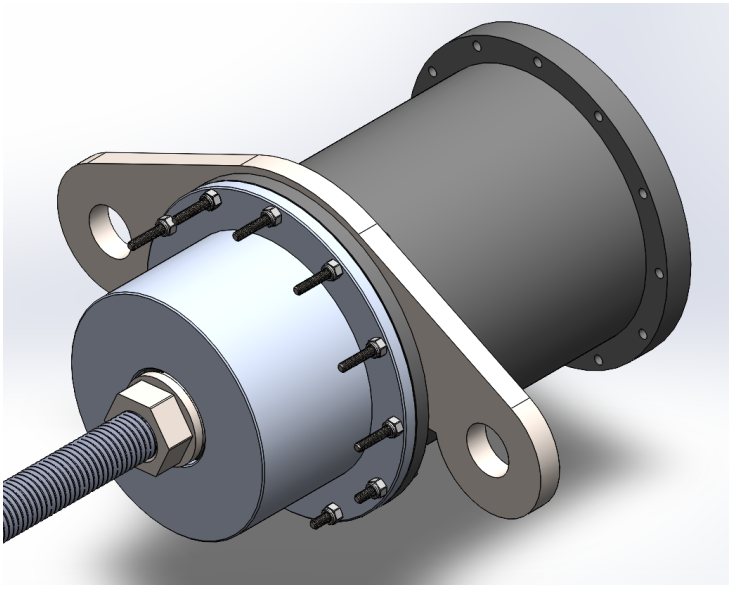
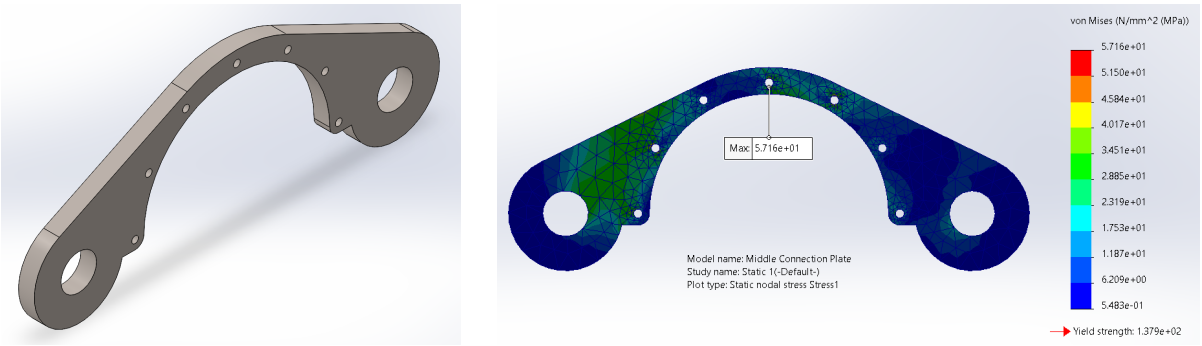


Figure 5.18: Actuator assembly with middle plates for attachment to outer gimbal ring



(a) 8 mm thick stainless steel 316 **(b)** FEA Von Mises stresses

Figure 5.19: Middle connecting plate - inner gimbal

5.4 Actuator Assembly

5.4.1 Fasteners

Socket cap screws were selected due to limited tooling access inside the housing. External joints use threaded components, but Nyloc nuts are recommended to resist loosening under cyclic loads and vibrations, which can cause seawater ingress. Alternatives include spring washers, split washers, Nord-Locks, or non-permanent threadlockers. The screws and nuts required for one complete assembly of a frame-mounted and gimbal-ring-mounted actuator are given in Table 5.2. All fasteners are marine-grade stainless steel.

Table 5.2: Fasteners required for full assembly - minimum lengths

Fastener	Quantity	Connection
M3x16mm	36	Shaft to actuator connection
M3x40mm	24	Actuator to end-cap connection
M3x20mm	17	External rear housing to end-cap connection (outer and inner actuator)
M3x25mm	12	External rear housing to rear bracket connection (outer actuator)
M3x35mm	7	External rear housing to end-cap and middle gimbal ring connection brackets (inner actuator)
M3 Nyloc	36	All external bolts
M16 Nyloc	12	Connection from back plate to frame, and to gimbal rings

5.5 Tolerances

In general, dimensional tolerances are ± 0.05 mm. Tighter tolerances would increase manufacturing costs and are applied only where functionally necessary. The tolerances described below are shown on the individual component drawings in Appendix D, while an example drawing for the output shaft is shown by Figure 5.20.

5.5.1 Output Shaft

Critical dimensions for tight tolerances are the flange shaft, which locates the shaft concentrically on the actuator, and the O-ring groove geometry, which minimises misalignment and wear.

Defining the main shaft axis as datum A, the following tolerances are applied:

- Total runout of 0.02 mm is applied to the flange shaft outer diameter and O-ring grooves.
- Shaft diameters have a general tolerance of 0.02 mm, and positional tolerance 0.1 mm.
- O-ring groove surface finish is specified as maximum Ra 0.5 µm, critical for sealing.
- the rotating face has a runout tolerance of 0.02 mm relative to datum A to minimise shaft angular misalignment.

The actuator central hole is stated as ±0.2 mm, so the locating flange shaft is sized at 11.8 mm. A surface finish of 0.5 µm is possible with turning, Ra 1.6-3.2 µm is typical for as-machined finishes [64]. An extremely high surface finish is not required, as there is no continuous rotation.

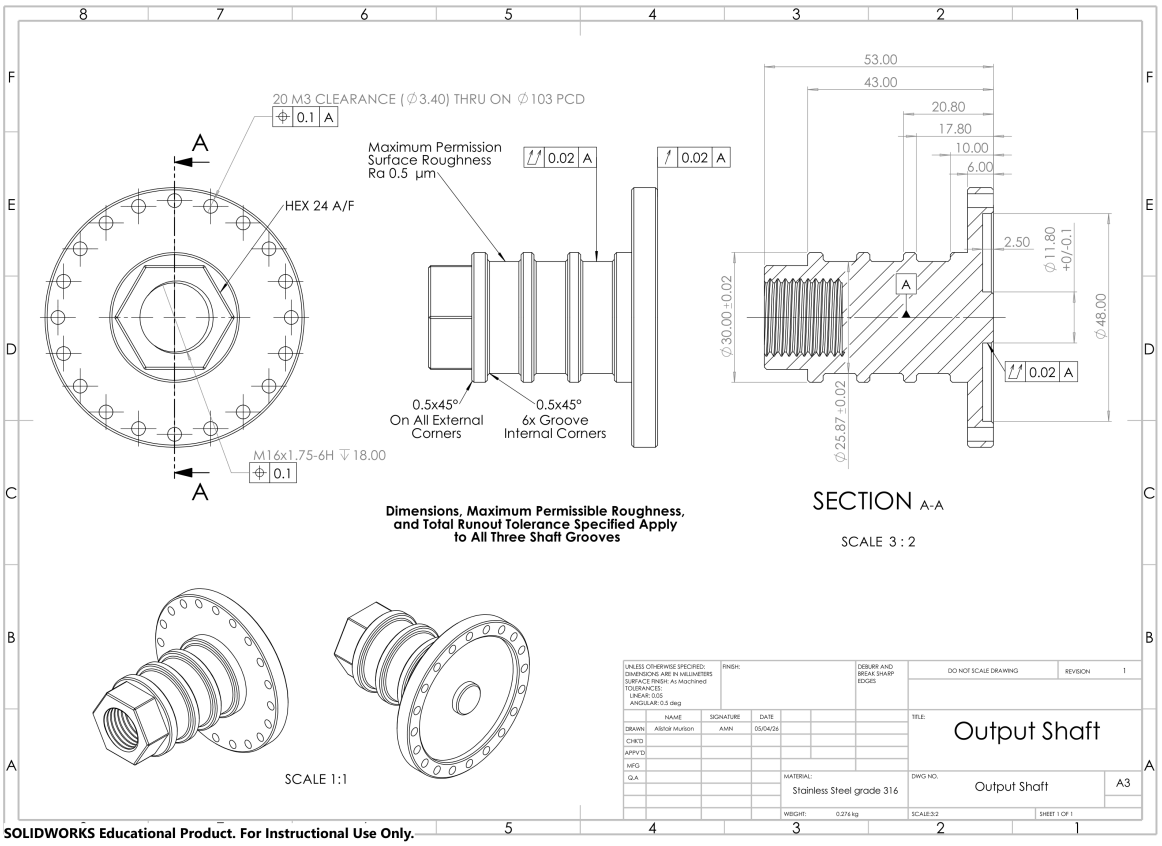


Figure 5.20: Output shaft manufacturing drawing

5.5.2 End-cap

The critical requirement is alignment of the shaft bore with the actuator axis after assembly. The key controls are the position of the central bore and the bolt hole pattern beneath it.

The datum system is based on the features used to locate it during assembly:

- Mounting face = datum A
- Bolt-hole pattern = datum B
- One bolt hole = datum C

The shaft bore is assigned a positional tolerance of 0.05 mm relative to A, B, and C, limiting combined uncertainty with the shaft to within the O-ring manufacturing tolerance of ±0.09 mm. The bore surface finish is maximum Ra 0.5 µm as per the shaft.

The bolt-hole pattern is controlled with a position tolerance of 0.10 mm, as the actuator through holes are 3.4 mm in diameter. Due to potential misalignment, a fitting tool would provide more reliable concentric alignment, with the bolt holes primarily clamping the part in place.

5.5.3 Rear Housing and connector plates

No specific dimensional tolerances are required for the rear housing or connector plates. The static flange O-ring between the rear housing and end-cap accounts for small variations in flatness.

5.6 Costs

5.6.1 Bill of Materials

Table 5.3 summarises the quantities and prices, including VAT, of off-the-shelf items and raw materials required. The volume of raw material is that required to manufacture the required pieces, plus a marginal spare for cutting. Weblinks are provided for convenience in ordering. Shipping is excluded. Prices for unchanged components from the previous design are assumed to be covered elsewhere. Material prices would reduce if multiple sets were manufactured. The total price for an actuator pair is £3,341.74, £5,778.26 (or 63.4%) cheaper than a pair of the previously tested Arctic Rays actuators.

To reduce the number of bolt types, the 20 mm, 25 mm, and 35 mm bolts are replaced by 40 mm bolts, increasing the number of M3x40 mm bolts to 60 with minimal effect on overall cost.

Table 5.3: Bill of Materials. Prices correct as of 29th March 2026

Item	Quantity	Unit Cost	Cost	Source
MyActuator EPS-RH-17-100-E-B-D	2	£1172.30	£2,344.60	[47]
Parker Hannifin E0540-80 2-214	6	~ £15	~ £90	[65]
Parker Hannifin E0540-80 2-236	12	~ £15	~ £180	[65]
Parker Hannifin E0540-80 8-214	2	~ £15	~ £30	[65]
Parker Hannifin E0540-80 8-236	4	~ £15	~ £60	[65]
M3x16mm bolt	36		£7.20 (50 pack)	[66]
M3x40mm bolt	60		£26.40 (100 pack)	[67]
M3 Nyloc nut	36		£5.40 (50 pack)	[68]
M16 Nyloc nut	12		£14.40 (12 pack)	[69]
M16 threaded rod, 2 m	1		£49.72	[70]
110 mm diameter, 250 mm length, POM-C acetal rod	1		£48.23	[71]
110 mm diameter, 150 mm length, 316 stainless steel bar	1		~ £340	[62]
80 mm diameter, 150mm length, 316 stainless steel bar	1		£107.88	[72]
300x225 mm, 8 mm thick plate	1		£37.91	[73]
Total			**£3,341.74**	

5.6.2 Labour Costs

Manufacturing costs depend strongly on whether parts are produced internally by the School of Engineering or outsourced. The required processes are summarised in Table 5.4.

Two instant-quote suppliers, Xometry and Protolabs Network, were used to obtain indicative CNC machining costs, outputting vastly different estimates [74] [75]. These quotes include material but not inspection, and should be treated as approximate until reviewed by an engineer against the final drawings. Xometry could not provide an instant price for the end-cap. Protolabs Network gave a total estimate of £2,536.18. Given the relatively low raw-material costs, significantly lower overall production costs may be achievable through manufacturing in-house.

Table 5.4: Manufacturing details

Component	**Quantity**	**Material**	**Manufacturing Methods**	**Xometry Quote / Protolabs Quote [£]**
Output shaft	2	Stainless Steel 316	CNC (turning or 5-axis), drilling	823.30 / 472.32
End-cap	2	Stainless Steel 316	CNC (turning or 5-axis), drilling, thread tapping	NA / 569.88
Rear housing	2	POM-C Acetal	CNC (turning or 5-axis), drilling	597.10 / 508.56
Rear connecting bracket	1	Stainless Steel 316	Laser cutting, thread tapping	142.72 / 241.40
Middle connecting bracket	2	Stainless Steel 316	Laser cutting	137.76 / 293.32

Chapter 6

Discussion

6.1 Site Flow Model

The derived analytical model provided a practical basis for defining inlet conditions and estimating actuator load within the project timescale. It captured the three main contributors to velocity, but remained a simplified representation of the site. Wave motion was represented as a single dominant Stokes second-order wave, whereas the real tidal flow is a superposition of waves with different amplitudes, periods, and directions, potentially causing freak waves. A single seabed roughness was applied, despite local bathymetry, potential wave refraction, and varying slope across the site.

The current velocities and wave velocities were scaled down to the near-bed height using the log-law. For a depth of 50 metres down to a height of 1-2 metres, there is a large scope of uncertainty here. It would be beneficial to design and deploy a small measuring device in the area where the ADCP will be deployed to improve confidence in both the analytical model and the CFD boundary conditions.

6.2 CFD Modelling

The CFD study produced a physically realistic flow field, reproducing accelerated flow over the frame, internal recirculation, and the expected bluff-body behaviour. The STAR-CCM+ model can therefore serve as a template for future studies, as it produced an accurate model that captures the complex flow details. An alternative to CFD modelling would be an experimental set-up within a frame using load cells to measure forcing values.

An important result was that actuator load was not proportional to the current velocity. In the sensitivity study, the largest outer-axis moment occurred under the long-term mean flow, which had a higher turbulence intensity because of its lower velocity. This indicates that internal mixing and vortex interaction within the frame were more important than current speed alone, and that domain size materially influenced the result. Given the recirculation velocities observed, biofouling is unlikely to be problematic.

Global verification was achieved, with an order of convergence of 2.85 and a finest-grid GCI of 0.08%. However, this does not guarantee local accuracy at the payload and gimbal rings. Validation against ADCP data was not possible without large time input, and because wave motion was defined only at the inlet, oscillatory behaviour decayed downstream of the frame (Figure 4.11).

Further work should prioritise reverse flow and tilted-frame or gimbal ring cases, particularly because the model showed a high-velocity stream above the frame at about 30° when assuming a flat seabed. Re-simulation with the final housing and updated gimbal geometry is also required. The reverse flow case remains the most important unresolved simulation, as higher velocities were observed on the side opposite the payload (Figure 4.14). However, the selected RH-17 actuator still provides a brake-holding safety factor of approximately 42.

6.3 Housing Design Process

The outcome of the housing design is a structurally verified, manufacturable and low-cost design ready for prototype manufacture and testing. Material selection was based on achieving the required function without overspending, with stainless steel 316 for the tolerance-critical shaft and end-cap, and POM-C acetal for the rear housing, where lower cost and simpler manufacture were advantageous. Before manufacturing, an actuator should be purchased for hands-on exploration to ensure its functionality, as understood in this project, is correct.

All components to be manufactured were designed conservatively, assuming that all forces throughout the assembly are applied to each component, with a safety factor of 2. This results from the limitations of SOLIDWORKS' in-built FEA, which is less accurate than dedicated FEA software such as ABAQUS, which can be used to perform full assembly analysis, including gimbal rings, dynamic analysis of sudden actuator activation, and cyclic loading [76].

A total cost estimate of £3,341.74 was produced for a set of two actuators, with the actuators accounting for 70% of the cost. Raw material totalled £534.03, 16% of the total. While cost was considered throughout the design, the stainless steel end-cap is the most expensive component at £340, due to the large diameter starting piece. The cost of raw materials excludes labour and manufacturing costs, which are hard to quantify without a manufacturer reviewing component drawings and tolerance specifications. The full system cost awaits the gimbal design, but the design presented provides a basis for manufacture. Further research into the financial viability of lip seals should be conducted, as they offer a performance advantage over O-rings.

Chapter 7

Conclusion and Further Work

7.1 Conclusion

This project aimed to develop a low-cost actuator and housing assembly for subsea alignment of ADCP sensors in high-energy coastal waters. A theoretical design supported by site characterisation, CFD, actuator selection, and component-level structural and manufacturability analysis has been presented.

Throughout the project, the following was developed:

- A simplified analytical flow model for the Fall of Warness.
- A grid-independent CFD study of flow around the frame and payload, which may be utilised for future design iterations and alternative flow conditions.
- A suitable actuator selected based on loading conditions.
- A detailed housing concept that is cost-effective, manufacturable and robust.
- A detailed bill of materials with costs, excluding labour costs.

A simplified flow model for the Fall of Warness was developed to describe the combined effects of current, waves, and turbulence. This provided a practical basis for defining CFD inlet conditions and estimating the loads acting on the payload and gimbal system.

The CFD study then characterised the flow around the frame and payload. The model reproduced the expected bluff-body behaviour, including stagnation ahead of the frame, separation, wake formation, and internal recirculation. A critical result was that the largest actuator load occurred under long-term mean-flow conditions rather than extreme conditions. The final model predicted a maximum moment of 1.1851 Nm about the outer gimbal axis, which was used as the actuator design load. Verification showed grid independence, with a finest-grid GCI of 0.08%.

A review of commercial subsea actuators showed existing products were generally unsuitable for this application because they were either back-drivable or overspecified for deep-water oil and gas service. The selected actuator was the MyActuator RH-17, which offered the best balance of size, cost, and holding performance. An effective brake holding torque of 50 Nm at the output shaft provides a safety factor of approximately 42 against the adopted design load, meeting the requirement that no power is required to hold position.

A detailed housing concept was then developed for an air-filled actuator rated to 100 m depth. The final material selection was stainless steel 316 for the output shaft and end-cap, and POM-C acetal for the rear housing. FEA gave safety factors of 2.63 for the output shaft, 5.9 for the end-cap, and 2.6 for the rear housing, with small displacements in all cases. Sealing arrangements, tolerances, fasteners, and mounting concepts were also defined and summarised in the bill of materials. The cost for a pair of actuator assemblies was £3,341.74.

The success of the project can be evaluated by comparison to the objectives outlined in Section 1.2. The objectives were almost fully satisfied, although the design could be further improved through initial manufacturing and testing to inform refinement.

7.2 Next Steps

It was decided that the original manufacturing and testing objectives would be sidelined, with focus on the theoretical design prioritised. These objectives are presented in Appendix E and should serve as a basis for future work.

The next stage should focus on reducing the remaining uncertainty before manufacture. The highest CFD priority is to complete the reverse-flow case, as higher velocities were observed on the side opposite the payload. Further simulations could include uneven or inclined seabeds or gimbal orientations, and should be repeated using the final housing geometry and the updated gimbal design. Future projects may include redesigning the frame to reduce recirculation within, and the gimbal rings to reduce the forcing experienced, both of which may use the CFD simulation used in this project.

Before manufacture, the complete actuator and gimbal assembly should be analysed using dedicated FEA software to assess full-load transfer, transient actuation, and cyclic loading. Further research into the financial and operational viability should be conducted. Then a prototype should be manufactured and tested to verify sealing, structural strength, and operational performance in representative subsea conditions.

Bibliography

[1] A. Hall, *The Challenges Of Renewable Energy*, en-GB, Jul. 2022. Accessed: 17th Mar. 2026. [Online]. Available: https://www.engineeringpowersolutions.co.uk/the-challenges-of-renewable-energy/.

[2] *Wave & Tide – Orkney Renewable Energy Forum (OREF)*, en-GB. Accessed: 17th Mar. 2026. [Online]. Available: https://www.oref.co.uk/orkneys-energy/wave-tide/.

[3] *Physics-Informed Estimation of Tidal and Subtidal Flow Fields From ADCP Repeat Transect Data - Jongbloed - 2025 - Water Resources Research - Wiley Online Library*. Accessed: 17th Mar. 2026. [Online]. Available: https://agupubs.onlinelibrary.wiley.com/doi/10.1029/2023WR036038.

[4] M. Wilson, 'Design, Analysis, and Comparison of Subsea Instrument Azimuth Rotation,' The University of Edinburgh, MEng Thesis, 2026.

[5] B. Sellar, Interview conducted via Microsoft Teams, 14 Oct. 2025.

[6] *Personal data processed by students | Data Protection*, en, Nov. 2023. Accessed: 17th Mar. 2026. [Online]. Available: https://data-protection.ed.ac.uk/guidance/personal-data-processed-students.

[7] *Origin 600 ADCP - Sonardyne*. Accessed: 17th Mar. 2026. [Online]. Available: https://www.sonardyne.com/product/origin-600-adcp/.

[8] *Nortek | Signature 500 | Current profiler*. Accessed: 17th Mar. 2026. [Online]. Available: https://www.nortekgroup.com/products/signature-500.

[9] *Workhorse II Sentinel ADCP*. Accessed: 17th Mar. 2026. [Online]. Available: https://www.teledynemarine.com/brands/rdi/workhorse-sentinel-adcp.

[10] *EMEC - The European Marine Energy Centre*, en-gb. Accessed: 17th Mar. 2026. [Online]. Available: https://www.orkney.com/life/energy/emec.

[11] *EMEC - Fall of Warness Wildlife Observation Programme | marine.gov.scot*, 2015. Accessed: 17th Mar. 2026. [Online]. Available: https://marine.gov.scot/?q=information/emec-fall-warness-wildlife-observation-programme.

[12] A. Naberezhnykh, D. Ingram and I. Ashton, 'Wavelet applications for turbulence characterisation of real tidal flows measured with an ADCP,' *Ocean Engineering*, vol. 270, p. 113 616, Feb. 2023, ISSN: 0029-8018. DOI: 10.1016/j.oceaneng.2022.113616. Accessed: 17th Mar. 2026. [Online]. Available: https://www.sciencedirect.com/science/article/pii/S0029801822028992.

[13] 'Environmental Description for the EMEC Tidal Test Site Fall of Warness, Orkney,' EMEC, Online, Tech. Rep., 2009. [Online]. Available: https://www.emec.org.uk/?wpfb_dl=140.

[14] *Open Data for Tidal Energy*. Accessed: 1st Apr. 2026. [Online]. Available: https://tidalenergydata.org/projects.

[15] B. Sellar, C. Old, P. Mccallum, N. Zigrat, M. Jordain De Thieulloy and M. Dorward, 'D2.2 - Next Generation Flow Measurements and Flow Classification,' Tech. Rep., 2021. Accessed: 2nd Nov. 2025. [Online]. Available: https://tidalenergydata.org/media/documents/RLT-WP2-2-PDL-000-04.pdf.

[16] *Arctic Rays*, 2024. Accessed: 30th Oct. 2025. [Online]. Available: https://arcticrays.com/.

[17] *SS109HT High Performance Pan & Tilt Device*, en. Accessed: 17th Mar. 2026. [Online]. Available: https://www.sidus-solutions.com/product/ss109ht-high-performance-pan-tilt-device/.

[18] J. Fairman, *Fluid Pressure and Depth*, 1996. Accessed: 17th Mar. 2026. [Online]. Available: https://www.grc.nasa.gov/www/k-12/WindTunnel/Activities/fluid_pressure.html.

[19] *5 Marine Energy Resources*, en. Accessed: 17th Mar. 2026. [Online]. Available: https://www.gov.scot/publications/scottish-shelf-model-part-2-pentland-firth-orkney-waters-sub/pages/8/.

[20] *SS350 Heavy Duty Subsea Rotator | Sidus Solutions*. Accessed: 17th Mar. 2026. [Online]. Available: https://www.sidus-solutions.com/product/ss350-heavy-duty-rotator/.

[21] *What is biofouling and how can we stop it?* en. Accessed: 17th Mar. 2026. [Online]. Available: https://www.sofarocean.com/posts/what-is-biofouling-and-how-can-we-stop-it.

[22] J. Harrison, 'ReDAPT MC7.3 Public Domain Report: Final,' en, Tech. Rep., Dec. 2015. [Online]. Available: https://tidalenergydata.org/media/documents/MC7.3_Operations_Final_Report.pdf.

[23] J. Lewis, 'Marine biofouling and its prevention on underwater surfaces,' *Materials Forum*, vol. 22, pp. 41–61, Jan. 1998.

[24] H. Rosenberg, 'Titanium in the marine environment,' in *OCEANS 82*, Sep. 1982, pp. 519–523. DOI: 10.1109/OCEANS.1982.1151780. Accessed: 2nd Apr. 2026. [Online]. Available: https://ieeexplore.ieee.org/document/1151780/.

[25] W. Wong, *What Are the Benefits and Uses of Titanium in Marine Environments?* en-US, Oct. 2024. Accessed: 2nd Apr. 2026. [Online]. Available: https://triplycircletitanium.com/what-are-the-benefits-and-uses-of-titanium-in-marine-environments/.

[26] P. Dhaiveegan, N. Elangovan, T. Nishimura and N. Rajendran, 'Corrosion behavior of 316L and 304 stainless steels exposed to industrial-marine-urban environment: Field study,' en, *RSC Advances*, vol. 6, no. 53, pp. 47 314–47 324, 2016. DOI: 10.1039/C6RA04015B. Accessed: 2nd Apr. 2026. [Online]. Available: https://pubs.rsc.org/en/content/articlelanding/2016/ra/c6ra04015b.

[27] M. Mihaljevic, *Atlas Steels Technical Handbook of Stainless Steels*, en, 2021. [Online]. Available: https://atlassteels.com.au/wp-content/uploads/2021/08/Atlas-Steels-Technical-Handbook-of-Stainless-Steels-12-08-21.pdf.

[28] *PEEK Polymer: Properties, Processing and Applications | 2026 Guide*, en. Accessed: 2nd Apr. 2026. [Online]. Available: https://www.weerg.com/guides/peek-3d-printing.

[29] *Applications for PEEK in Oil & Gas*, Advanced EMC Technologies, May 2018. Accessed: 2nd Apr. 2026. [Online]. Available: https://advanced-emc.com/applications-for-peek-in-oil-gas/.

[30] *Acetal*, en-US. Accessed: 2nd Apr. 2026. [Online]. Available: https://www.curbellplastics.com/materials/plastics/acetal/.

[31] *316 marine grade stainless steel and black acetal plastic subsea ROV sampling clamps – Safire Associates*, en-GB. Accessed: 2nd Apr. 2026. [Online]. Available: https://safire.uk.com/waterjet-cuting/316-marine-grade-stainless-steel-and-black-acetal-plastic-subsea-rov-sampling-clamps.

[32] *Guide to oil seals for your application*, en. Accessed: 2nd Apr. 2026. [Online]. Available: https://eriks.com/en/know-how-hub/blogs/oil-seal-selection-guide.html.

[33] *Bearing Isolators: An expert guide | aesseal.com*, en. Accessed: 2nd Apr. 2026. [Online]. Available: https://www.aesseal.com/en/resources/academy/bearing-isolators/.

[34] *Fundamentals of Mechanical Seals | Seal FAQs*, en-US. Accessed: 2nd Apr. 2026. [Online]. Available: https://www.sealfaqs.com/?page_id=940.

[35] U. B. Mehta and Z. Lavan, 'Flow in a Two-Dimensional Channel With a Rectangular Cavity,' en, *Journal of Applied Mechanics*, vol. 36, no. 4, pp. 897–901, Dec. 1969, ISSN: 0021-8936, 1528-9036. DOI: 10.1115/1.3564799. Accessed: 17th Mar. 2026. [Online]. Available: https://asmedigitalcollection.asme.org/appliedmechanics/article/36/4/897/425326/Flow-in-a-TwoDimensional-Channel-With-a.

[36] B. Sellar and D. Sutherland, 'Technical Report on Tidal Sire Characterisation During the ReDapt Project,' Tech. Rep., 2015. Accessed: 29th Oct. 2025. [Online]. Available: https://tidalenergydata.org/media/documents/Technical_Report_on_Tidal_Site_Characterisation_During_the_ReDAPT_Project_v4.0.pdf.

[37] U.-J. Lee, D.-H. Ko and J.-S. Park, 'Characteristic Analysis of Vertical Tidal Profile Parameters at Tidal Current Energy Site,' *Journal of Marine Science and Engineering*, vol. 12, no. 11, p. 1998, Nov. 2024. DOI: https://doi.org/10.3390/jmse12111998.

[38] N. Bergeron and A. Abrahams, 'Estimating shear velocity and roughness length from velocity profiles,' *Water Resources Research*, vol. 28, no. 8, pp. 2155–2158, Aug. 1992. [Online]. Available: https://doi.org/10.1029/92wr00897.

[39] R. J. S. Whitehouse and T. J. Chesher, 'Seabed Roughness in Tidal Flows A Review of Existing Measurements,' en, 1994. Accessed: 23rd Nov. 2025. [Online]. Available: https://eprints.hrwallingford.com/348/1/SR360.pdf?.

[40] M. Benitz, '6. Non-linear Water Waves,' en, Book Title: Ocean Hydrodynamics for Engineers. Accessed: 17th Mar. 2026. [Online]. Available: https://rwu.pressbooks.pub/oceanhydro/chapter/non-linear-water-waves/.

[41] V. Venugopal, *Wave Generation and Wave Theories*, Lecture Notes, Marine Energy 5 (MECE11009) Lecture 1-2, University of Edinburgh, 2026.

[42] *5.4.1: Wave orbital velocities*, en, Oct. 2021. Accessed: 18th Mar. 2026. [Online]. Available: https://geo.libretexts.org/Bookshelves/Oceanography/Coastal_Dynamics_(Bosboom_and_Stive)/05%3A_Coastal_hydrodynamics/5.04%3A_Wave_orbital_velocity_pressure_and_bed_shear_stress/5.4.01%3A_Wave_orbital_velocities.

[43] *Simcenter STAR-CCM+ CFD software*, en. Accessed: 17th Mar. 2026. [Online]. Available: https://www.siemens.com/en-us/products/simcenter/fluids-thermal-simulation/star-ccm/.

[44] *[CFD] Inflation Layers / Prism Layers in CFD*, Jun. 2021. Accessed: 17th Mar. 2026. [Online]. Available: https://www.youtube.com/watch?v=1gSHN99I7L4.

[45] D. Ingram, *Refinement_analysis.py*, CC-BY License, School of Engineering, The University of Edinburgh, Edinburgh, UK, 2021.

[46] J. G. Leishman, 'Bluff Body Flows,' en, Jan. 2023, Book Title: Introduction to Aerospace Flight Vehicles. DOI: 10.15394/eaglepub.2022.1066.n25. Accessed: 2nd Apr. 2026. [Online]. Available: https://eaglepubs.erau.edu/introductiontoaerospaceflightvehicles/chapter/bluff-body-flows/.

[47] *MyActuator*, en. Accessed: 20th Mar. 2026. [Online]. Available: http://uk.robotshop.com/search?q=myactuator.

[48] *User Manual for RH Series Products V1.4*, Jan. 2025. Accessed: 20th Mar. 2026. [Online]. Available: https://cdn.robotshop.com/rbm/acdeb3e1-04dc-4138-8b99-88509ddc4e94/9/93065726-15f2-4f69-9f8d-74782ec9de7a/032cbddd_user-manual-for-rh-series-products-v1.4.pdf?_gl=1*118xdex*_gcl_au*NzgxNDI4MTA5LjE3NzM3NjI3MTM.*_ga*MjEzNzMwMTEzMy4xNzczNzYyNzEz*_ga_FXHVC4EYRV*czE3NzM3NjI3MTIkbzEkZzEkdDE3NzM3NjI3NTIkajIwJGwwJGgw.

[49] *RH Series Harmonic Actuator*. [Online]. Available: https://cdn.robotshop.com/rbm/acdeb3e1-04dc-4138-8b99-88509ddc4e94/9/93065726-15f2-4f69-9f8d-74782ec9de7a/8dc47646_rh-series-dual-encoder-250212.pdf?_gl=1*ygxvd2*_gcl_au*NzgxNDI4MTA5LjE3NzM3NjI3MTM.*_ga*MjEzNzMwMTEzMy4xNzczNzYyNzEz*_ga_FXHVC4EYRV*czE3NzM3NjI3MTIkbzEkZzAkdDE3NzM3NjI3MTIkajYwJGwwJGgw.

[50] *RH-17-D Details*, en. Accessed: 23rd Mar. 2026. [Online]. Available: https://www.myactuator.com/rh-17details.

[51] *MCBH6M Subconn connector*, en. Accessed: 23rd Mar. 2026. [Online]. Available: https://surveyspares.com/products/mcbh6m-subconn-connector-1.

[52] *SOLIDWORKS for Students: 3D CAD Software for Education | SOLIDWORKS*, en, Oct. 2019. Accessed: 24th Mar. 2026. [Online]. Available: https://www.solidworks.com/product/students.

[53] *Clearance Hole Size for Bolts and Screws (Metric)*, en-GB, Aug. 2020. Accessed: 24th Mar. 2026. [Online]. Available: https://engineersbible.com/clearance-hole-metric/.

[54] *ISO 724 - Metric Threads*. Accessed: 27th Mar. 2026. [Online]. Available: https://www.engineeringtoolbox.com/metric-threads-d_777.html.

[55] *Rotary Seals*. [Online]. Available: https://www.trelleborg.com/-/media/tss-media-repository/tss_website/pdf-and-other-literature/catalogs/rotary_gb_en.pdf?rev=dea9fee9291342659839a425c17b7a30&openpdf=1.

[56] *CR Seals Handbook*, Nov. 2024. [Online]. Available: https://cdn.skfmediahub.skf.com/api/public/0901d196807662c1/pdf_preview_medium/0901d196807662c1_pdf_preview_medium.pdf.

[57] *Rotary Seal Design Guide*, en, 2018. [Online]. Available: https://www.parker.com/content/dam/Parker-com/Literature/Engineered-Polymer-Systems/5350.pdf.

[58] *Parker O-Ring Handbook*. Accessed: 25th Mar. 2026. [Online]. Available: https://www.parker.com/content/dam/Parker-com/Literature/Praedifa/Catalogs/Catalog_O-Ring-Handbook_PTD5705-EN.pdf.

[59] C. Powell and P. Webster, 'Copper Alloys for Marine Environments,' en, Copper Development Association, Tech. Rep., Dec. 2012. [Online]. Available: https://live.copper.org/applications/marine/cuni/alloys/pub-206-copper-alloys-for-marine-environments.pdf.

[60] *15th Report on Carcinogens*, en. Accessed: 29th Mar. 2026. [Online]. Available: https://ntp.niehs.nih.gov/research/assessments/cancer/roc.

[61] *McMaster-Carr*, en. Accessed: 27th Mar. 2026. [Online]. Available: https://www.mcmaster.com/.

[62] *Stainless Steel Bars, Stainless Steel Rods & Round Bars | metals4U*, en. Accessed: 4th Apr. 2026. [Online]. Available: https://www.metals4u.co.uk/materials/stainless-steel/stainless-steel-round?grade=70916&product_list_limit=96.

[63] *Titanium round Bar - TA6V grade (grade 5) - Diameter 60 mm*, en. Accessed: 27th Mar. 2026. [Online]. Available: https://www.titane-services.eu/Titanium-round-Bar-TA6V-grade-grade-5-Diameter-60-mm.

[64] *Surface Roughness Explained | Ra Roughness Chart*, en. Accessed: 29th Mar. 2026. [Online]. Available: https://get-it-made.co.uk/resources/surface-roughness-explained.

[65] *EPDM O Rings: EPDM Rubber O Rings & Seals*, en. Accessed: 4th Apr. 2026. [Online]. Available: https://simplybearings.co.uk/shop/Seals-O-Ring-Seals-EPDM-O-Rings/c19_4501_4707/index.html?selection=EPDM+Rubber+O-Rings&page=1.

[66] *Buy M3 x 16mm Full Thread Socket Cap Head Screws (DIN 912) - Marine Stainless Steel (A4)*, en-GB. Accessed: 29th Mar. 2026. [Online]. Available: https://www.accu.co.uk/metric-cap-head-screws/3978-SSCF-M3-16-A4.

[67] *Buy M3 x 40mm Socket Cap Head Screws (DIN 912) - Marine Stainless Steel (A4)*, en-GB. Accessed: 29th Mar. 2026. [Online]. Available: https://www.accu.co.uk/metric-cap-head-screws/3073-SSC-M3-40-A4.

[68] *Buy M3 Hexagon Nylon Locking Nuts (DIN 985) - Marine Stainless Steel (A4)*, en-GB. Accessed: 29th Mar. 2026. [Online]. Available: https://www.accu.co.uk/hexagon-nylon-locking-nuts/7957-HNN-M3-A4.

[69] *Buy M16 Hexagon Nylon Locking Nuts (DIN 985) - Marine Stainless Steel (A4-80)*, en-GB. Accessed: 29th Mar. 2026. [Online]. Available: https://www.accu.co.uk/hexagon-nylon-locking-nuts/652942-HNN-M16-A4-80.

[70] *Stainless Steel Threaded Bar 316/316L*, en-US. Accessed: 29th Mar. 2026. [Online]. Available: https://www.metalsupermarkets.co.uk/product/stainless-steel-threaded-bar-316-316l/.

[71] *Acetal Rod | Direct Plastics Limited*. Accessed: 27th Mar. 2026. [Online]. Available: https://www.directplastics.co.uk/acetal-rod.

[72] *Stainless Steel Round Bar 316/316L*, en-US. Accessed: 27th Mar. 2026. [Online]. Available: https://www.metalsupermarkets.co.uk/product/stainless-steel-round-bar-316-316l/.

[73] *Stainless steel sheet 8mm 2B | metals4U*, en. Accessed: 4th Apr. 2026. [Online]. Available: https://www.metals4u.co.uk/materials/stainless-steel/stainless-steel-sheet-and-plate/100734-p.

[74] *Xometry UK*, en. Accessed: 29th Mar. 2026. [Online]. Available: https://get.xometry.uk/quotes/145170.

[75] *Hubs | On-demand Manufacturing: Quotes in Seconds, Parts in Days*, en-001. Accessed: 29th Mar. 2026. [Online]. Available: https://www.hubs.com/.

[76] *Abaqus*, en, Jul. 2023. Accessed: 4th Apr. 2026. [Online]. Available: https://www.3ds.com/products/simulia/abaqus.

Appendix A

Interview GDPR Documentation

The following documents are the following, as a result of collaboration with Michael Wilson to determine the operation requirements of both MEng projects:

- Participant Information Sheet (2 pages)
- Participant Consent Form, signed (2 pages)
- Student Research Data Protection Impact Assessment (7 pages)

PARTICIPANT INFORMATION SHEET

You are being invited to take part in research on subsea sensor alignment systems. Alistair Murison (s2214327) and Michael Wilson (s2090366) at the University of Edinburgh is leading this research. Before you decide to take part, it is important that you understand why the research is being conducted and what it will involve. Please take time to read the following information carefully.

WHAT IS THE PURPOSE OF THE STUDY?

The purpose of the study is to gain knowledge that will be included in the literature reviews that Alistair and Michael will submit to the School of Engineering as part of their Masters projects, and will influence design decisions taken during their individual projects.

WHY HAVE I BEEN INVITED TO TAKE PART?

You are invited to participate in this study because you are involved with the projects that Alistair and Michael are working on for their Masters Projects, and you will have knowledge that will be beneficial in the research stage of their projects.

DO I HAVE TO TAKE PART?

No – it is entirely up to you. If you do decide to take part, please keep this Information Sheet and complete the Informed Consent Form to show that you understand your rights in relation to the research, and that you are happy to participate. If you do decide to take part, you are still free to withdraw at any time and without giving a reason. Please note down your participant number (which is on the Consent Form) and provide this to the lead researcher if you seek to withdraw from the study at a later date.

WHAT WILL HAPPEN IF I DECIDE TO TAKE PART?

You will be asked a number of questions primarily to establish the requirements of their projects. The interview will take place in a safe environment at a time that is convenient to you. Ideally, we would like to audio record your responses (and will require your consent for this), so the location should be in a fairly quiet area. The questionnaire interview will take around an hour to complete.

WHAT ARE THE POSSIBLE BENEFITS OF TAKING PART?

By sharing your experiences with us, you will be helping Alistair Murison, Michael Wilson, and the University to better understand how to design and build subsea actuator alignment systems.

ARE THERE ANY RISKS ASSOCIATED WITH TAKING PART?

There are no significant risks associated with participation.

WHAT IF I WANT TO WITHDRAW FROM THE STUDY?)

Agreeing to participate in this project does not oblige you to remain in the study nor have any further obligation to this study. If, at any stage, you no longer want to be part of the study, please inform the project administrator, Dr Brian Sellar, Brian.Sellar@ed.ac.uk. You should note that your data may be used in the production of formal research outputs (e.g., journal articles, conference papers, theses, and reports) prior to your withdrawal and so you are advised to contact the research team at the earliest opportunity should you wish to withdraw from the study. On specific request, we will destroy all your identifiable answers, but we will need to use the data collected prior to your withdrawal, and to maintain our records of your consenting participation.

DATA PROTECTION AND CONFIDENTIALITY

Your data will be processed in accordance with Data Protection Law. All information collected about you will be kept strictly confidential. Unless they are anonymised in our records, your data will be referred to by name. If you consent to being audio recorded, all recordings will be destroyed once they have been transcribed. Your data will only be viewed by the researcher/research team. All electronic data will be stored on a password-protected computer file, and all paper records will be stored in a locked filing cabinet. Your consent information will be kept separately from your responses in order to minimise risk. All data and information collected will be stored indefinitely under the research exemption of intention for future use.

WHAT WILL HAPPEN WITH THE RESULTS OF THIS STUDY?

The results of this study may be summarised in published articles, reports and presentations. Quotes or key findings will always be made anonymous in any formal outputs unless we have your prior and explicit written permission to attribute them to you by name. Information may also be kept for future research.

WHO CAN I CONTACT?

If you have any further questions about the study, please contact the lead researchers, Alistair Murison (s2214327@ed.ac.uk) and Michael Wilson (s2090366@ed.ac.uk)

If you wish to make a complaint about the study, please contact:

Dr. Brian Sellar, Brian.Sellar@ed.ac.uk

In your communication, please provide the study title and detail the nature of your complaint.

You can get this document on tape, in Braille, large print and various computer formats if you ask us. Please contact us on s2214327@ed.ac.uk or s2090366@ed.ac.uk.

For general information about how we use your data, go to:

https://www.ed.ac.uk/records-management/privacy-notice-research

PARTICIPANT CONSENT FORM

Study Titles:

Alistair Murison – Engineering Design of Actuated Sensor Alignment Systems for Subsea Applications

Michael Wilson – Design, Analysis, and Comparison of Subsea Instrument Azimuth Rotation System, integrated into 2-axis gimbal

	Please initial box
1. I confirm that I have read and understood the Participant Information Sheet for the above study.	BGS
2.	
3. I have been given the opportunity to consider the information provided, ask questions and have had these questions answered to my satisfaction.	BGS
4. I understand that my participation is voluntary and that I can ask to withdraw at any time without giving a reason and without my medical care or legal rights being affected.	BGS
5. I understand that my anonymised data will be stored for a minimum of 5 years and may be used in future ethically approved research.	
6. I agree to take part in this study.	BGS

Name of person giving consent	Date	Signature
Brian G Sellar	14/10/2025	BGS

Names of persons taking consent	Date	Signature
Alistair Murison	10/10/2025	**Alistair I. Murison**
Michael Wilson	13/10/2025	

DATA PROTECTION IMPACT ASSESSMENT
Student Research

PROJECT NAME:	Engineering Design of Actuated Sensor Alignment Systems for Subsea Applications

OVERVIEW

1. Project outline – what and why

Explain broadly what the project aims to achieve and what type of processing it involves. You may find it helpful to refer or link to other documents, such as a project proposal.

For the motivation section of the Project Proposal form:

This project will focus on the further development of a gravity-moored sensor platform system, with the design of electro-mechanical actuators to actively align and correct the positioning of a sensor, which collects water velocity data. The existing system relies on a passive gimbal system, which can be disrupted by tidal forces, vibrations, and other interference, leading to misalignment and unusable data.

The aspiration is to design a low-cost, high-performance rotational actuator and housing that significantly improves data collection quality and reliability. This technology may have the potential for commercialisation in the offshore renewable energy (ORE) sector, as well as in climate change monitoring and coastal defense.

The proposed actuator setup would also be used to align the sensors to communicate with other sensors. The actuator design will contain a motor, which will be selected based on performance characteristics to be determined as part of the project, that is sealed from highly energetic coastal waters up to a depth of 100 metres. Although the project could work from the pre-existing gimbal set design, alternative methods of sensor alignment will also be explored. Current subsea actuators exist, but they are not suited to this application through their balance of quality and materials, and cost.

Two types of housing will be considered: for a large high-torque motor and one for a low-torque variant. If the project processes well, a prototype may be manufactured and tested if financial and time constraints allow. The engineering design of the actuator housing will address material selection, part specification, sealing strategies, and tolerancing to ensure long-term subsea performance.

2. Describe the information flow

You should describe the collection, use and deletion of personal data here and it may also be useful to refer to a flow diagram or another way of explaining data flows – where you are getting the data from, where it will be stored and where it could be transferred to. You should also say how many individuals are likely to be affected by the project.
e.g. Data will be collected from research participants via online forms

↓

Data will be stored encrypted on departmental drives

↓

The dataset will be provided to the School of Engineering as an appendix in the interim and final reports

There are likely to be 2-3 participants affected by the project.

Interview Data flow:

Information will be collected in recorded interviews with participants via with transcription of conversation taken. No voice recordings will be stored, they will be deleted after the transcript is complete.

↓

Typed notes and transcription will be stored on University of Edinburgh OneDrive

↓

Information will be used to inform design and research of project deliverables and may be included in final report and presentations. Opinions will be excluded from this output.

3. Privacy law compliance

Note: Data Protection legislation is relevant to any DPIA, and a DP compliance check should always be carried out. The Data Protection Officer will be able to advise you on the relevance of other privacy laws.

3.1 UK General Data Protection Regulation (UK GDPR) and Data Protection Act 2018 (DPA)

	Question	**Answer**
1.	What personal data is going to be processed? See here for definition	Personal data will be collected in the form of information and opinions provided during interviews and consultations with participants involved in the research project.
	Principle 1 – Fairness, Lawfulness, Transparency	
2.	Are you processing the personal data under Article 6 (1) (e) – task carried out in the public interest? If not, explain what other legal basis you rely on.	The processing of this personal data is to be carried out on the basis of legal consent.

3.	If special categories of personal data are going to be processed, are you (in addition to the Article 6(1) legal bases) relying on the legal basis in Article 9 (2)(j) – necessary for research in the public interest? Note – special categories of personal data are personal data consisting of information as to (a) the racial or ethnic origin of the data subject, (b) political opinions, (c) religious beliefs, (d) Trade Union membership, (e) physical or mental health, (f) sexual life, (g) genetic data and (h) biometric information.	N/A; special categories of personal data not collected
4.	How are individuals being made aware of how their personal data will be used? If you supply participants with a PIS, please attach the PIS.	PIS Attached
	Principle 2 – Purpose Limitation	
5.	Does the project involve the use of existing personal data for new purposes?	Yes
	Principle 3 – Adequacy, Relevance, Data Minimisation	
6.	What procedures will be in place for checking that the data collection procedures are adequate, relevant and not excessive in relation to the purpose for which the data will be processed?	The completed Data Protection Impact Assessment will risk assess and ratify necessity of procedures
	Principle 4 – Accuracy	
7.	How will the personal data be checked for accuracy?	It will be confirmed with the participants of the study.
	Principle 5 – Storage Limitation	
8.	Will there be set retention periods in place in relation to the storage of the personal data or are you applying the research exemption that the data are intended for future use? If so, is this included in your PIS?	Research purposes exemption; data intended for future use. This is highlighted in the PIS.
	Principle 6 – Security	
9.	What technical and organisational security measures will be in place to prevent any unauthorised or unlawful processing of the personal data?	Data and information will only be stored on University of Edinburgh online data storage services i.e. Teams, OneDrive. These services are protected by University of Edinburgh security measures.
10.	Has the personal data been evaluated to determine whether its processing	Yes

	could cause damage or distress to data subjects?	
11.	Will you be transferring personal data to a country outside of the European Economic Area? If so where, and what arrangements will be in place to ensure that there are adequate safeguards over the data? If you have answered 'yes' and provided an explanation of safeguards, a separate approval procedure is required involving the Head of School. Advise your supervisor to consult the Data Protection Officer for further guidance and to initiate the approval procedure.	No
12.	If the data will be anonymised, is it likely that a 'motivated intruder' will be interested in attempting re-identification by linking the data with other information available to them? Check the guidance for more information on the 'motivated intruder' test.	No
A Data Protection compliance check has been carried out as part of this DPIA, the details of which are below. From this we have concluded: the project is data protection compliant.		
3.4 Common Law duty of confidence		
Note: This only applies when you use, for example medical data or similar types of data that individuals would not expect to see disclosed. Describe how you have obtained consent.		
N/A		
3.3 Human Tissue Act and the Medicines for Human Use (Clinical Trials) Regulations (if relevant)		
Note: This only applies to medical research. Describe how you have obtained consent.		
N/A		

4. Screening questions
Explain what practical steps you will take to ensure that you identify and address privacy risks. Who should be consulted about potential risks (members of your research team, supervisor, research sponsor…)? Then list the risks identified under 5. **Answer the questions by ticking the box if 'yes'.**

Will the project involve the collection of new identifiable or potentially identifiable information about individuals?	☑
Will the project compel individuals to provide information about themselves, i.e. where they will have little awareness or choice?	☑
Will identifiable information about individuals be shared with other organisations or people who have not previously had routine access to the information?	☐
Are you using information about individuals for a purpose it is not currently used for r in a new way, i.e. using data collected to provide care for an evaluation of service development.	☐
Where information about individuals is being used, would this be likely to raise privacy concerns or expectations, i.e. will it include health records, criminal records or other information that people may consider to be sensitive and private and may cause them concern or distress?	☐
Will the project require you to contact individuals in ways which they may find intrusive, i.e. telephoning or emailing them without their prior consent?	☐
Will the project result in you making decisions in ways which can have a significant impact on individuals, i.e. will it affect the care a person receives?	☐
Does the project involve you using new technology which might be perceived as being privacy intrusive, i.e. using biometrics, facial recognition or automated decision making?	☐
Is a service being transferred to a new supplier (re-contracted) and the end of an existing contract?	☐
Is processing of identifiable/potentially identifiable data being moved to a new organisation (but with same staff and processes)	☐

4. identification of risks

Note: You should carry out the risk analysis using exactly the same methodology as you do for other project risks. Enter the key risks that have been identified, and the options for avoiding or mitigating those risks, into the table below. Below are some of the most common risks – choose from these and add any other risk that might be specific to your work. *

Risk description	*Options for avoiding or mitigating this risk	Residual Privacy Risk after implementation of mitigation		
		High	Medium	Low
Information stored indefinitely may be used for longer than necessary	The information being stored and used in this study are for research purposes related to the study only. Information will only be accessible by the researchers.			☑
Inadequate disclosure controls increase the likelihood of information being shared inappropriately.	The information being stored and used in this study are for research purposes related to the study only. Information will only be accessible by the researchers and will not be shared externally of the researchers. All data and information will only be stored on University data storage services such as Teams or OneDrive, protected by University information security protocols.			☑
Without proper security, the possibility of external unlawful access to the data such as hacking increases	The information and data used in this study is to be stored solely on Univerisity of Edinburgh provided data storage services i.e. Teams or OneDrive. These are protected by robust Microsoft and University of Edinburgh data security protocols. Information must not be stored externally of these services.			☑
Shared opinions that participants may find damaging if shared publicly.	Information that participants share will not be used in the publicly shared output works of this research study.			☑

* For each privacy risk, there could be a number of options for avoiding or mitigating that risk. You should list all the options then consider the residual risk for each one

5. Approval by academic supervisor (date and signature)
BRIAN G. SELLAR – 27th October 2025

Appendix B

CFD Simulation Files

B.1 STAR-CCM+ Simulation Files

The files used during the CFD section of the project are listed below, in order of their first use.

Table B.1: List of .sim files used in CFD simulations

File name (.sim)	Notes
Simulation Setup	Prior to running simulations. Outdated
Preliminary Simulations	
Initial Simulation V2	First refinement
Refined Simulation	Further refinement
Refined Simulation_Unsteady	First unsteady flow file
Half Model Simulation V1	Attempted half model. Unresolvable errors
Full Model Simulation V1	Half model updated to full model
Full Model Simulation V2.1	0.5 m base size. Used in grid convergence study
Full Model Simulation V2.1_0.25m base	For grid convergence study. Too fine - crashes on initiation
Full Model Simulation V2.1_2m base	For grid convergence study
Full Model Simulation V2.1_1m base	For grid convergence study
Full Model Simulation V2.1 Back Flow	
Full Model Simulation V2.2	Domain size increased
Full Model Simulation V3_1m base	Attempted simulation with gimbals upright - subtract feature errors
Full Model Simulation V3_1m base_Mean	Attempted simulation with gimbals upright - subtract feature errors
Full Model Simulation V4 1 Year	For sensitivity study on smaller domain, coarser 1 m base size. Small correction to overall equations from this point.

File name (.sim)	Notes
Full Model Simulation V4 50 Year	For sensitivity study on smaller domain, coarser 1 m base size
Full Model Simulation V4 Long Term Mean	For sensitivity study on smaller domain, coarser 1 m base size
Full Model Simulation V5 Long Term Mean	In-between iteration file
Full Model Simulation V5 Back Flow	In-between iteration file
Full Model Simulation V6 Long Term Mean	Final model with largest domain and finest grid
Full Model Simulation V6 Back Flow	Final model with reverse flow. Unresolvable instability.

B.2 Additional CFD Plots

As part of the collaboration with Michael Wilson for his MEng project, *Design, Analysis, and Comparison of Subsea Instrument Azimuth Rotation*, a number of plots from the final CFD simulation file were shared to inform his design decisions.

Figure B.1 shows the moment produced about the azimuth axis, showing a maximum value of 0.1049 Nm, but a minimum of 0.0992 Nm, suggesting asymmetry in the flow.

Figure B.2 shows the horizontal force acting on the ADCP payload. A maximum value of 4.7452 N in the direction of flow is low, and contrary to the flow movement seen in figures that demonstrate recirculation within the frame.

Figure B.3 shows the vertical force acting on the ADCP payload. Forces ranging from 2457.76 N to 2548.5 N in the upward direction suggest that flow is pushing the ADCP upward, and/or it is being pulled up by the high velocity stream above.

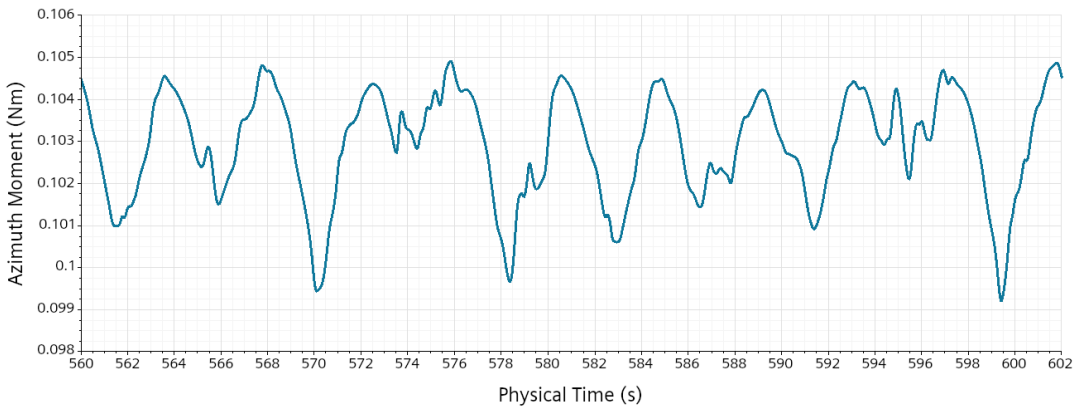


Figure B.1: Azimuth moment about gimbal vertical axis

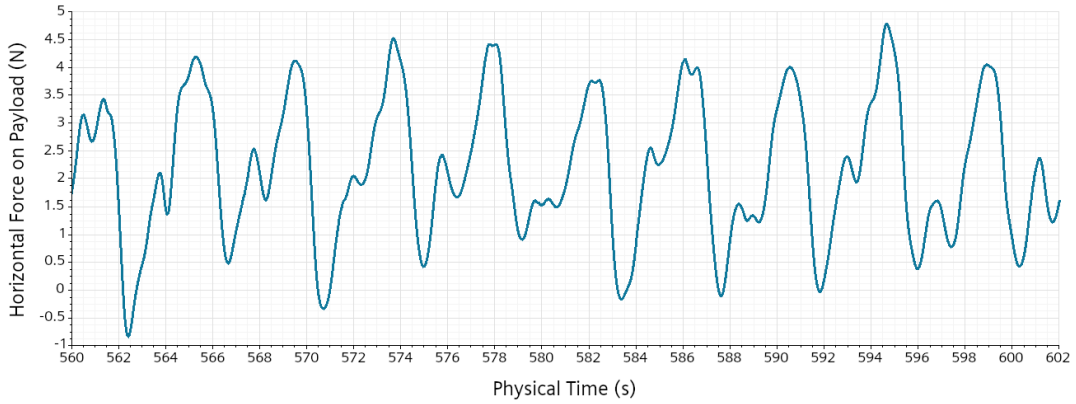


Figure B.2: Horizontal force on payload

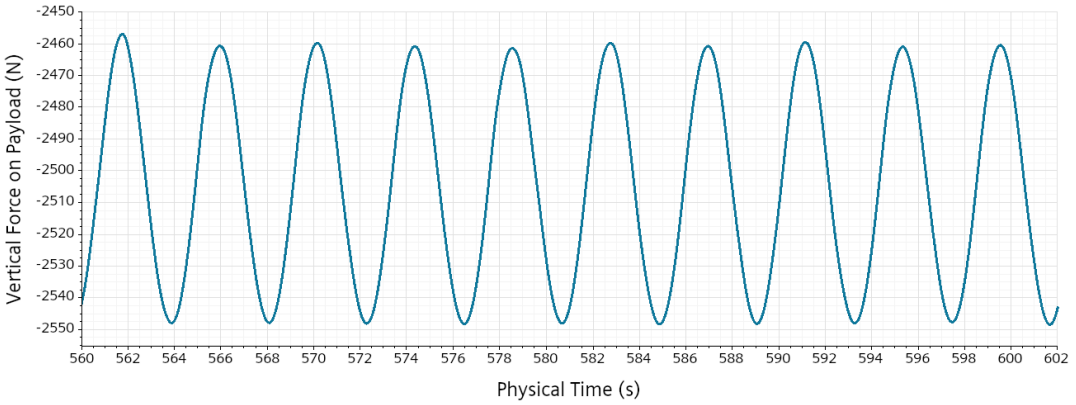


Figure B.3: Vertical force on payload

Appendix C

GCI Python Scripts

Two Python scripts used in Spyder 6 for the grid convergence study. grid_refinement.py remains modified, while values obtained from CFD simulations are input to GCI.py.

C.1 grid_refinement.py

```
import numpy as np
import matplotlib.pyplot as plt
from matplotlib.ticker import MultipleLocator

class Error(Exception):
    '''Class used to create errors'''
    pass

class gridsNotOrdered(Error):
    '''Raised when no the grids are not ordered with the finest grid first'''

class refinement_analysis:
    '''Grid refinement analysis tools

    A series of tools and a driver function for performing a grid refinement
    study using Python.  The tools are based on the RefinenementAnalysis.m
    Matlab programme written by D Ingram based on the NASA NPARC Fortran code
    published as part of the grid convergence assessment collaboration.

    The equations used are those given by Patric Roache in his 1998 book.

    David Ingram, School of Engingeering
    (c) 2021 The University of Edinburgh
    License: CC-BY, Creative Commons by Attribution
    '''

```

```
27      def __init__(self,x,f):
28          ''' Create a new instance of the refinement analysis using
29          data obtained from a mesh refinement study.  The two
30          parameters given are arrays of the same length containing the
31          grid spacing (x) and the function values (f) that have been
32          evaluated on each grid.
33          '''
34          N = len(x) # number of grids used in the study
35          # store the mesh spacing and the function values in the object
36          self.f = f
37          self.x = x
38
39          # check the grid spacings are in the correct order and if not
40          # throw an exception.
41          if all(x[i] < x[i+1] for i in range(N-1)) is False:
42              raise gridsNotOrdered
43
44          # now compute the mesh spacings
45          self.r = np.divide(x[1:],x[:-1])
46
47          # finally estimate the the order of convergence using the
48          # first three data pairs and assuming that the grid refinement
49          # ratio is constant, r(1) = r(2). This is done using
50          # Eqn. 5.10.6.1 of (Roache, 1998).  This needs three grids
51
52          try:
53              self.p = abs(np.log(abs(f[2]-f[1])/abs(f[1]-f[0]))/np.log(self.r[0]))
54          except:
55              print("Warning: Only 2 grids are provided, 2nd order is assumed")
56              self.p = 2.0
57
58      def richardson(self):
59          '''calculate the Richardson extrapolation Estimate of the
60          value of f on a mesh with delta_x = 0. '''
61
62          f_exact = self.f[0] + (self.f[0]-self.f[1]) / (
63              self.r[0]**self.p - 1.0)
64          return f_exact
65
66      def plot(self, Richardson = False, f_name = 'function'):
67          '''produce a plot of f against dx.  If Richardson is True then
68          the value of f with delta_x = 0 will be plotted.  f_name is
69          used to determine the name of the function value to be used on
70          the y-axis.'''
```

```
71
72          # create a plot in Matplotlib
73          fig, ax = plt.subplots(1)
74          ax.plot(self.x,self.f, color = 'blue', linestyle=':',
75              marker='o' )
76
77          # add axis titles
78          ax.set(xlabel = r'Grid Spacing $\Delta x$',
79              ylabel = f_name)
80
81          # If Richardson is True add a symbol marker for Delta_x = 0 on
82          # the y-axis
83          if Richardson is True:
84              ax.plot(0.0,self.richardson(),'rx')
85          else:
86              ax.set_xlim(left=0.0)
87
88          # We don't want a box round the plot and we want to ensure the
89          # x-axis sits exactly on x=0.0  The following commands turn
90          # off the top and right "spines" and enforce the left edge at
91          # x=0.0.
92          ax.spines['left'].set_position('zero')
93          ax.spines['right'].set_color('none')
94          ax.yaxis.tick_left()
95
96          ax.spines['top'].set_color('none')
97          ax.xaxis.tick_bottom()
98
99          # Display the plot.
100         plt.show()
101
102     def graph(self, Richardson = False, f_name = 'function', filename='refinement_analysis.pdf'):
103         '''output a plot of f against dx.  If Richardson is True then
104         the value of f with delta_x = 0 will be plotted.  f_name is
105         used to determine the name of the function value to be used on
106         the y-axis.'''
107
108         # create a plot in Matplotlib
109         fig, ax = plt.subplots(1)
110         ax.plot(self.x,self.f, color = 'blue', linestyle='--',
111             marker='o' )
112
113         # add axis titles
114         ax.set_xlabel(r'Grid Spacing, $\Delta x$', fontsize=12)
```

```
115         ax.set_ylabel(f_name, fontsize=12)
116 
117         ax.grid(True, linestyle='--', alpha=0.5)
118 
119         ax.xaxis.set_major_locator(MultipleLocator(0.02))
120         ax.yaxis.set_major_locator(MultipleLocator(0.002))
121 
122         # If Richardson is True add a symbol marker for Delta_x = 0 on
123         # the y-axis
124         if Richardson is True:
125             ax.plot(0.0,self.richardson(),'rx')
126         else:
127             ax.set_xlim(left=0.0)
128 
129         # We don't want a box round the plot and we want to ensure the
130         # x-axis sits exactly on x=0.0  The following commands turn
131         # off the top and right "spines" and enforce the left edge at
132         # x=0.0.
133         ax.spines['left'].set_position('zero')
134         ax.spines['right'].set_color('none')
135         ax.yaxis.tick_left()
136 
137         ax.spines['top'].set_color('none')
138         ax.xaxis.tick_bottom()
139 
140         # Display the plot.
141         plt.savefig(filename)
142 
143     def GCI(self,A,B):
144         ''' Compute Grid Convergence Index (GCI) between grids A and
145         B using Eqn. 5.6.1 from Roache's book. Using a factor of
146         safety as recommended on page 123. The parameters A and B
147         are grid numbers, so grid 1 is the finest grid and grid N is
148         the coarsest.'''
149 
150         # How many grids have been used
151         N = len(self.x)
152 
153         # Set the satfey factor, if there are more than 2 grids then
154         # this is 1.25, if there are only 2 grids then the saftey
155         # factor is 3.0
156         if (N>2):
157               f_safe = 1.25
158         else:
```

```
            f_safe = 3.0

        # Now compute the relative error in f between the grids
        epsilon = abs(self.f[B-1] - self.f[A-1]) / abs(self.f[A-1])

        # and return the GCI
        return f_safe * epsilon / (self.r[0]**self.p - 1.0)

    def GCI_all(self):
        ''' Compute the GCI on the sequence of all grid pairs'''

        # How many grids have been used
        N = len(self.x)

        # Loop over the grids calculating the GCI(A,B) with A going
        # from 1 to N-1 and B from 2 to N.
        gci = []
        for i in range(N-1):
            gci.append(self.GCI(i+1,i+2))

        return gci

    def GCI_ratio(self,tol=1.0e-2):
        '''Examine if asymptotic range has been achieved by examining
        ratio of Eqn. 5.10.5.2 of Roache's book is one.  tol is used
        as a tollerance with np.isclose(ratio,1.0,tol) to see if the
        computed ratio is close to 1.0'''

        # Calculate the GCI for all the grids
        gci = self.GCI_all()

        # find out how many GCI's we have calculated
        N = len(gci)

        if (N>2):
            # Loop over the grids calculating the ratios
            ratio = []
            for i in range(N-1):
                ratio.append(self.r[0]**self.p * gci[i]/gci[i+1])
        else:
            print("Warning: Only 2 grids used, ratios cannot be calculated.")
            ratio = [1000.0]

        return [ratio, np.isclose(ratio, 1.0, tol)]
```

```
203
204     def report(self,f_name = 'function', tol =1.0e-2):
205         ''' print a report on the grid convergence study. f_name is
206         the description of the function being measured on the grid and
207         tol is the tolerance used to see if the GCI ratio is close to
208         one. '''
209
210         # How many grids
211         N = len(self.x)
212         print(f"Refinement Analysis on {N} grids.\n")
213
214         # Tabulate the grids and the function values
215         heading = f"Grid Delta x ratio  {f_name}"
216         print(heading)
217         print("-"*len(heading))
218         for i in range(N-1):
219             print("{:4d} {:7.4g} {:5.2g} {:9.6g}"
220                       .format(i+1, self.x[i], self.r[i], self.f[i]))
221         print("{:4d} {:7.4g}   --- {:9.6g}"
222                   .format(N, self.x[-1], self.f[-1]))
223         print("-"*len(heading),"\n")
224
225         # report the order of accuracy
226         print("order of convergence, p = {:6.2f}".format(self.p))
227
228         # report the Grid Convergence Index
229         gci = self.GCI_all()
230         print("\nGrids       GCI\n---------------")
231         for i in range(len(gci)):
232             print("{:2d} {:2d} {:9.4g}".format(i+1,i+2, gci[i]))
233         print("---------------\n")
234
235         # report the GCI Ratios
236         if (len(gci)>2):
237             ratio, converged = self.GCI_ratio(tol)
238             print(" Grid Step  GCI Ratio Converged")
239             print("-------------------------------")
240             for i in range(len(ratio)):
241                 print("{:2d}{:2d} {:2d}{:2d}     {:7.4g} {}"
242                           .format(i+1,i+2,i+2,i+3,ratio[i],converged[i]))
243             print("-------------------------------\n")
244
245     # These last two functions enable python to describe the
246     # refinement analysis object (using repr) and to give a short
```

```
247     # human readable summary (using str).
248 
249     def __repr__(self):
250         ''' describe the object for the command line'''
251         return f'refinement analysis(x={self.x}, f={self.f})'
252 
253     def __str__(self):
254         ''' describe the object for a print command'''
255 
256         N = len(self.x)
257 
258         return f'''Refinement Analysis on {N} grids.
259 
260   dx = {self.x}
261   f  = {self.f}
262 
263   refinement ration, r = {self.r}
264   order of convergence, p = {self.p}
265 
266   Grid Convergence Indicies: {self.GCI_all()}
267 
268   GCI ratios : {self.GCI_ratio()}
269 '''
```

C.2 GCI.py

```
"""
Created on Wed Dec 17 15:32:04 2025

@author: Alistair Murison
"""

from refinement_analysis import refinement_analysis

# Grid spacing (metres, finest to coarsest)
x = [0.07440076758, 0.1461384848, 0.2214329664]

# Drag coefficient from STAR-CCM+
f = [0.6785775, 0.6760163333, 0.6584878333]

# Run analysis
analysis = refinement_analysis(x, f)
analysis.report("Drag Coefficient Grid Convergence")
analysis.graph(True, r"Drag Coefficient, $C_D$")
```

Appendix D

Component Technical Drawings

- Figure D.1: Output shaft technical drawing
- Figure D.2: End-cap technical drawing
- Figure D.3: Rear housing technical drawing
- Figure D.4: Rear connection plate drawing
- Figure D.5: Middle connection plate drawing

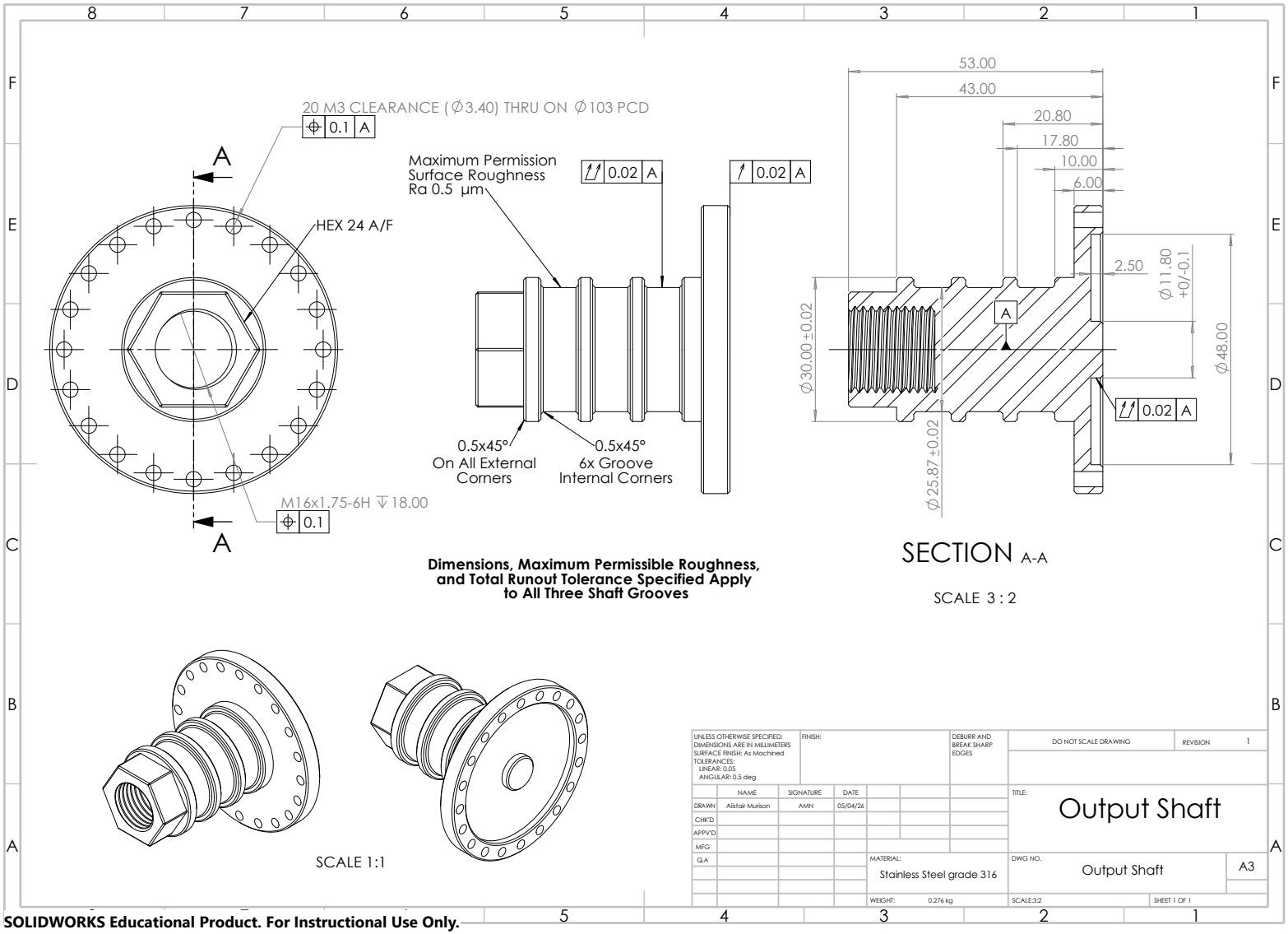


Figure D.1: Output shaft technical drawing

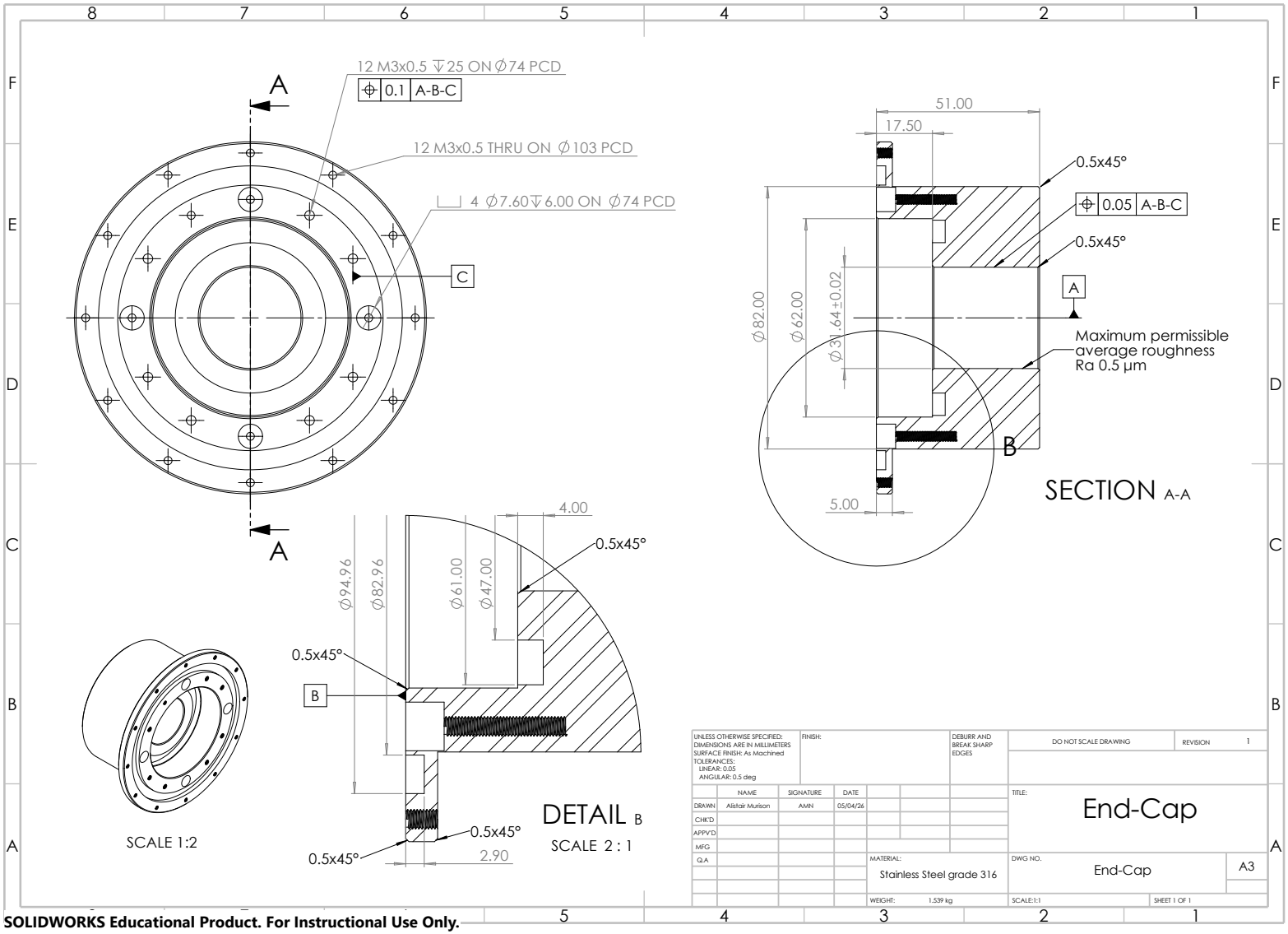


Figure D.2: End-cap technical drawing

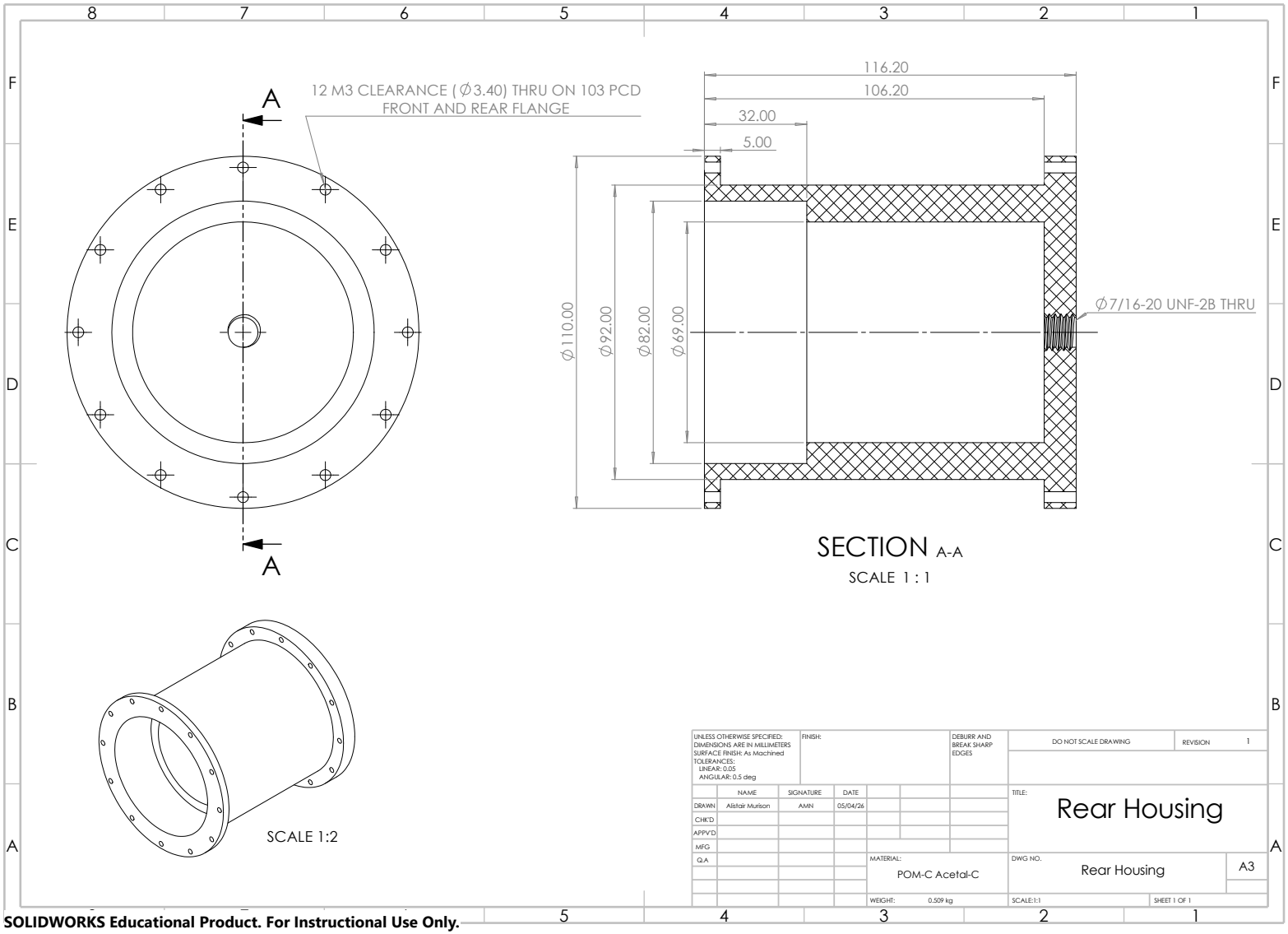


Figure D.3: Rear housing technical drawing

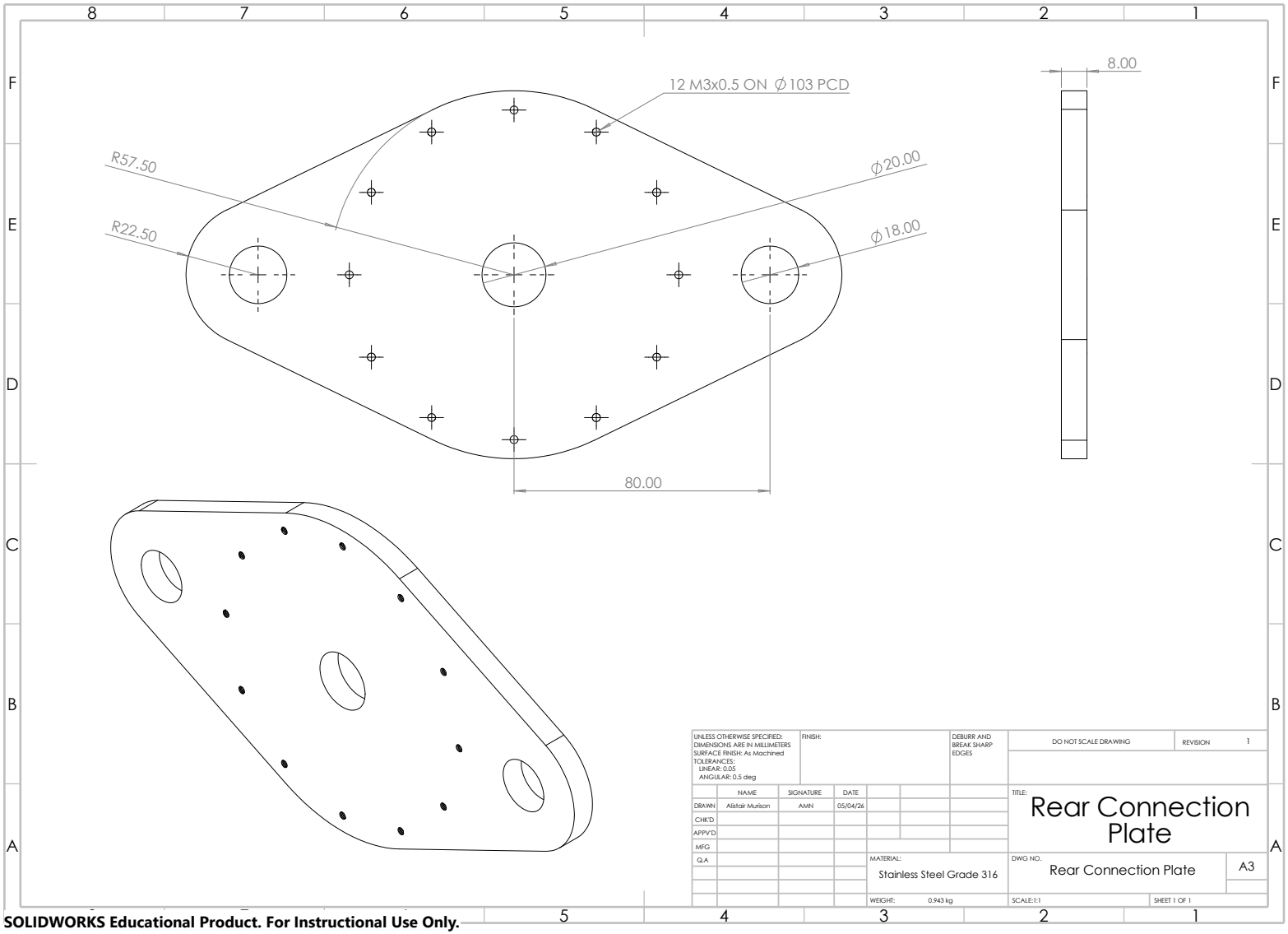


Figure D.4: Rear connection plate technical drawing

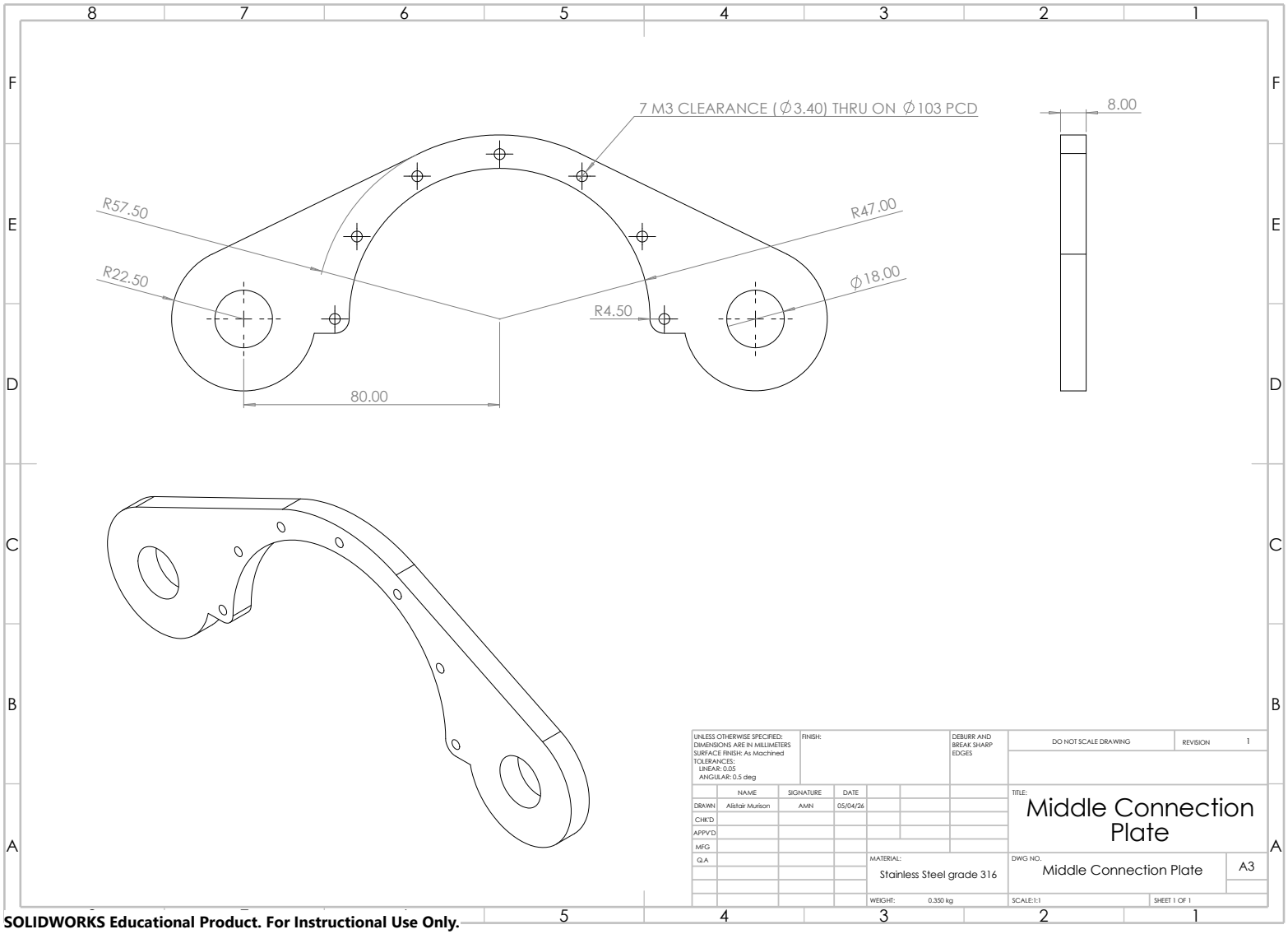


Figure D.5: Middle connection plate technical drawing

Appendix E

Manufacture and Testing Objectives

Manufacturing and testing objectives were included in the project proposal, subject to financial and time constraints. They were sidelined around the submission of the interim report to focus on the theoretical design.

These objectives were:

- Manufacture and assemble a prototype actuator housing assembly, complete with actuator, including a testing rig if required.
- Validate actuator performance under predicted subsea loading conditions, as determined by Objective 1.
- Validate the tolerances and sealing type required to prevent seawater ingress, as determined in Objective 2.
- Determine the relationship between sealing techniques and friction between the seals and actuator shafts.